SEARCH FOR THE RARE DECAY OF A B MESON TO A K MESON AND TWO NEUTRINOS

A Dissertation

Presented to the Faculty of the Graduate School

of Cornell University

in Partial Fulfillment of the Requirements for the Degree of

Doctor of Philosophy

by

John Gregg Thayer

May 2004

SEARCH FOR THE RARE DECAY OF A B MESON TO A K MESON AND TWO NEUTRINOS

John Gregg Thayer, Ph.D.

Cornell University 2004

We search for the exclusive decays $B \to (K^+, K_S, K^{*+}, K^{*0})\nu\bar{\nu}$ in a sample of 9.7 million charged and neutral B meson decays recorded by the CLEO detector at the $\Upsilon(4S)$resonance. The technique was one of full event reconstruction where after selecting a signal B candidate the remainder of the event is required to be consistent with a hadronic $B \to D^{(*)}(n\pi)$ decay. No signals were observed so 90% confidence level upper limits were set at: $\mathcal{B}(B^+ \to K^+\nu\bar{\nu}) < 6.1 \times 10^{-4}$, $\mathcal{B}(B^0 \to K_S\nu\bar{\nu}) < 2.3 \times 10^{-3}$, $\mathcal{B}(B^+ \to K^{*+}\nu\bar{\nu}) < 2.0 \times 10^{-3}$, and $\mathcal{B}(B^0 \to K^{*0}\nu\bar{\nu}) < 2.6 \times 10^{-3}$.

BIOGRAPHICAL SKETCH

Gregg Thayer was born in Chicago on Valentine's Day 1974, thereby initiating a lifelong association with irony. He spent his suburban childhood being obnoxious and taking things apart. He enjoyed reasonable success putting them back together and in keeping with the thrift of his parents, usually was able to save a few obviously superfluous parts.

At the suggestion of his Grandfather, the family attended an open house at Fermilab in nearby Batavia when he was about ten. The Fermilab outreach machine never let go. Later, they came to his Junior High School and showed him how to make a cloud chamber, which was pretty darn cool. While in High School, he participated in Fermilab's Saturday Morning Physics program.

Majoring in Physics when he attended the University of Illinois in Urbana, was practically a foregone conclusion. That he actually graduated with a degree in Physics is perhaps more surprising. While at Illinois, he attended the organizational meeting for Physics Van, part of the Physics Department's Outreach program. Not only did this lead to his participation in over 50 shows for elementary school children, but the faculty advisor, Mats Selen, hired him to help assemble a cosmic ray telescope. The rest of his undergraduate career consisted of playing with high voltage, liquid nitrogen, and having far more fun than is usually allowed in a physics lab. It was at Illinois that he met Jana, who he married on

August 7, 1999, a day that will live in infamy.

After graduating from Illinois in 1996, Gregg continued his education at Cornell University, where he worked for Chris Bebek on several electronics projects in support of the CLEO III detector upgrade. He had so much fun, that he didn't even start an analysis until his fourth year. But under the expert guidance of Jim Alexander, he has finally competed this dissertation.

To my parents, James and Marcia,

my sister Susan,

and my wife, Jana.

They have put up with a lot.

ACKNOWLEDGEMENTS

When you've been in graduate school as long as I have, you have a lot of people to thank. Unfortunately, being in graduate school as long as I have, I'm sure to forget many of the people who have helped see me through. I apologize ahead of time to anyone who I've left out.

There are three people from whom I have learned more than any others. Mats Selen gave me my first Physics job, saving me from another summer of construction work. Amid the cables, ancient computers, lead bricks, and roaches of Physics Lab One at the University of Illinois, he not only taught me about the different aspects of a particle physics experiment, but showed me exactly how much fun experimental physics could be. It was on his advice that I came to Cornell to work for Chris Bebek on the CLEO III upgrade.

The opportunity to learn from Chris was the most rewarding part of working on CLEO. Chris was responsible for guiding me through the projects I completed, teaching me about electronics and software along the way. The sheer volume of his knowledge made it impossible not to learn from him.

When it was finally time for me to start a physics analysis, my advisor Jim Alexander took the reins, and taught me much about how analysis is done. His style of advising allowed me the time I needed to see all sides of a problem, and when all was beyond hope, he could show me where I was wrong. He may disagree,

but I couldn't have asked for a better advisor.

Among those I had the pleasure of working with during the installation of CLEO III are Elliot Lipeles, Charlie Strohman, Andreas Wolf, Valera Frolov, Todd Pedlar, Karl Ecklund, Dan Peterson, and Tom Meyer. Tom and I spent much of our formative years cabling and re-cabling the CC, working in DAQ lab, and taking care of any loose ends that Chris Bebek could assign to us. We learned about the guts of CLEO together, and I've always wanted to comment my code as well as he does.

No one who has ever shared an office with Véronique Boisvert can say that it wasn't a very interesting place to be. Though I never had the pleasure of being the recipient of one of her to-do lists, our discussions were probably responsible for delaying both of our graduations by several months. The rest of my fellow graduate students and their significant others have also been a great source of support and merriment through the years. Most recently Chris Stepaniak, Pete Zweber and Adie Gloor, Lauren Hsu, Alan Magerkurth, Mike and Tammie, have helped keep me sane. Thanks to anyone who has ever participated in the CLEO graduate student poker night.

My Cornell classmates and their families proved to be great fun and were a big part of my first few years at Cornell. Becky B., Jenny H., Aash C., Tom G., Nick B., Cayce B., Steve and Katie K., Merlin M-M., Anatoli O., Stanimir B., Craig and Tauni C., and, of course, the irrepressible Janis Chang.

Anyone who has met my family knows they are the reason that I am who I am. (The good and the bad.) Their support has been unwavering over the twenty-

some years that I've been in school, and I couldn't have done it without them. This dissertation is for them, and I hope they never have to read it.

I suppose I have the rest of my life to acknowledge the contributions that Jana has made to my life, so I'll keep it short here. Those who know her, know exactly how lucky I am to have her as a wife and colleague. (Really lucky.)

TABLE OF CONTENTS

LIST OF TABLES

LIST OF FIGURES

CHAPTER 1

INTRODUCTION

The subject of elementary particle physics can appear esoteric and removed from common experience. It may well be. After all, its currency is counted in any number of unseeable (if not undetectable) particles whose relevance to the macroscopic world is described either by clumsy analogy or complicated mathematics. However, current theories (collectively known as the Standard Model) have been extremely successful at predicting the outcome of experiments.

The emergence of particle physics at the forefront of our understanding of the universe is the product of more than 300 years of interplay between theory and experiment. In some cases, a theory may be developed to explain one set of experimental data only to predict some other result. In other cases, unexpected experimental results have demanded new ideas, *new physics*, to explain them. The subject of this dissertation is a search for such an anomaly, a decay predicted by present theories to be too rare to be seen in the current data. A more subtle example of this counterpoise between theory and experiment is provided by those theorists who help experimentalists interpret their data and suggest new experiments, or those experimentalists who make precision measurements to guide the development of theory.

The following introduction is not meant to be an exhaustive history of modern physics (it isn't). Rather, in order to give context to this dissertation, and the goals of elementary particle physics, it will briefly describe examples of how physics has attempted to explain diverse phenomena by common laws. It is through this process that we have developed our current understanding of the fundamental nature of our universe.

1.1 Classical Physics

Physics didn't start with Isaac Newton, but his contributions represent one of the best examples of the unifying power of physics. In addition to inventing the framework of classical mechanics, his law of universal gravitation united celestial mechanics and terrestrial mechanics. According to Newton, the force responsible for objects falling near the Earth's surface was the same force which held the planets in orbit around the sun. With his laws of motion he was able to derive the orbital mechanics of Johannes Kepler as well as the motion of projectiles [1].

In the nineteenth century, electricity and magnetism were the subject of much study. In 1820 Hans Christian Oersted performed experiments which showed there was a relationship between electric currents and magnetic fields. Namely, current in a wire would deflect the needle of a compass. Only a week later, André-Marie Ampère had a mathematical description of it [2]. A decade later, Michael Faraday observed the complimentary phenomena, that a changing magnetic field will create an electric current. But, a complete description of this unified electromag-

netism had to wait for James Clerk Maxwell to show that the various electrical and magnetic phenomena under study at the time could be described by a set of four relatively simple inter-related equations. (Actually we have Heinrich Hertz to thank for the compact notation of the "Maxwell Equations" [1].)

The development of atomic theory was also taking place in the nineteenth century, accompanying this was the combination of mechanics and thermodynamics in the kinetic theory of gasses. James Prescott Joule measured the relationship between mechanical energy and temperature by recording the amount of mechanical work needed to raise the temperature of water by a given amount. The idea that temperature and motion were related was a relatively radical idea, especially considering there was no hard evidence for the existence of atoms. (Though there were other reasons to suspect their existence.) John Dalton inferred the existence atoms by noting that the proportions of elements participating in chemical reactions were fixed. By studying many chemical reactions, chemists were able to infer the relative weights of many elements. In fact, by the 1860's there were over 60 elements defined this way, but this menagerie lacked order [3]. (Something very much like this happened in the early days of particle physics.) By ordering the elements by atomic weight and grouping them by their chemical properties, Dmitri Mendeleev succeeded in extracting order from the chaos in the form of his Periodic Table of elements. He was even able to predict the existence of new elements which were missing in his table, but the underlying reasons for this order had to wait for the advent of Quantum Mechanics in the twentieth century.

1.2 Modern Physics

A common place to mark the birth of modern particle physics is the discovery of the electron by J.J. Thompson in 1897. This negatively charged particle was correctly surmised to be a component of the atom. At the time, it was known that atoms were themselves neutral, so for the negatively charged electron to be a part of the atom there needed to be a source of positive charge to balance it. But, the atomic structure eluded physicists until Ernest Rutherford's scattering experiment [4] showed that the positive charge was localized at the center of the atom, dubbed the nucleus.

Studying the atomic weights in the periodic table, it was clear the view of the atom as a simple positively charged nucleus surrounded by electrons was incorrect. For example, Hydrogen, with atomic weight 1 had a nucleus with charge +1. Helium, whose nucleus had a charge of +2 weighed 4 times the weight of Hydrogen. Chadwick's 1932 discovery of a neutral particle with the mass of the proton, the neutron, resolved this. Now the Helium nucleus could contain 2 protons and 2 neutrons and have the correct weight and charge.

Over the course of the next forty years, more particles were discovered. Physicists were forced to categorize them by their properties, but without the satisfaction of knowing the source of the patterns that were seen. In 1961 Murray Gell-Mann and Yuval Ne'eman independently arranged the observed particles based on their charge and a property then known as strangeness. Much like the Periodic Table of Mendeleev, there were gaps in the pattern, which were filled by particles

whose properties had been predicted [4]. Then in 1964 Gell-Mann and Zweig independently proposed that the structure could be explained if the particles were not fundamental, but instead composed of other particles called quarks. Particles which contained quarks are known as hadrons, and are subdivided into two categories: baryons and mesons. In the quark model, baryons consist of three quarks, while mesons consist of a quark-antiquark pair.

Another process that under scrutiny at the beginning of the twentieth century was nuclear beta decay, where the nucleus of a radioactive atom would change to a lighter nucleus and emit an electron. When the energy spectrum to the electron was measured, it was not mono-energetic as would be expected in a two body decay. This led Wolfgang Pauli to postulate the existence of another particle which could carry away the momentum. The following year, Enrico Fermi devised a theory that included a small neutral particle which he dubbed the neutrino. There was a restriction on the mass of this particle. It needed to have extremely small or even zero mass since the electron spectrum endpoint extended to the kinematic limit.

By the end of the 1970s, our current understanding of particle physics had pretty much been assembled. The resulting framework is known as the Standard Model (SM). In the SM, there are three basic types of particles, quarks, leptons, and vector bosons. All matter is made of quarks and leptons, and the fundamental forces are mediated by the vector bosons. The quarks and leptons are grouped into three generations as here:

$$\begin{pmatrix} u \\ d \end{pmatrix} \begin{pmatrix} c \\ s \end{pmatrix} \begin{pmatrix} t \\ b \end{pmatrix} \tag{1.1}$$

$$\begin{pmatrix} \nu_e \\ e \end{pmatrix} \begin{pmatrix} \nu_\mu \\ \mu \end{pmatrix} \begin{pmatrix} \nu_\tau \\ \tau \end{pmatrix} \tag{1.2}$$

The upper row quarks all have charge $+\frac{2}{3}$ and are named up, charm, and top. The lower row have charge $-\frac{1}{3}$ and are named down, strange, and bottom. In the lepton family, the upper row contains the zero charged neutrinos. The bottom row contains the leptons of charge -1, the electron, muon, and tau.

The three forces in the SM are the electromagnetic force, the strong nuclear force, and the weak nuclear force. Gravity is not included in the SM, but is weak enough to be ignored. The electromagnetic force is mediated by the massless, chargeless photon (γ). The weak nuclear force is mediated by the $\pm W$ and Z^0 bosons. These bosons are massive, which limits the range of the weak interaction. The weak interaction is of particular interest to this analysis, and is described in more detail in Chapter 2. The strong nuclear force is mediated by massless gluons. Though electrically neutral, gluons do carry strong charge, called color. This is responsible for the peculiar fact that the strong force between two quarks actually increases as the distance between the quarks increases.

This has been an intentionally brief overview of particle physics. Chapter 2 deals with the the aspects of the SM which are particularly relevant to this analysis, Chapter 3 is a description of the apparatus used to collect the data used in this analysis, and Chapters 4 and 5 detail the analysis technique itself.

In 1944 Erwin Schrödinger wrote (as quoted in Reference [2]):

> We feel clearly that we are only now beginning to acquire reliable material for welding together the sum total of all that is known into a

> whole; but, on the other hand, it has become next to impossible for a single mind fully to command more than a small specialized portion of it. I can see no other escape from this dilemma (lest our true aim be lost forever) than that some of us should venture to embark on a synthesis of facts and theories, albeit with second-hand and incomplete knowledge of some of them–and at the risk of making fools of ourselves.

Though he wasn't referring specifically to dissertation writing, he could have been. (He also could have used more than two sentences.)

CHAPTER 2

THE PHYSICS OF $B \to K\nu\bar{\nu}$

2.1 The Standard Model

Here we describe the aspects of the Standard Model relevant to this analysis. As outlined in Chapter 1, the Standard Model describes matter as being made of quarks and leptons. To describe the electroweak interactions of these particles they are grouped into the $SU(2)_L$ doublets:

$$\begin{pmatrix} u \\ d' \end{pmatrix}_L \quad \begin{pmatrix} c \\ s' \end{pmatrix}_L \quad \begin{pmatrix} t \\ b' \end{pmatrix}_L \tag{2.1}$$

$$\begin{pmatrix} \nu_e \\ e^- \end{pmatrix}_L \quad \begin{pmatrix} \nu_\mu \\ \mu^- \end{pmatrix}_L \quad \begin{pmatrix} \nu_\tau \\ \tau^- \end{pmatrix}_L \tag{2.2}$$

The significance of the primes in Equation 2.1 is that the weak eigenstates of the quarks are not the same as the mass eigenstates, which are the quarks which we normally consider. If Equation 2.1 is a complete basis, there is a matrix which describes the rotation from the electroweak basis to the mass basis. This matrix is known as the Cabibbo-Kobayashi-Maskawa (CKM) matrix [5, 6] and is shown

in Equation 2.3.

$$\begin{pmatrix} d' \\ s' \\ b' \end{pmatrix} = \begin{pmatrix} V_{ud} & V_{us} & V_{ub} \\ V_{cd} & V_{cs} & V_{cb} \\ V_{td} & V_{ts} & V_{tb} \end{pmatrix} \begin{pmatrix} d \\ s \\ b \end{pmatrix} \tag{2.3}$$

So, for example, what we would normally consider a b quark is, in fact, a mixture of electroweak eigenstates b', s', and d' with relative contributions given by the appropriate CKM matrix elements. Likewise, a b' state is a mixture of b, s, and d. This allows weak decays to traverse the generations of quarks. One important aspect of the CKM matrix is that, in the Standard Model, it is unitary. This fact prohibits so called flavor changing neutral currents at the tree level. This is accomplished through the GIM mechanism [7]. In which for each diagram of a flavor changing neutral current there is a corresponding one to cancel it. Perfect unitarity causes this to hold for all orders. These CKM matrix elements are nine of the parameters of the Standard Model which must be measured experimentally. The decays $B \rightarrow K\nu\bar{\nu}$ involve the matrix element V_{ts} as will be described in Section 2.2.

There is a feature of strong interactions that merits a quick note. At short distance scales, strong effects can be calculated using perturbative expansions, but over long distances, this is not the case. To actually calculate useful quantities, a technique known as the Operator Product Expansion (OPE) [8] is used. OPE allows us to express the effective weak Hamiltonian as:

$$\mathcal{H}_{eff} = \frac{G_F}{\sqrt{2}} \sum_i V^i_{CKM} C_i(\mu) Q_i \tag{2.4}$$

where Q_i are operators which describe the decays, and $C_i(\mu)$ are the Wilson coef-

ficients which can be calculated pertubatively for appropriately small scales. The amplitude for a given decay of a meson M into a final state F is then given by:

$$A(M \to F) = \langle F \left| \mathcal{H}_{eff} \right| M \rangle = \frac{G_F}{\sqrt{2}} \sum_i V^i_{CKM} C_i(\mu) \langle F \left| Q_i(\mu) \right| M \rangle \tag{2.5}$$

Where $\langle F \left| Q_i(\mu) \right| M \rangle$ are the matrix elements of Q_i between M and F at scale μ. In the case of $B \to K\nu\bar{\nu}$, this is the the simple $V - A$ current. This sum has the advantage that the short distance calculation of the coefficients can be calculated pertubatively, while the long distance contribution is contained in the matrix elements are calculated non-perturbatively. In the case of box and penguin diagrams, the Wilson coefficients contain the contributions of the heavy particles in the loop (t quarks, W and Z bosons, in the case of $B \to K\nu\bar{\nu}$) and depend on the masses of those particles. If an extension to the SM contains other heavy particles, their contributions are also included in $C_i(\mu)$.

2.2 $B \to K\nu\bar{\nu}$

The decay $B \to K\nu\bar{\nu}$ is among the theoretically cleanest of rare B decays. It proceeds via the box and Z-penguin diagrams shown in Figure 2.1. The effective Hamiltonian for this process is

$$\mathcal{H}_{eff} = \frac{G_F}{\sqrt{2}} \frac{\alpha}{2\pi \sin^2(\theta_W)} V_{ts} V^*_{tb} X(x_t) \bar{b} \gamma^\mu (1 - \gamma_5) s \bar{\nu} \gamma_\mu (1 - \gamma_5) \nu \equiv c_L^{SM} \mathcal{O}_L \tag{2.6}$$

where $X(x_t)$ accounts for the contribution of two-loop diagrams[9]. To illustrate an attractive feature of studying this decay, we compare it to arguably the next simplest rare B decay, $B \to K\ell^+\ell^-$. The decay proceeds by the same diagrams as

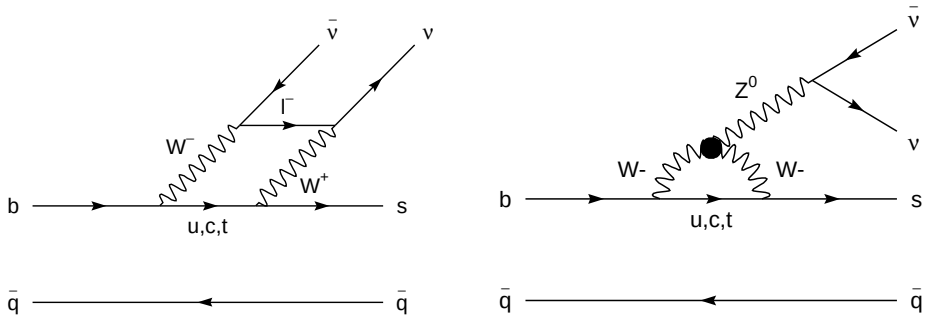

Figure 2.1: The dominant diagrams which contribute to $B \to K\nu\bar{\nu}$.

$B \to K\nu\bar{\nu}$, with the neutrinos replaced with charged leptons. However whereas $B \to K\nu\bar{\nu}$ relies on a single Wilson coefficient, $B \to K\ell^+\ell^-$ depends on several [10]. So called long distance interactions arise due to the charges of the leptons and resonant effects of the charmonium resonances which decay to two leptons. $B \to K\nu\bar{\nu}$ does not suffer from this complication [10].

There are two goals for any measurement of the branching fractions $B \to K\nu\bar{\nu}$: to measure the parameters of the standard model, and to set limits on contributions of New Physics. There are many techniques for quantifying the effects of New Physics [11, 12, 13, 14, 11, 15], but any effect must manifest itself by either modifying the Standard Model coefficient c_L^{SM} in Equation 2.6 or by introducing a new, right-handed operator resulting in an effective Hamiltonian:

$$\mathcal{H}_{eff} = c_L\mathcal{O}_L + c_R\mathcal{O}_R \tag{2.7}$$

The effect of this modification could be an enhancement of the branching fraction

or an alteration of the expected kinematics of the decay.

Equation 2.6 shows that the decay $B \to K\nu\bar{\nu}$ depends on the value of the CKM element V_{ts}. By combining a measurement of $\mathcal{B}(B \to K^*\nu\bar{\nu})$ and $\mathcal{B}(B \to \rho\ell\nu)$ one can extract a value for $|V_{ts}|/|V_{ub}|$ with small theoretical uncertainties [16, 14]. Similarly, from the ratio of branching fractions $\mathcal{B}(B \to X_s\nu\bar{\nu})$ and $\mathcal{B}(B \to X_c\ell\nu)$ one can extract the ratio $|V_{ts}|/|V_{cb}|$ [8].

The standard model predictions of the branching fractions of $B \to K\nu\bar{\nu}$ are[9]:

$$\mathcal{B}(B^- \to K^- \sum_i \nu_i\bar{\nu}_i) = (2.6 \pm 0.6)\left(\frac{|V_{ts}|}{0.04}\right)^2 \times 10^{-6} \tag{2.8}$$

$$\mathcal{B}(B^- \to K^{*-} \sum_i \nu_i\bar{\nu}_i) = (5.1 \pm 0.8)\left(\frac{|V_{ts}|}{0.04}\right)^2 \times 10^{-6} \tag{2.9}$$

2.3 Signal Monte Carlo

This analysis is a search for the exclusive decays $B \to K^{(*)}\nu\bar{\nu}$ not the inclusive $B \to X_s\nu\bar{\nu}$, so a word on the matrix elements of the effective Hamiltonian 2.6 is in order. In what follows, we parameterize the matrix elements following the convention in Reference [17]. For the scalar kaons, this is:

$$\langle K(p')|\bar{s}\gamma_\mu b|B(p)\rangle = (p+p')_\mu F_1(q^2) + \frac{M_B^2 - M_K^2}{q^2} q_\mu \left[F_0(q^2) - F_1(q^2)\right] \tag{2.10}$$

where $q = p - p'$ and $F_1(0) = F_0(0)$. In the signal Monte Carlo simulations generated for this analysis we followed [9] and used

$$F_1(q^2) = \frac{F_1(0)}{1 - q^2/M_P^2} \tag{2.11}$$

with $F_1(0) = 0.25 \pm 0.03$ and $M_P = 5$ GeV.

The vector kaons, with their polarization (ϵ), present a more complicated face. The matrix elements are parameterized in the following way:

$$\begin{aligned}\langle K^*(p',\epsilon)\,|\bar{s}\gamma_\mu(1-\gamma_5)\,b|\,B(p)\rangle &= \epsilon_{\mu\nu\alpha\beta}\epsilon^{*\nu}p^\alpha p'^\beta\frac{2V(q^2)}{M_B+M_{K^*}}\\ &-i\Bigg[\epsilon^*_\mu(M_B+M_{K^*})\,A_1\left(q^2\right)-(\epsilon^*\cdot q)\,(p+p')_\mu\frac{A_2(q^2)}{(M_B+M_{K^*})}\\ &-(\epsilon^*\cdot q)\frac{2M_{K^*}}{q^2}\left(A_3\left(q^2\right)-A_0\left(q^2\right)\right)q_\mu\Bigg]\end{aligned} \tag{2.12}$$

where $A_0(0)=A_3(0)$ and

$$A_3\left(q^2\right)=\frac{1}{2M_{K^*}}\left[(M_B+M_{K^*})\,A_1\left(q^2\right)+(M_{K^*}-M_B)\,A_2\left(q^2\right)\right]. \tag{2.13}$$

Again, following Reference [9] we use:

$$V\left(q^2\right)=\frac{V(0)}{1-q^2/M_p^2}, \tag{2.14}$$

with $V(0)=0.47\pm0.03$ and $M_p^2=5$ GeV, and

$$A_i\left(q^2\right)=A_i(0)\left(1+\beta_i q^2\right), \tag{2.15}$$

with $A_1(0)=0.37\pm0.03$, $\beta_1=-0.023$ GeV^{-2}, $A_2(0)=0.40\pm0.03$, and $\beta_1=0.034$ GeV^{-2}. The kaon momentum and missing energy distributions for the Monte Carlo samples generated using these matrix elements are shown in Figure 2.2.

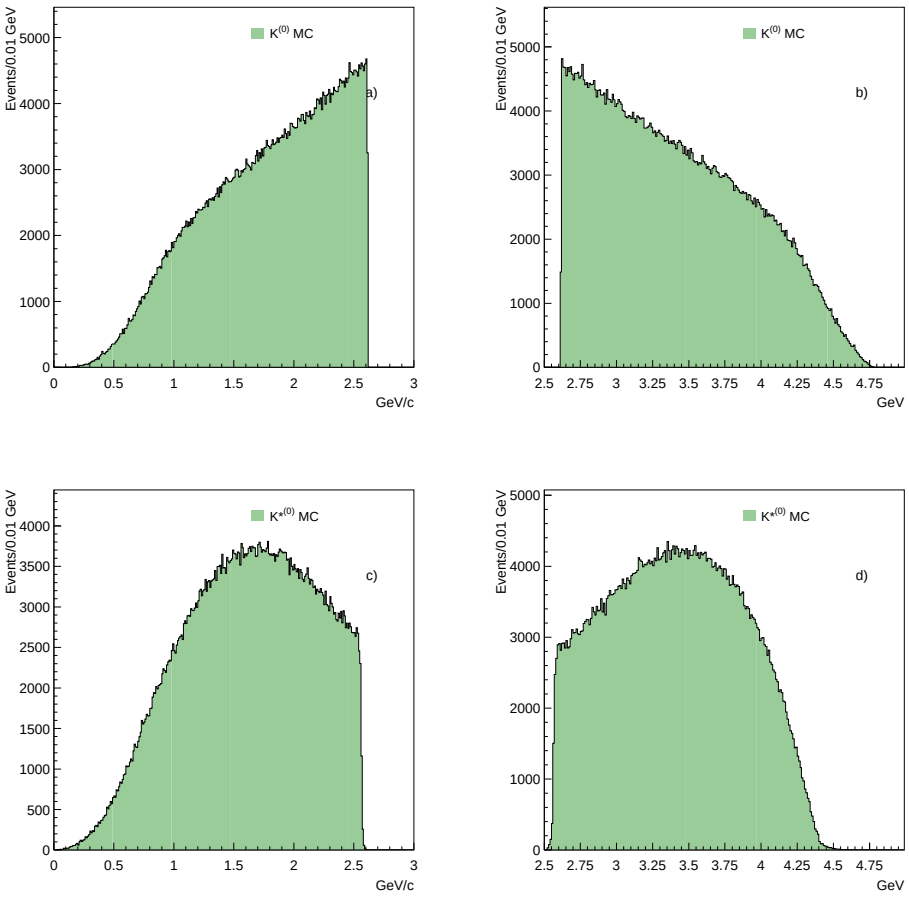

Figure 2.2: Signal Kinematics: p_K and E_{miss}.

Signal Monte Carlo generated kaon momentum for a) scalar kaons and b) vector kaons. Signal Monte Carlo generated missing energy spectrum for c) scalar kaons and d) vector kaons.

CHAPTER 3

THE EXPERIMENTAL APPARATUS

Twelve meters below the athletic fields at Cornell University sits the last of the university-based high energy particle physics accelerators. The Wilson Synchrotron Laboratory is home to the Laboratory for Elementary-Particle Physics, nèe Laboratory of Nuclear Studies. Here, beneath the fickle Ithaca sky there is the perennial sunshine of electron-positron annihilation. In the Accelerator Complex, beams are created by the Injection System, stored in the storage ring, CESR, and smashed together. The detritus of these collisions are recorded in the CLEO detector for analysis. This chapter is a brisk digest of the parts of the Lab that provided the data analyzed for this dissertation.

3.1 The Accelerator Complex

The Wilson Lab Accelerator Complex is shown in Figure 3.1. It is the luxury of the particle physicist to believe that the physics of particle accelerators is the physics of freshman E&M. Meanwhile, the accelerator physicist struggles with the immense complexity of getting bunches of electrons and positrons to smash into each other thousands of times a second at nearly the speed of light. Nevertheless,

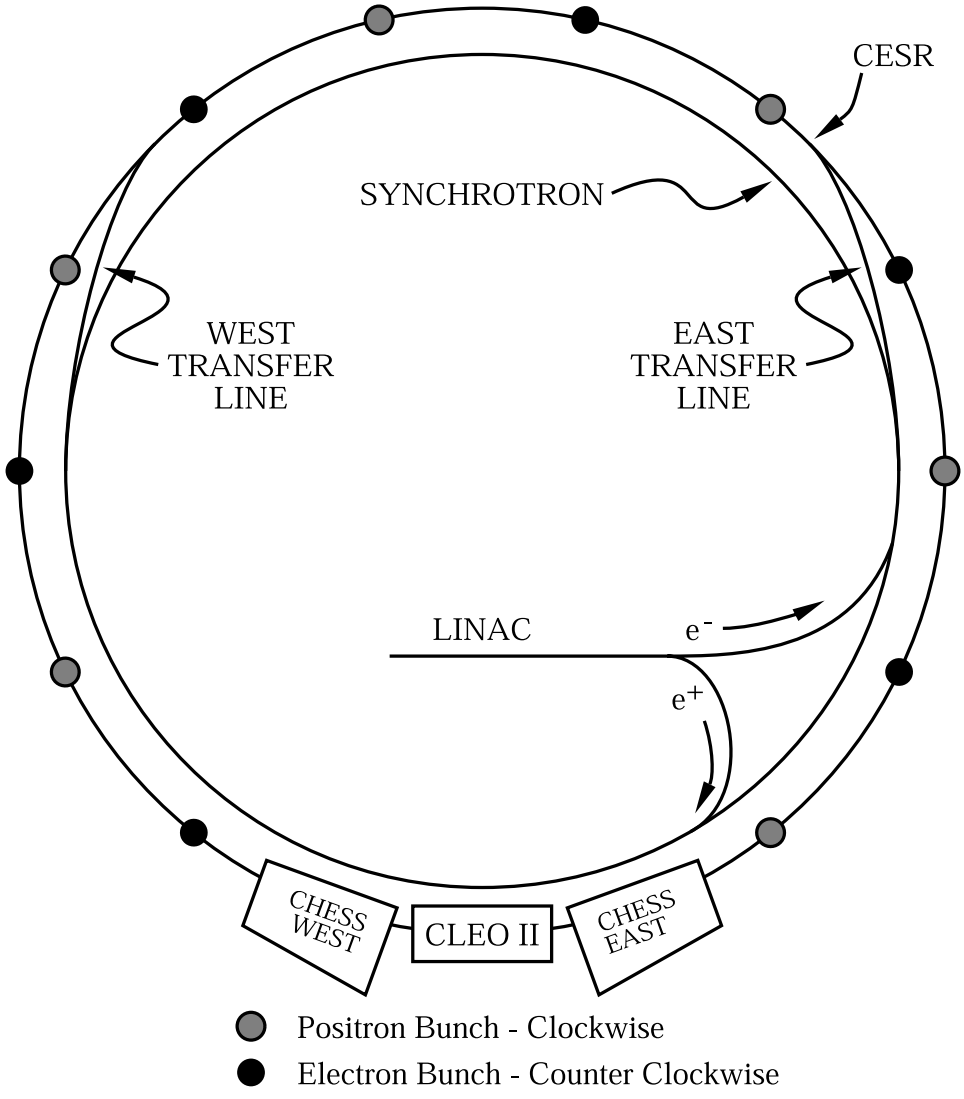

Figure 3.1: The Wilson Lab Accelerator Complex.

we will approach the physics of accelerators simply, and leave it to our colleagues to approach the topic in all its glory.

3.1.1 The Physics of Accelerators

There are three basic equations that govern the motion of the particles in particle accelerators. Taken directly from a freshman physics text, they define the force $\vec{F}$ on a charge q exerted by another charge q_2, an electric field $\vec{E}$, and a magnetic field $\vec{B}$:

$$\vec{F} \propto \frac{qq_2}{r_2^2}\hat{r}_2 \tag{3.1}$$

$$\vec{F} \propto q\vec{E} \tag{3.2}$$

$$\vec{F} \propto q(\vec{v}_q \times \vec{B}) \tag{3.3}$$

Each of these forces finds a role to play in the Accelerator Complex. Electric fields are used to accelerate the electrons and positrons while magnetic fields steer and focus them. There are forces between the particles in each bunch that endeavor to blow the bunch apart while forces between oppositely charged bunches passing through each other result in complicated couplings among all of the bunches in the ring. From these equations, we see that a magnetic field will cause charged particles to move in a circle. This is what gives CESR its ring[1]. The radius of this circle is set by the particles momentum p and the strength of the magnetic field as given by

$$R = \frac{p}{qB}. \tag{3.4}$$

[1]To quote Foghorn Leghorn, "That's a joke, son."

Armed with this sketch of the important physics, we will take a walk along the path we ask our electrons and positrons to tread.

3.1.2 Injection System

Before there was a storage ring, what has become the CESR injection system was the source of high energy electron beams for fixed target experiments. Now, electrons and positrons are produced, accelerated and injected into CESR by the components described in this section.

The electron gun produces electrons by placing a voltage on a cathode grid high enough to drive electrons out of the material. The electron gun in use at CESR [18] is capable of generating peak currents of 19 A! These electrons are then "prebunched" by magnets in preparation for being accelerated by the linear accelerator or linac.

Once in the linac, the electron bunches are accelerated by the electric fields in a series of radio-frequency (RF) cavities. These cavities are driven by klystrons which generate electromagnetic waves. These waves oscillate in the cavities and the electron bunches are timed to pass through the cavities so that they are accelerated. By the end of the 30 m linac, the electrons have achieved an energy of 350 MeV[19].

Positrons are created by electrons striking a 1/4 inch tungsten plate placed about half way down the linac. Upon striking the converter, a spray of particles, including positrons, is ejected. The positrons are selected and bunched by a series of magnets and then accelerated down the remaining sections of the linac. By the end, they have reached an energy of 220 MeV.

After passing through the linac, the synchrotron accelerates the particles up to their final energy. The beams are bent into a circle by dipole magnets which are located throughout the ring. Equation 3.4 shows that as the energy of the electrons increases, the magnetic field must also increase in order to keep the beam orbiting at the same radius. It is the synchronization of the acceleration and the magnetic field strength that gives the synchrotron its name. The acceleration in the synchrotron is achieved by injecting a traveling RF wave into cavities as the particle enters. One consequence of this is that the synchrotron can only accelerate electrons or positrons at one time. To change from one to the other, the RF power is switched to enter the other end of the accelerating structure. It takes a few thousand times around the synchrotron (only a few milliseconds) for the beams to reach the desired energy at which point they are injected into the storage ring. The injection cycle begins by filling the storage ring with positrons, then electrons. Once both counter-circulating beams are in the storage ring are they brought into collision.

3.1.3 Storage Ring

In the storage ring, the beams are steered into a circle by 86 dipole magnets. Interspersed among the dipoles are 98 quadrupole magnets which are responsible for steering errant particles back onto their design orbit. Each quadrupole magnet has the effect of focusing the beam in one dimension while defocusing it in the other. By alternating the orientation of the quadrupoles, overall, the beam is steered back onto its design orbit. Sextupole magnets are placed in the ring to

correct for energy dependent effects from the quadrupole magnets.

Originally, CESR was designed to circulate a single bunch of electrons and a single bunch of positrons. These two bunches would collide in two places on the ring, in the North and South Experimental Areas. The North area was the location of the CUSB detector, and the South area is home to CLEO. Thanks in part to the fact that all of the particles in each bunch are actively repelling one another, there are limits to the number of particles which can be crammed into each bunch. To increase the current in the ring, CESR was required to begin multi-bunch operation. Of the many complications this creates, perhaps the simplest to understand is that of so-called parasitic crossings. Now with multiple (N) counter-rotating bunches, there are crossings at $2N$ points around the ring, only one of which is located inside CLEO. To remedy this, electrostatic separators were introduced to deflect the beams from their central orbit. These separators place an electric field across the beam, deflecting the positrons one way, while deflecting the electrons the other. Now both sets of bunches oscillate around the central orbit and pass by one another in what is called a pretzel orbit. The separators are placed so that the pretzel is removed as the beams enter the South Experimental Area, allowing them to collide in CLEO.

Relativistic electrons which are accelerated radiate electromagnetic energy at a rate that is proportional to the square of the force causing the acceleration. For the beams in CESR this electromagnetic radiation is in the form of x-rays known as synchrotron radiation. This emission amounts to a energy loss of ~ 1.2 MeV/turn. This energy needs to be replaced by the CESR RF system in order to keep the

beam in the machine, but this energy loss is well worth the price of electricity to do so. The energy lost to synchrotron radiation has the effect of damping unwanted instabilities that would otherwise build up in the beams. This is crucial for successful beam storage. The characteristic damping time in CESR is 23 ms which is one of the limits on the instability that can be accommodated in CESR. The x-rays produced are also available to the users of the Cornell High Energy Synchrotron Source (CHESS) where all manner of physics, biology, and chemistry are studied.

The CESR RF system has to satisfy many conditions that aren't required in the synchrotron, the simplest is that it must support electron and positron beams circulating in both directions at the same time. To accommodate this, the 500 MHz electromagnetic field oscillates as a standing wave in the cavities. This allows the electrons to be accelerated in one direction while the positrons are accelerated in the other. But, the CESR RF system does more than simply replace the energy lost to synchrotron radiation. It also plays a vital role in shaping the particle bunches[20]. To do this, the bunches are timed to pass through the cavity while the electric field is falling from its maximum value as seen in Figure 3.2. This serves to compact the bunches in the following way. A particle with the proper energy will be on the design orbit and arrive at precisely the right time to get the necessary kick to keep it at the right energy. If a particle's energy is too high, then from Equation 3.4 it must be on an orbit with a larger radius. If this is true, then it will arrive in the cavity late, and since the electric field is decreasing, the particle will be accelerated less. Similarly, particles with too little energy are on a

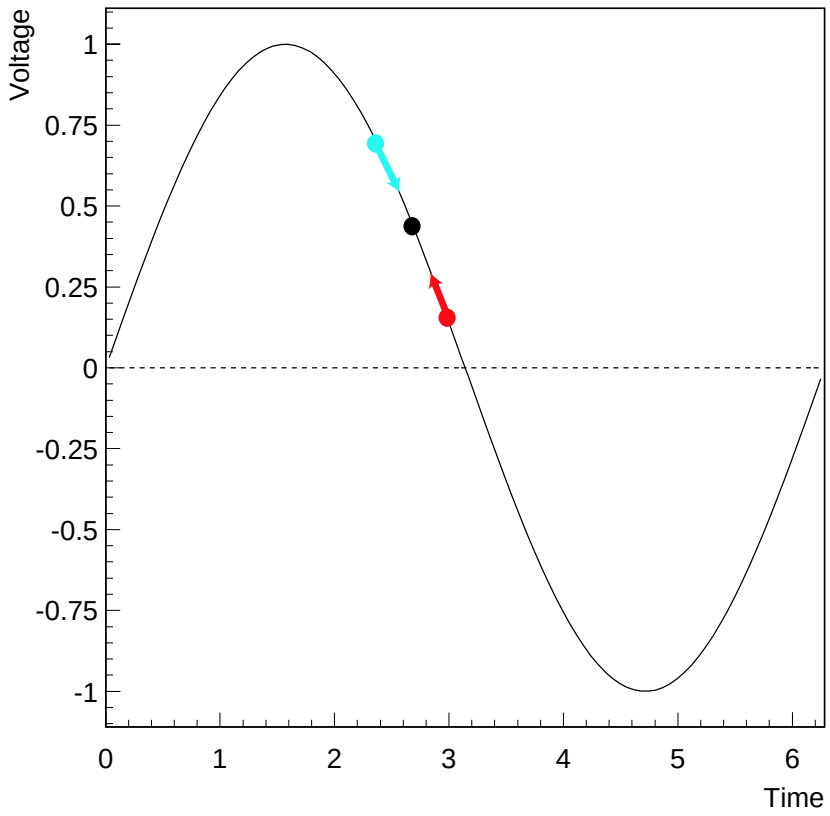

Figure 3.2: The timing of bunches passing through the CESR RF cavities. As explained in the text, a bunch with more energy than the design energy arrives in the cavity late (lower dot) and receives less energy. A bunch with too little energy arrives early (upper dot) and will receive more energy.

tighter orbit and arrive early, and get the extra push they need.

There is one parameter whose importance dwarfs all others and that is Luminosity or roughly the rate of electron-positron collisions at the interaction point. It is described by the following equation [20].

$$\mathcal{L} \propto f \frac{N_B n_{e^-} n_{e^+}}{A_{eff}} \tag{3.5}$$

Here f is the revolution frequency of the bunches which is set by the circumference of the ring, $f = c/768$ m ≈ 390 KHz for CESR. $n_{e^\pm}$ are the numbers of particles in each bunch and N_B is the number of bunches. For the CESR operating mode where there were 9 trains of 3 bunches the number of particles per bunch was $\sim 10^{11}$. A_{eff} is the effective area of the bunches. This depends on the vertical and horizontal sizes of the beams ($\sigma_h \approx 300$ μm and $\sigma_v \approx 6$ μm) which is generally defined by the strength of the final focusing magnets, the bunch length, which is limited by the RF gradients, and the crossing angle. Unfortunately, this equation predicts luminosities that are larger than those observed. This is due to the fact that Equation 3.5 neglects the more complicated beam dynamics present in the storage ring, like beam-beam interactions. Trying to understand and compensate for these effects is one of the areas of study pursued by accelerator physicists.

3.2 The CLEO Detector

Though the Accelerator Complex at Wilson Lab is itself both a technological marvel and a source of scientific study, without a detector, we would never know if we were producing interesting physics, let alone be able to study it. CLEO, a

collection of sub-detectors whose layers are wrapped around the south interaction point of CESR, opens a window onto the fundamental constituents of matter.

The CLEO detector has existed in several configurations over its more than twenty year history. The data used for this analysis were collected using the CLEO II (1989-1995) [21] and CLEO II.V (1995-1999) [22] configurations. CLEO is a general purpose solenoidal detector enclosing $\sim 95\%$ of the 4π solid angle. This hermeticity has allowed the development of analysis techniques, like the one described here, which rely on the reasonable expectation that the entire event is contained in the active volume of the detector for the vast majority of events. The basic design of CLEO has charged particle tracking surrounded by a time of flight system and an electromagnetic calorimeter. This is then enclosed in a superconducting solenoid magnet surrounded by an iron return yoke interspersed with muon identification chambers. The CLEO II configuration can be seen in Figures 3.3 and 3.4. The CLEO II.V configuration saw the innermost tracking chamber replaced with a silicon vertex detector and a change in the gas used in one of the tracking chambers as described in Section 3.2.2.

Different particle species interact differently with matter, and CLEO's different detector elements are designed to take advantage of these interactions in order to measure the kinematic properties of the particles which pass through them. The goal is to have enough information to be able to reconstruct the physical processes which follow the electron-positron annihilation. This section first briefly describes the primary processes by which these particles interact with matter, then goes on to describe how CLEO's various sub-detectors use these processes to measure the

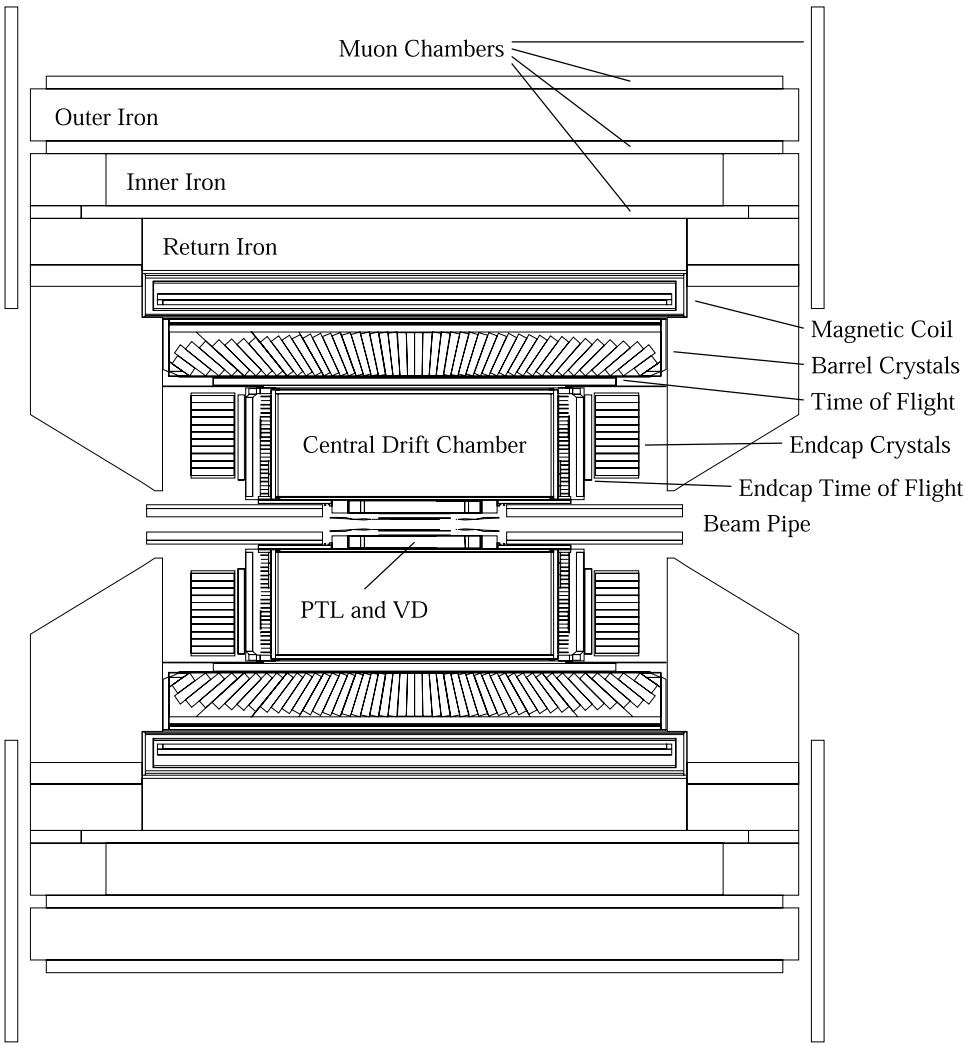

Figure 3.3: Side view of the CLEO II Detector

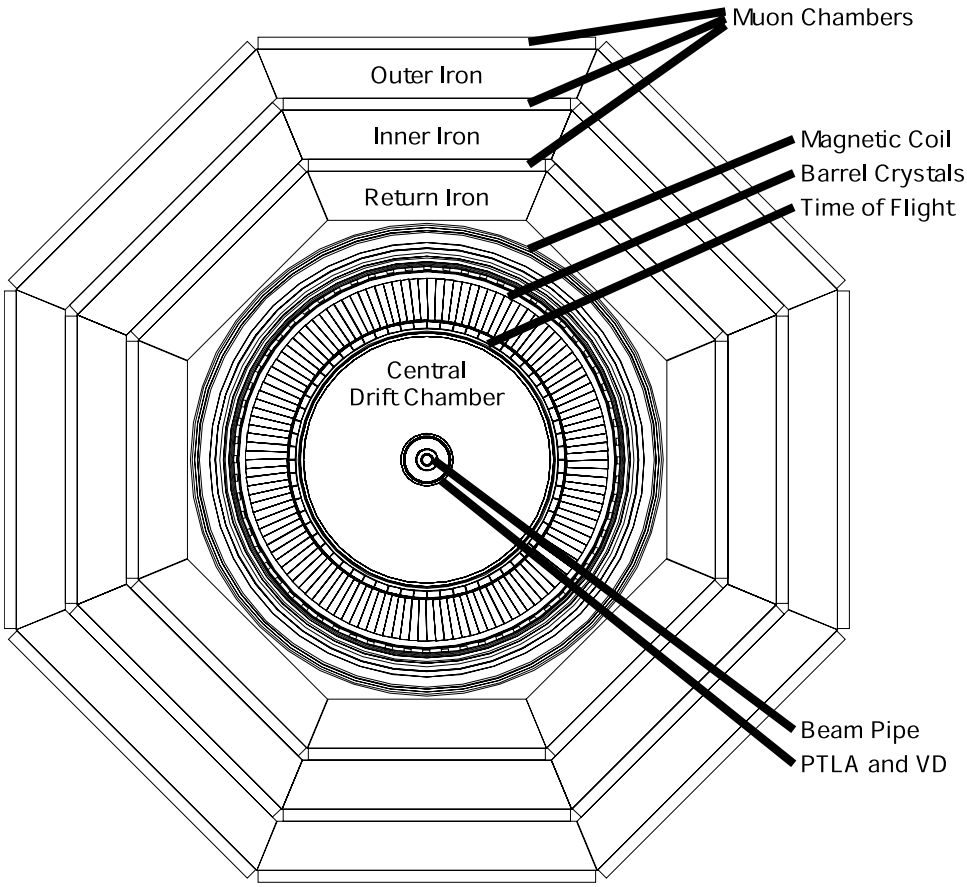

Figure 3.4: End view of the CLEO II Detector

kinematic properties of the particles that traverse them.

3.2.1 Interaction of Particles with Matter

There are two things that can happen to charged particles as they pass through material[23, 24]. They can lose energy to the material and they can change direction. Likewise, photons can be scattered and absorbed. When dealing with the passage of particles through matter, it is useful to deal separately with electrons (and positrons), heavier charged particles, and photons. As CLEO has no hadronic calorimeter, we will not discuss the interactions of neutral hadrons. We will see that in the charged particle tracking system, CLEO physicists correct for the effects of scattering and energy loss of charged particles in the tracking chambers and use the energy loss as a method particle identification. Further, the energy loss of electrons and photons in the electromagnetic calorimeter provide vital information for the reconstruction of physics at CLEO.

Scattering of Charged Particles

The scattering of charged particles is dominated by Coulomb scattering from the nuclei in the detector material. The vast majority of these interactions result in small angular deflections of the particle with negligible energy loss. As the particle slaloms past the nuclei, these small deflections result in an overall change in the particle's direction. This process is called multiple scattering and calculations result in a probability distribution of the net deflection of a particle traversing a given thickness of material.

Energy Loss of Charged Particles

For heavy charged particles, inelastic collisions with atomic electrons in the medium are primarily responsible for the loss of energy. When a heavy charged particle collides with an atomic electron, its direction is not usually altered, but energy is transferred to the electron, sometimes enough to free the electron from the atom. Though each individual interaction governed by a quantum mechanical probability, there are many such interactions in a macroscopic pathlength, and the mean energy loss due to ionization can be calculated statistically. Known as dE/dx this quantity is given by the Bethe-Bloch equation, which for particles of unit charge has the form:

$$-\frac{dE}{dx} \sim K_1 \frac{1}{\beta^2}\left[\ln\left(K_2 \frac{\beta^2}{1-\beta^2}\right) - 2\beta^2\right] \tag{3.6}$$

where the constants K_1 and K_2 are largely dependent on the medium. The $1/\beta^2$ dominates at low β, but at around $\beta = 0.96$, there is a minimum, after which the logarithmic term takes over. Particles at the minimum energy loss are called minimum ionizing particles. The portion of the curve past the minimum is called the relativistic rise. Plots showing dE/dx for different particle species will be shown in Section 3.2.2. (For a thorough description of the Bethe-Bloch equation, see Reference [23] or Section 26 of Reference [24].)

Electrons (and positrons), being charged particles themselves, also lose energy by ionizing the material, but the Bethe-Bloch equation needs modification for two reasons. For electrons at least, there are quantum mechanical consequences of the indistinguishability of the atomic electron and the electron being scattered.

For both electrons and positrons the interaction is with atomic electrons, and it is no longer appropriate to neglect the deflection of the incident particle. So, electrons scatter off atomic electrons in addition to the atomic nuclei as previously mentioned. The scattering of a charged particle can cause that particle to emit radiation, and the emission probability scales with the inverse square of the mass of the scattered particle. For electrons and positrons in the energy regime of CLEO this leads to bremsstrahlung, literally braking radiation. A plot of the relative contributions to dE/dx of ionization loss and bremsstrahlung can be seen in Figure 3.5.

Photons

The photon's lack of electrical charge precludes its participation in inelastic interactions with atomic electrons. There are, however, three other processes which govern the interactions of photons. They are the photoelectric effect, Compton scattering, and pair production. The cross sections for these three processes as a function of energy are shown in Figure 3.6.

The photoelectric effect is the absorption of the photon by an atomic electron which results in the ejection of the electron. A free electron cannot absorb a photon while conserving momentum and energy, so the photoelectric effect can only be seen in bound electrons with the atomic nucleus recoiling to satisfy energy-momentum conservation. As can be seen in Figure 3.6, for relatively low photon energies (low for CLEO, that is) there is structure associated with the atomic electron energy levels, but above the highest binding energies, the cross section falls off.

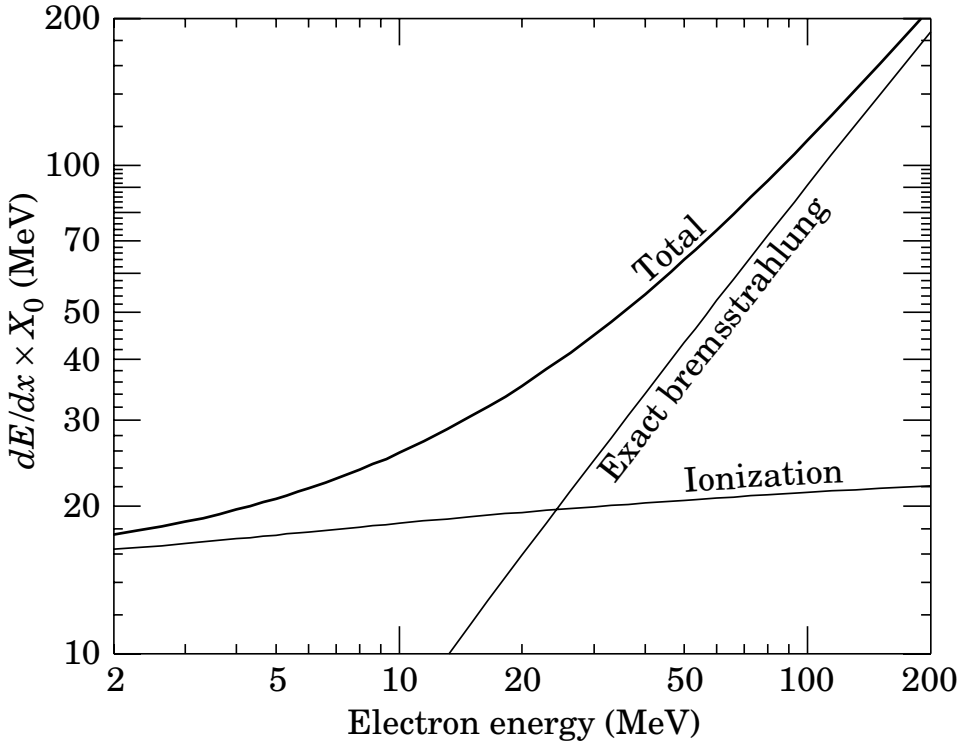

Figure 3.5: Electron energy losses due to ionization and bremsstrahlung. Adapted from Ref. [24]

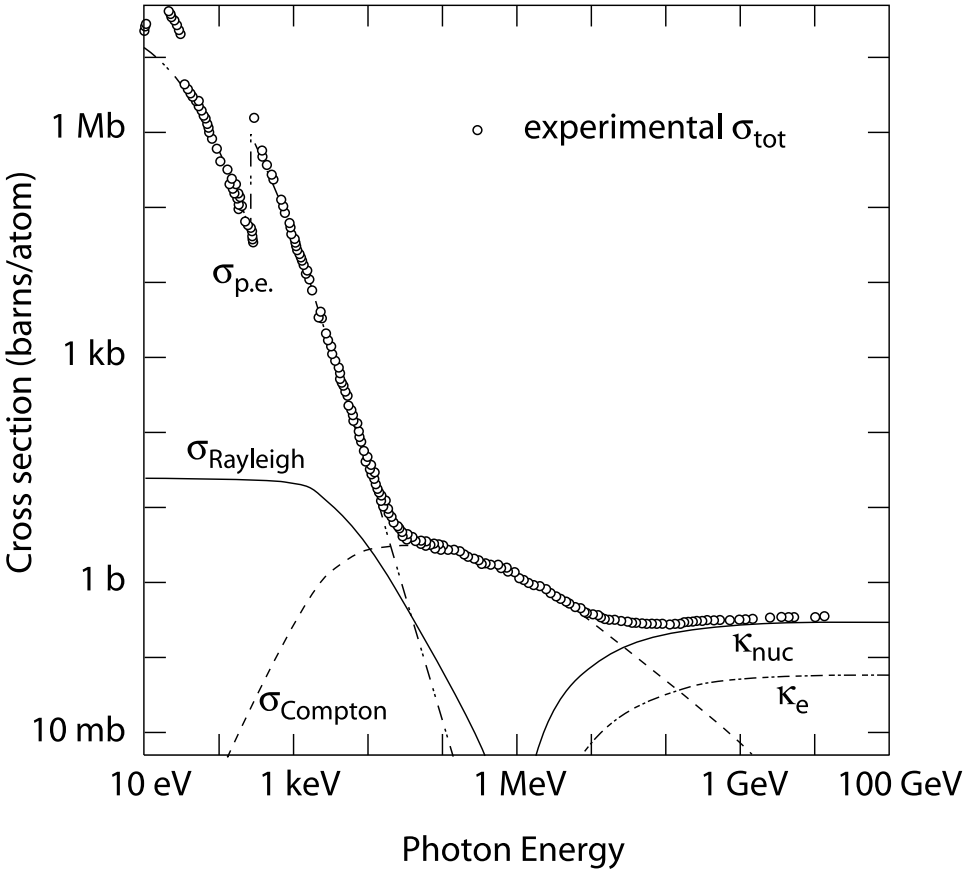

Figure 3.6: The total photon cross section and its components, where $\sigma_{p.e.}$ is the atomic photoelectric effect, $\sigma_{Rayleigh}$ is coherent scattering, $\sigma_{Compton}$ is incoherent scattering, and κ_{nuc} and κ_e are pair production in the nuclear and electron fields. Adapted from Ref. [24]

Compton scattering occurs when a photon interacts with a free electron. (The free electron approximation is good for atomic electrons when the photon energy is sufficiently large compared to the electron's binding energy.) In this process the photon loses energy to the electron, but is not absorbed.

By far, the most important photon interaction process at CLEO is pair production. To create an electron-positron pair, the photon needs to have enough energy (2×0.511 MeV $= 1.022$ MeV) and there must be a third body to conserve momentum and energy. As can be seen in Figure 3.6 the cross section for pair production dominates at large photon energies.

3.2.2 Charged Particle Tracking

Drift Chambers

Since the charged particle tracking in CLEO is achieved by three concentric wire drift chambers, a brief mention of how these devices work[25] is in order. Drift chambers are ionization detectors designed to precisely measure the position of an ionizing particle's path relative to an anode sense wire. A drift chamber is divided up into drift cells which each contain an anode sense wire embedded in an electric field. In the case of the CLEO drift chambers, the drift cell is enclosed by either a conducting tube or a field wire cage and the electric field is generated by placing a high positive voltage on the anode wires, and grounding the field wires/tube.

A electric field in a generic drift chamber has two basic characteristics. Away from the wire the field is uniform, but closer to the anode wire, the field increases

rapidly. Both of these characteristics are important to the functioning of a drift chamber. Imagine a charged particle passing through the drift cell. As described in Section 3.2.1, this particle leaves a path of ionization in its wake. The liberated electrons(ions) are then pulled towards the anode(field) wires. If the electric field shape is well understood, the speed at which the electrons drift is described by a known drift function. As the electrons approach the sense wire, the increased electric field causes the primary ionization electrons to gain sufficient energy to ionize more gas. These secondary electrons cause further ionization and an avalanche forms. This results in a "gas gain" resulting in a measurable signal on the sense wire.

There are two important properties of this signal that can be measured. The time of arrival of the ionization at the sense wire will allow us to calculate the position of the track in the cell, and the size of the signal will allow us to calculate the amount of primary ionization created by the track. Using information about the time that the particle passed through the cell (called t_0), the time of arrival of the signal on the sense wire, and the known drift function, the distance from the sense wire to the track can be calculated. If we know the magnitude of the gas gain, we can calculate the amount of primary ionization from which we can extract the amount of energy the particle deposited in the cell. In a multilayer device, the change in the amount of ionization allows a measurement of energy loss along the path of the particle (dE/dx) which can be used in particle identification as described in Section 3.2.2.

Precision Tracker

As seen in Figure 3.3, the innermost drift chamber is the Precision Tracker (PT) which is shown in more detail in Figure 3.7. The PT is a six layer straw tube chamber whose sole purpose is to determine particle directions and separate primary and secondary vertices by precisely measuring the $r-\phi$ positions of the tracks close to the interaction point. Each layer contains 64 15 μm gold plated tungsten wires surrounded by an aluminized mylar tube. In order to allow the sides of the cells to touch, the radial size of the tubes range from approximately 2 mm for the inner layer to 4 mm in the outer layer. Further, each layer is offset from the previous one by half the cell width to resolve the ambiguity of which side of the sense wire the particle passed.

Silicon Vertex Detector

The PT was removed for the CLEO II.V era in favor of a 3 layer double sided Silicon Vertex detector (SVX)[22] which is shown in Figure 3.8. Though not a drift chamber, this solid state device also measures the position of charged particle tracks by the detection of ionization. The electron-hole pairs are detected by electrical signals induced on traces placed directly on the detector surface. The nature of the manufacturing process allows the readout strips to be placed very close together ($\sim$ 100 μm for the CLEO SVX.) The SVX allows for even more precise discrimination of secondary vertices, which is vital for many CLEO analyses. However, for this particular analysis, the difference is not significant.

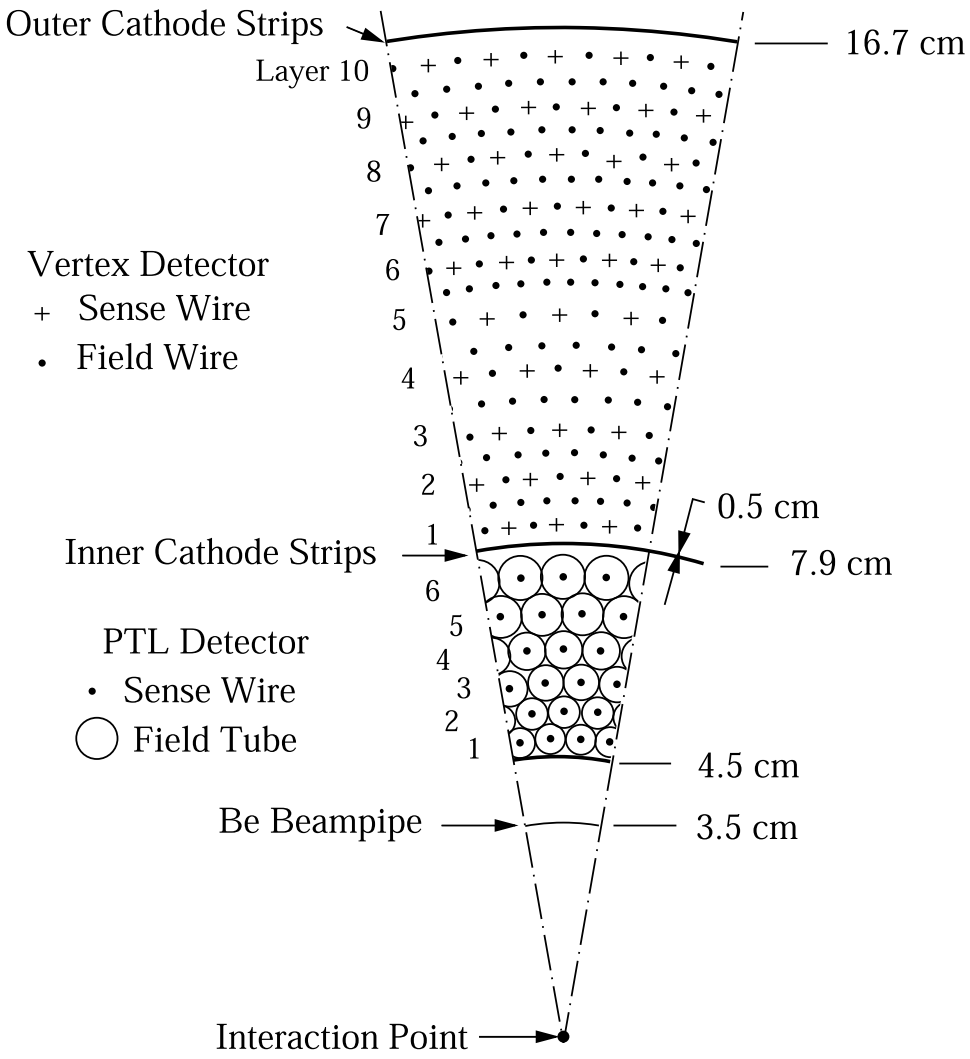

Figure 3.7: The Precision Tracker (PT) and Vertex Detector (VD).

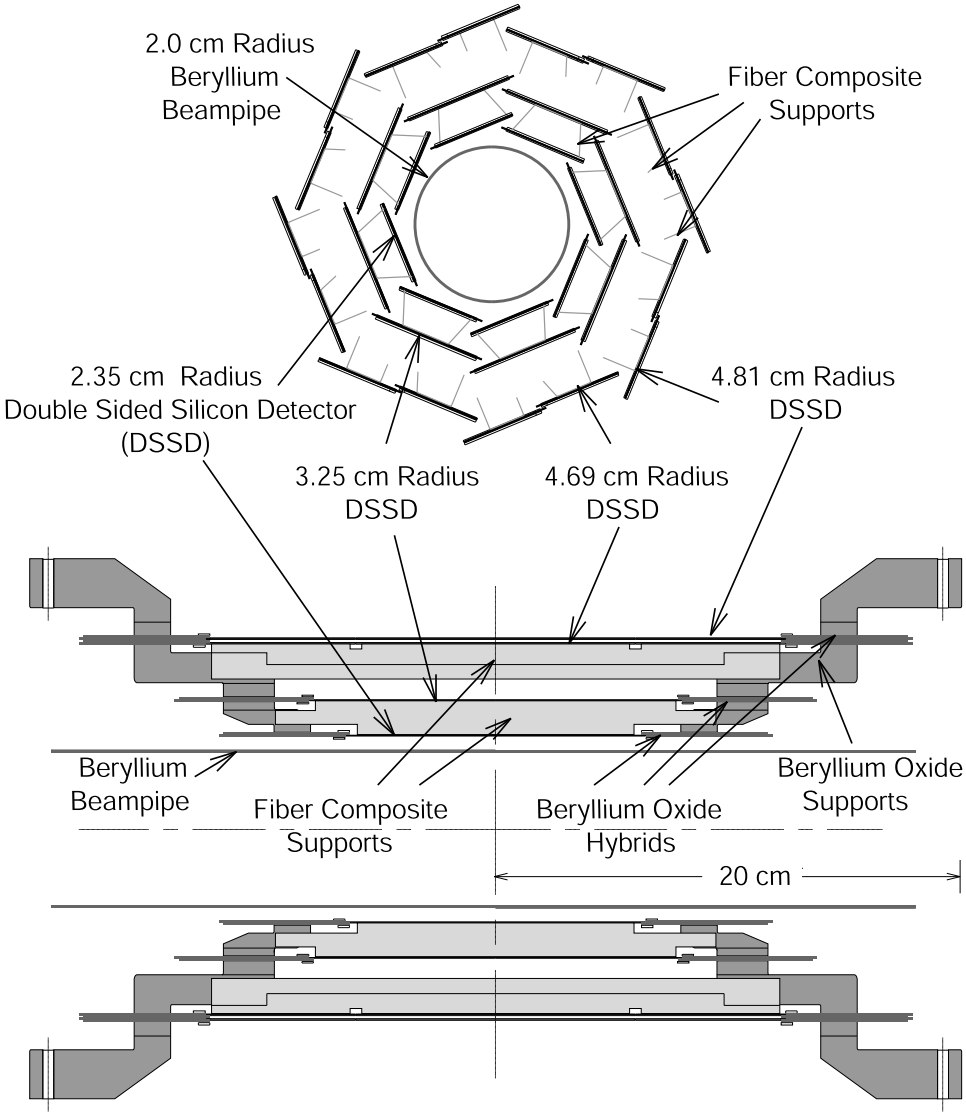

Figure 3.8: The CLEO II.V Silicon Vertex Detector.

Vertex Detector

Outside the PT/SVX from radii 8.1 cm to 16.4 cm is the Vertex Detector (VD). The VD was originally built for CLEO-1.5 in 1984 and enabled the reconstruction of decay vertices of charmed mesons and taus [26]. A portion of the VD cell structure can be seen in Figure 3.7. There are 10 layers, the inner 5 containing 64 cells and the outer 5 containing 96. The field is shaped into hexagonal cells by 3 field wires per sense wire. The VD design includes some features not found in the PT, for example, the field in the innermost and outermost layers are shaped by segmented cathode surfaces on the inner and outer skins of the chamber. These segments (aluminum bonded to mylar) are arranged as 5.85 mm(6.85 mm) pads along the beam axis (the "z-direction") on the inner(outer) cathode sheets and segmented into 8 azimuthal sections as seen in Figure 3.9. This arrangement is such that the image charge of the avalanche on the sense wires are spread over 3 pads which can be read out to determine the position of the track along the length of the chamber. Another trick to extract z information is called charge division. The sense wires are made of a nickel-chromium alloy which has three times the resistivity of gold plated tungsten. Each wire is read out at both ends, and due to the resistance in the wire, the amplitude of the signals at either endplate can be used to determine the z position of the track on the wire.

Drift Chamber

The outer drift chamber or DR consists of 51 layers stretching from a radius of 17.5 cm to 0.95 m and is the main tracking volume. There are a total of 12240

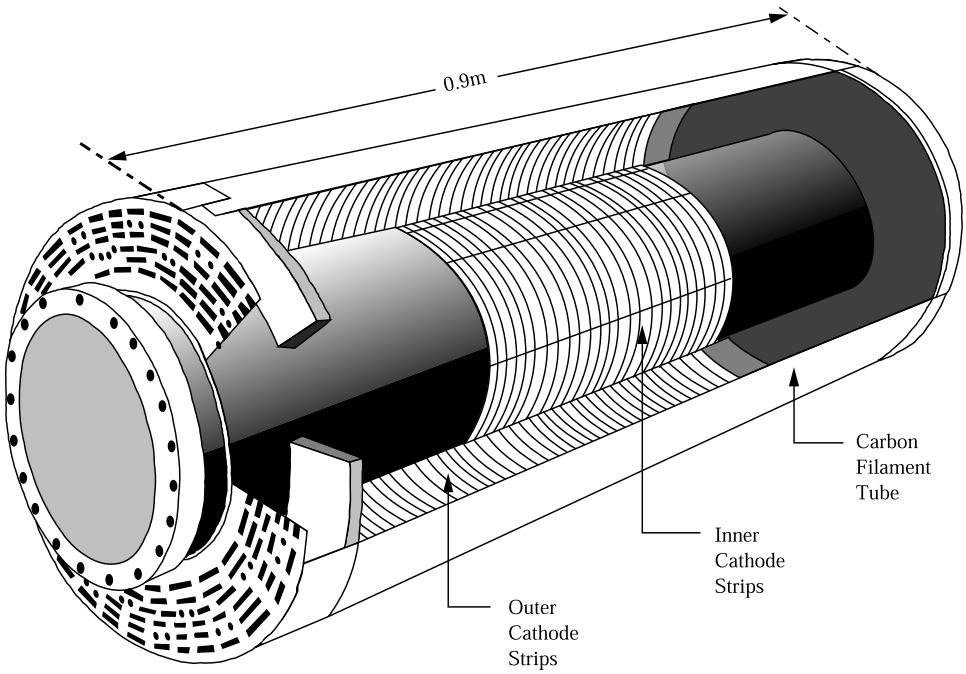

Figure 3.9: Arrangement of the cathode strips in the Vertex Detector.

rectangular cells formed by 36240 field wires. The cell geometry can be seen in Figure 3.10. As in the VD, there are instrumented cathode pads on the inner and outer surfaces, but there is yet another drift chamber trick to retrieve z information. 11 of the layers are not strung axially, but rather with a slight angle. These stereo layers are interspersed between groups of 3 or 5 axial wires and alternate the direction of the stereo angle. When a track passes through the chamber, there should be only one z position at each stereo layer that will result in a continuous reconstructed track. In the CLEO II.V era, the gas in the drift chamber was changed from a 50 : 50 mixture of Argon and Ethane to a 60 : 40 mixture of Helium and Propane. The change in gas decreased the amount of multiple scattering in the DR volume, and the decrease in drift velocity resulted in improved spatial resolution [27].

Superconducting Solenoid

The entire central detector is enclosed in a superconducting solenoid magnet which can be seen in Figures 3.3 and 3.4. The design specification for the magnet called for the 1.5 T field to be uniform to $\pm 2\%$ over 95% of the solid angle of the drift chamber volume. The field was measured to be uniform to 0.2%[21]. Field uniformity is important as it allows for a better knowledge of the drift functions in the tracking chambers and therefore better tracking resolution. The purpose of the magnetic field is to bend the paths of charged particles in the tracking chambers. As we saw in Section 3.1.1 the radius of curvature of a charged particle in a magnetic field is proportional to its momentum. Thus the magnetic field al-

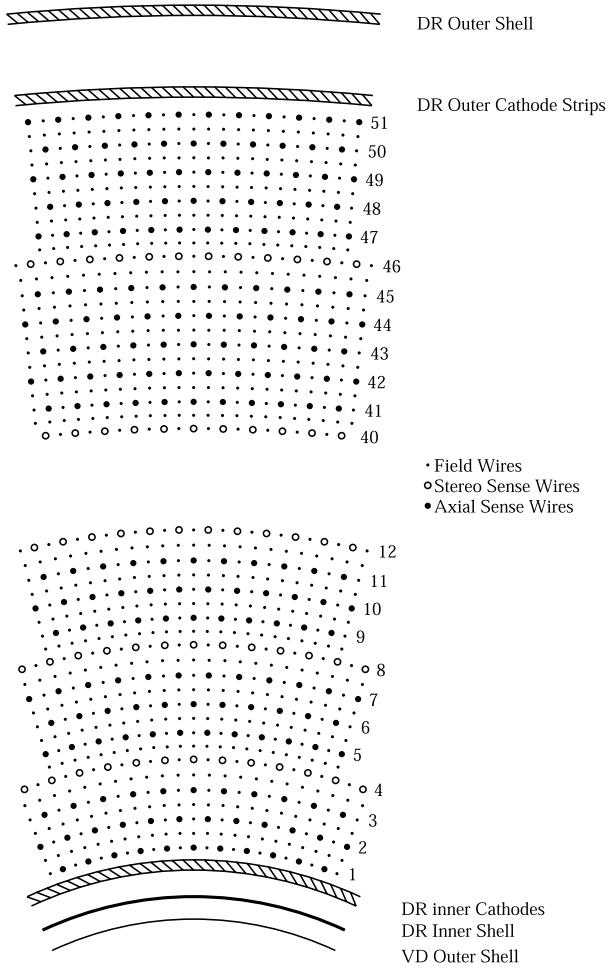

Figure 3.10: Drift Chamber cell geometry.

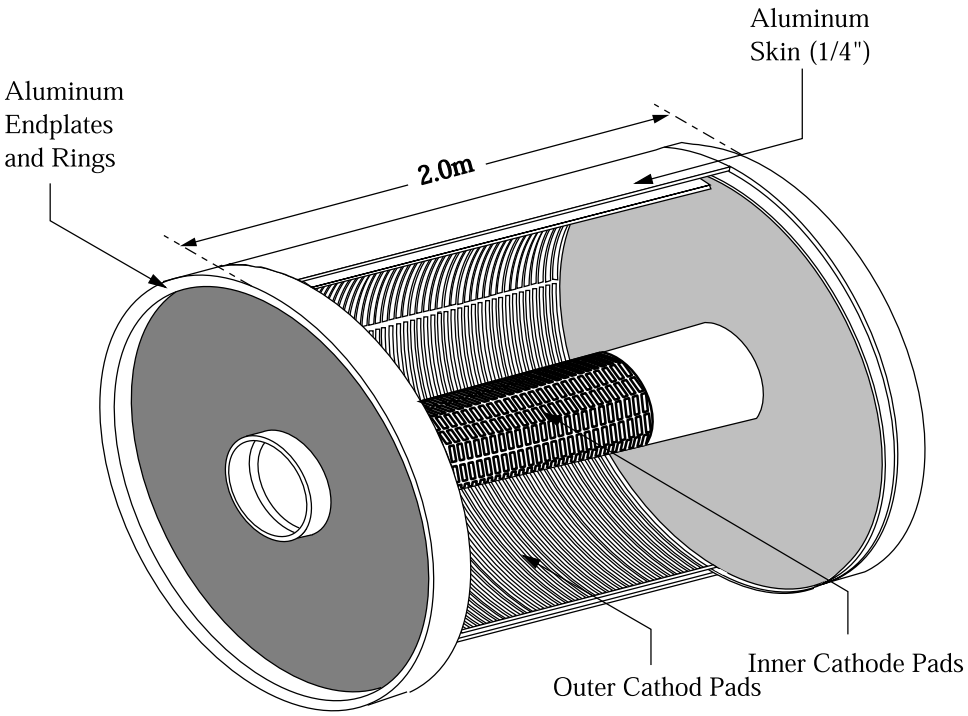

Figure 3.11: Drift Chamber cathode placement.

lows our tracking system to make momentum measurements. The electromagnetic calorimeter is also inside the magnet. This prevents particles from having to pass through the significant amount of magnet material prior to calorimetry as was the case for CLEO I.

Time of Flight

We discuss the physics of scintillators in Section 3.2.3. The time of flight (TOF) system is a cylinder of 64 plastic organic scintillation devices in the barrel section of CLEO and 28 wedge shaped devices on each endcap as seen in Figures 3.3 and 3.4. These are then connected to photomultiplier tubes which measure the amount and timing of light pulses in the scintillator which mark the passage of charged particles. The TOF system serves two basic purposes, the first is as an input to the trigger system which initiates data taking. The second is as a particle identification tool. Both of these tasks will be described in later sections.

Muon Chambers

Muons are the only charged particles able to pass through the material of the inner detectors, the solenoid, and magnet flux return iron. In order to identify these particles, triplets of wire chambers are placed at 3, 5, and 7 radiation lengths interspersed with CLEO's outer iron as seen in Figures 3.3 and 3.4. A view of a muon chamber can be seen in Figure 3.12. Each chamber gives position measurements in the two planar directions, allowing for tracks from the central detector to be matched to them. The resolutions are on the order of centimeters which

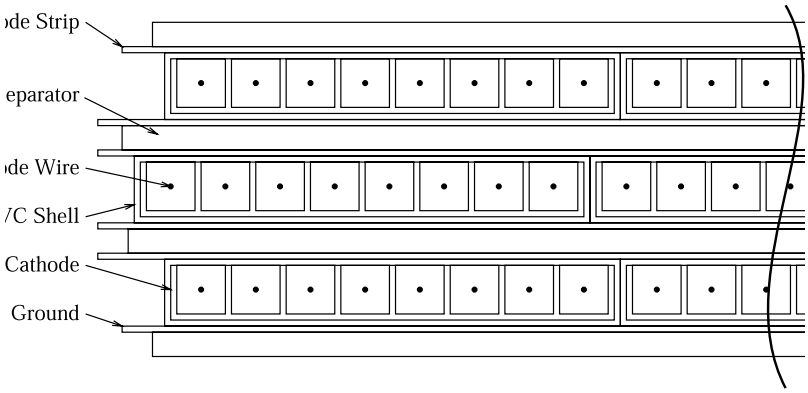

Figure 3.12: Muon chamber

proves sufficient for this purpose. Because muons can range out before exiting the detector, the identification is only reliable above 1.5 GeV.

Track Fitting

Transforming hits on wires into tracks is done in two steps. First, hits that are likely to belong together on a track or part of one are grouped together by the track finder. Then, the track fitter finds the best track parameters which describe the motion of the particle through the tracking chambers. As described in Section 3.2.1, the particles undergo energy loss and scattering as they pass through the tracking chambers and the track fitting algorithm (an implementation of a Kalman filter [28, 29]) takes this into account. One of the consequences of this is that the fitter needs to be run for each of the possible mass hypotheses (e, μ, π, K, and p) as the energy loss is different for each of them. In the end the goal is to have the track

parameters describing the initial momentum of the track and the associated error matrix for each mass hypothesis.

Vertex Finding

Having well fit tracks is only half of the battle when it comes to particles that decay within the tracking chambers like K_S and Λ particles. In the dark ages of so called vee finding, this involved simply looking for tracks which crossed in the $r - \phi$ projection, and placing the vertex where the tracks crossed. With the use of the Kalman filter, in addition to the track parameters, the error matrices can be used in the vee finding process. The technique of kinematic fitting [30, 31] also includes constraints based on the mass of the particle to be reconstructed.

Particle Identification

The identity of a particle is defined by its mass, and there are two basic tools used at CLEO to facilitate the identification of charged particles. Both are methods of measuring the speed (β) of the particle in question. Combined with the momentum of the track measured in the drift chamber, the mass of the particle can be calculated and the particle identified. The time of flight system is the more straightforward of the two.

The TOF system uses the CESR beam crossing time and the signal from the passage of the charged particle through the scintillator to calculate the time taken for the particle to travel from the interaction point to the detector. Since the path of the particle is known from the tracking system, the speed β of the particle is

known. A plot of $1/\beta$ versus momentum can be seen in Figure 3.13. The bands formed by the different particle species are clearly seen. This technique is limited by the ability to accurately measure the very short time intervals for the highly relativistic particles to travel the ~ 1 m from the IP to the TOF scintillators.

The second method of measuring β comes from dE/dx. From the Bethe-Bloch (Equation 3.6) we know that the energy lost by a charged particle to ionization in the tracking chambers is primarily a function of β. For a track that passes through all 51 layers of the DR, there are 51 measurements of the ionization and from this dE/dx can be calculated. When plotted against the momentum of the track the results can be seen in Figure 3.14.

The particle identification (PID) information for these two measurements is presented in the following way. For each of the candidate particle hypotheses for a given track the following quantity is defined:

$$\chi_{PID^h} = \frac{PID^h_{measured} - PID^h_{predicted}}{\sigma(PID^h_{measured})} \tag{3.7}$$

where $PID^h_{measured}$ is the measured particle identification value, either dE/dx or TOF. $\sigma(PID^h_{measured})$ is the error on that measurement, and $PID^h_{predicted}$ is the value expected for each particle hypothesis $h = e$, μ, π, K, or p.

3.2.3 Electromagnetic Calorimetry

Scintillators

Scintillating materials are those which are able to convert absorbed energy (like ionization from the passage of a charged particle) to near optical photons. These

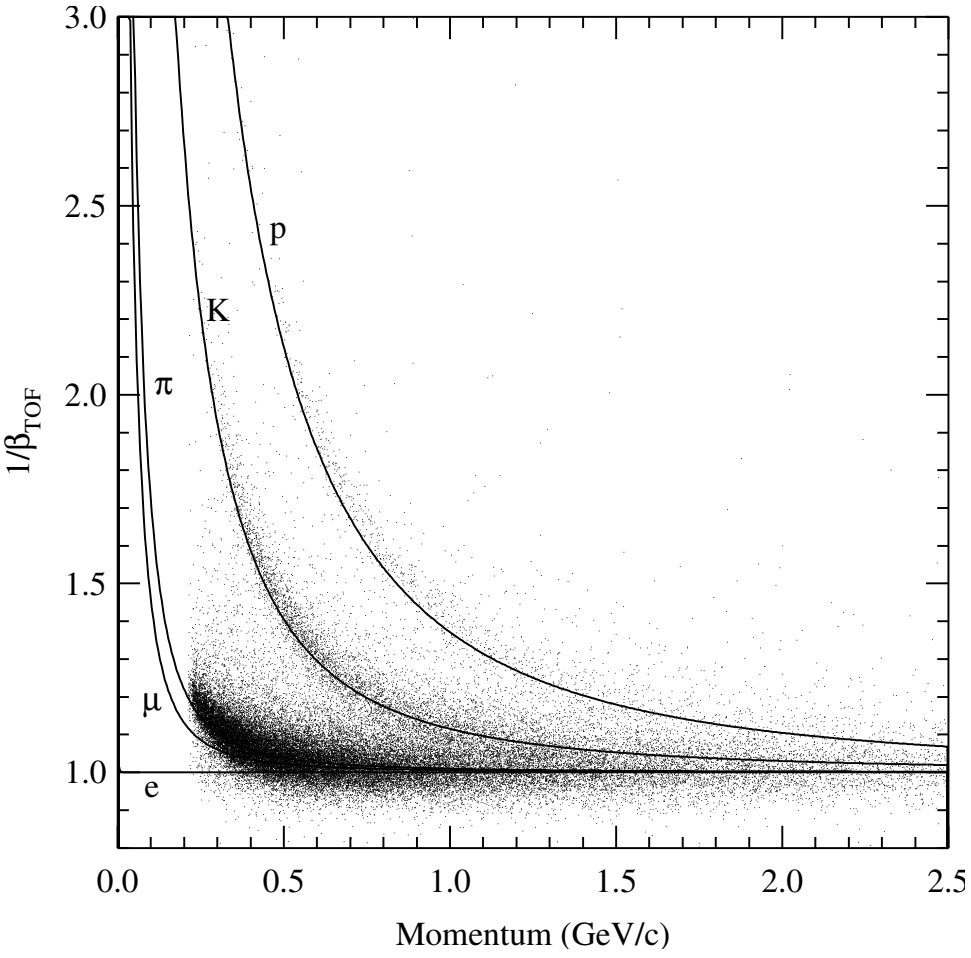

Figure 3.13: $1/\beta$ as measured by the TOF system versus momentum from the tracking system. Where p, K, π, μ, and e, are the particle species: proton, kaon, pion, muon, and electron.

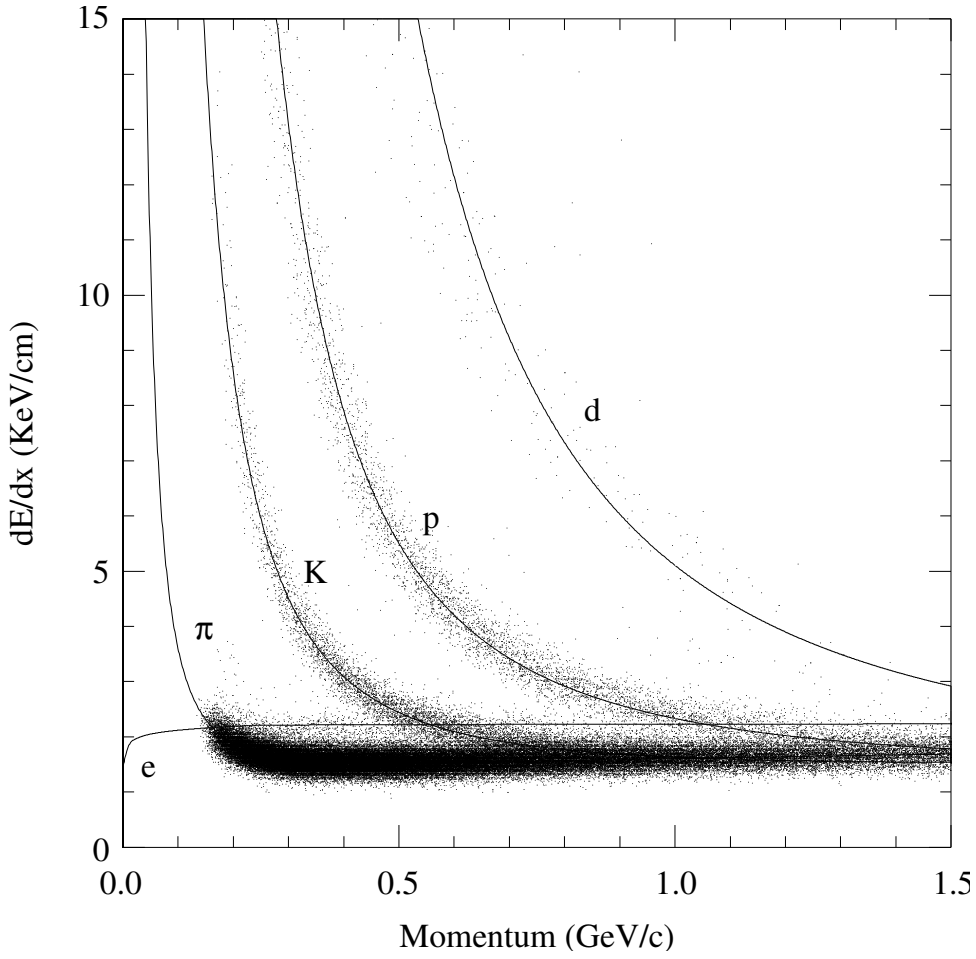

Figure 3.14: Measured ionization loss versus momentum in CLEO II. Where d, p, K, π, and e are the particle species: deuteron, proton, kaon, pion, and electron.

photons are then detected with photomultiplier tubes (PMTs) or photodiodes. The two classes of scintillating materials used in CLEO are the organic plastic scintillators used in the TOF system and the inorganic crystal scintillators used in the crystal calorimeter.

In organic scintillators, the light production mechanism proceeds in more than one step. With the passage of the charged particle, valence electrons are excited, and some organic compounds (mainly those with aromatic rings) will release some of this energy ($\sim$ 3%) as optical or ultra-violet photons. One disadvantage of organic scintillators it that the light production does not scale linearly with ionization, which makes them less useful as calorimeters. However, their fast response time and the ease with which they can be machined make them attractive for a trigger or time of flight systems. Most of the time, the scintillator is further doped with compounds which fluoresce, or absorb the UV light, and re-emit photons in the optical range. There can be several steps of fluorescence as the wavelength of the emitted light is shifted to a reasonable value. In the end, a substance can be chosen based on several properties including the efficiency with which absorbed energy is transformed to fluorescent radiation, the substance's transparency to the produced light, the spectrum of the produced light, and the decay constant associated with the light production.

Inorganic crystal scintillators have several advantages over organic/plastic scintillators in the realm of calorimetry. Among these are higher densities and linear light output with energy deposited. The light production in an inorganic crystal is a product of the band structure of the crystal. Charged particles can create

electron-hole pairs which, aided by impurities, produce light when they de-excite. In CLEO, inorganic crystals are used for electromagnetic calorimetry, by which the energy of high energy electrons and photons are measured. (Primarily photons, which are not detected by any of the ionization detectors.) As was described in Section 3.2.1, a high energy photon will undergo pair production, which results in the creation of a high energy electron-positron pair. These both can radiate more high energy photons via bremsstrahlung, the cycle repeats. This electromagnetic shower develops and the crystal will emit photons in proportion to the amount of energy lost by the electrons in the shower. If the crystal is thick and dense enough to contain the entire shower, the light output will be proportional to the energy of the incident photon or electron.

Crystal Calorimeter

The CLEO electromagnetic calorimeter, the Crystal Calorimeter (CC), is divided into three parts: the barrel and two endcaps. It is constructed using thallium-doped cesium iodide crystals. CsI(Tl) has a high density of 4.51 g/cm^3, a short radiation length of 1.83 cm, and a Molière radius of 3.8 cm. (The Molière radius is the characteristic lateral size of an electromagnetic shower.) The size of the crystals reflects a balance of several competing needs. Those of energy and position resolution and cost. The crystals need to be long enough to ensure that showers in the CLEO energy regime are fully contained, but it is harder to collect all of the produced light in longer crystals. The lateral dimensions are driven by the need for good position resolution. Small crystals would give good position information,

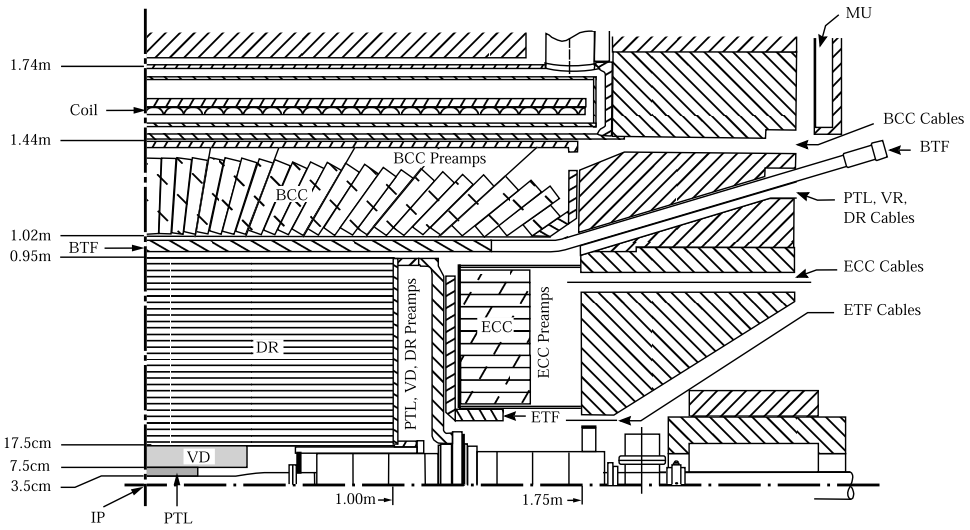

Figure 3.15: Quarter section of the CLEO II detector showing the orientation of the crystals in the Crystal Calorimeter.

but would require more crystals to contain each shower, which would degrade the energy resolution. In the end the crystal size chosen was approximately 5 cm (2.7 r.l.) square by 30 cm (16 r.l.) long [21].

The quarter view of CLEO II in Figure 3.15 shows the arrangement of the crystals in the CC. The barrel is made up of 6144 crystals, and each endcap contains 828. As can be seen in Figure 3.15, the crystals in the barrel are oriented in such a way as to point at the interaction point. (Though it should be noted that the gaps between the crystals do not!) This is so that photons from the IP strike the face of the crystal normally, and the showers develop down the long axis of the crystal. The light is collected by four photodiodes on the rear face of each crystal. Each photodiode is connected to a separate preamplifier and the analog outputs

of these preamps are then added together and shaped outside the detector volume before being measured by an analog-to-digital converter. This arrangement allows for the failure of a photodiode, without losing the signals from the others. In the lifetime of the CLEO II and CLEO II.V detectors there were a handful diode failures, but not a single crystal was lost thanks to this redundancy.

Shower Reconstruction

Shower reconstruction begins with the list of hit crystals and their energies. These are then grouped together into clusters in such a way as to minimize the energy resolution. The position of the cluster is then computed by an energy weighted sum of the crystals' geometric centers. This position is then corrected for the incident particle's direction and the depth to which a particle of the cluster's energy is expected to penetrate. The correct placement of the shower position is an important factor in the ability to match the shower to tracks in the central detector. (Obviously a good way to veto showers due to charged particles.) The energy and angular resolution of the CC can be parameterized as follows [21] for photons of energy $E(\mathrm{GeV})$ where θ and ϕ are the polar and azimuthal angles respectively. For the barrel:

$$\begin{aligned} \frac{\sigma_E}{E}[\ \%] &= \frac{0.35}{E^{0.75}} + 1.9 - 0.1E \\ \sigma_\phi[\ \mathrm{mrad}] &= \frac{0.28}{\sqrt{E}} + 1.9 \\ \sigma_\theta[\ \mathrm{mrad}] &= 0.8\sigma_\phi \sin(\theta), \end{aligned} \tag{3.8}$$

and in the endcap:

$$\begin{aligned} \frac{\sigma_E}{E}[\ \%] &= \frac{0.26}{E} + 2.5 \\ \sigma_\phi[\ \text{mrad}] &= \frac{3.7}{\sqrt{E}} + 7.3 \\ \sigma_\theta[\ \text{mrad}] &= \frac{1.4}{\sqrt{E}} + 5.6. \end{aligned} \tag{3.9}$$

Photons from the IP are only one of the things measured by the CC. The CC also excels at the reconstruction of π^0s which decay to two photons in the central detector. Because of the fine segmentation of the CC, the showers from π^0s with energies up to 2.5 GeV can be separately resolved. Merged showers from higher energy π^0s have different lateral shower shapes and can still be identified.

Electron identification can also be done in concert with the tracking chamber. Electrons form electromagnetic showers similar to photons. (There are some differences in lateral shower shapes.) As a result, a measurement of the electron's energy can be made. Combining this with the momentum of the track matched to the candidate shower, the ratio E/p is calculated and for electrons is close to unity. When E/p is augmented by shower shape variables, reasonable electron identification can be achieved.

3.3 The Event Environment

The data for this analysis were recorded at and below the $\Upsilon(4S)$ resonance. The cross section across the first four Υ resonances can be seen in Figure 3.16. The the cross section at the $\Upsilon(4S)$ has but a few components. The most common

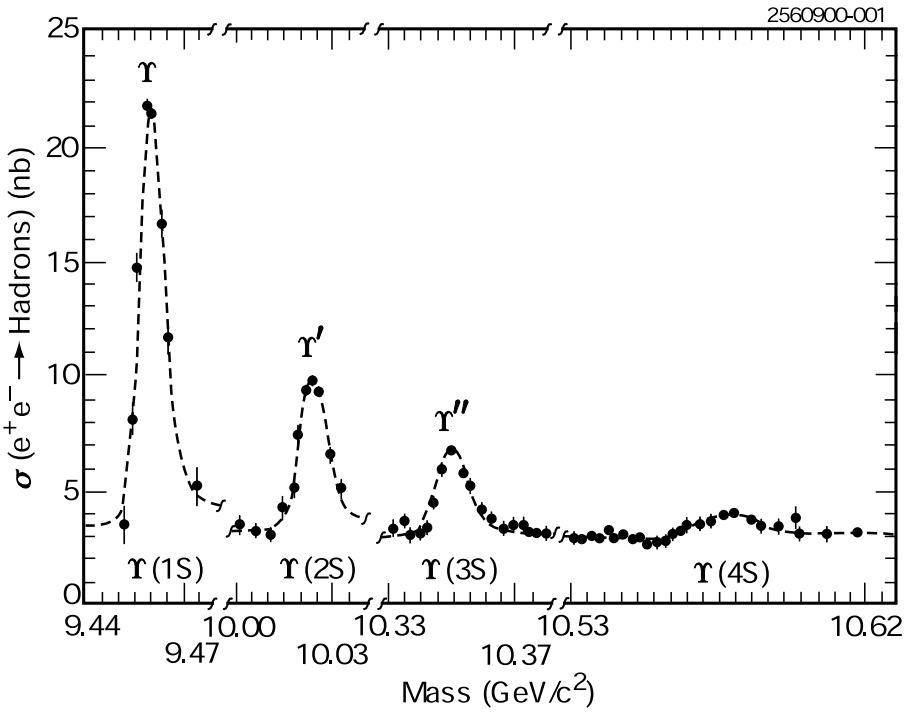

Figure 3.16: The Υ resonances.

interaction is for the electron and positron to scatter off one another in what is known as Bhabha scattering. Even though the physics of Bhabha scattering was worked out long ago, these events are still useful. The Bhabha electrons and positrons have known energy and their interactions with the detector (especially the CC) are a very good source of calibration data. Another well understood process used in calibration is the creation of μ pairs which has a cross section of 0.92 nb. Not to be left out, pairs of τ leptons are also created with a cross section of 0.87 nb, and have been a subject of study for many CLEO physicists.

As for quarks, CLEO physicists refer to the nonresonant creation of pairs of u, d, s, c, quarks as Continuum which has a cross section of 2.59 nb. For this analysis, the continuum represents one of the two largest sources of background. One way that many analyses deal with continuum is by using data taken at energies below the $\Upsilon(4S)$ where the production of B mesons is forbidden. This assumes that the continuum production at the resonance is the same as below. (After taking into account the energy scaling.)

The $\Upsilon(4S)$ is a resonance of a $b\bar{b}$ quark pair. The cross section for producing the $\Upsilon(4S)$ is 1.05 nb. The threshold for creating B meson pairs is just below the peak of the $\Upsilon(4S)$, and as a result the branching fraction for $\Upsilon(4S) \rightarrow B\bar{B}$ is over 96% [24]. At CLEO, the $\Upsilon(4S)$ is created at rest and the B mesons have a very small momentum ($\sim$ 350 MeV). This creates the difficulty that the decay products of the B and $\bar{B}$ cannot be trivially separated. In the ten years of the CLEO II and II.V era, nearly 10 million $B\bar{B}$ pairs were created for industrious CLEO physicists to examine.

CHAPTER 4

FULL EVENT RECONSTRUCTION

The three body decay $B \to K\nu\bar{\nu}$ is the acme of simplicity, a single kaon accompanied by two invisible neutrinos. Unfortunately, we aren't just looking at a B meson decaying to a kaon of unknown momentum and direction; we are looking at the products of an $\Upsilon(4S) \to B\bar{B}$ decay. Our technique is not to only try to reconstruct the decay $B \to K\nu\bar{\nu}$, but rather to fully reconstruct the decay of the $\Upsilon(4S)$ into both the signal B and the companion B. To avoid having yet another neutrino in the event, we restrict ourselves to reconstructing the companion B in the hadronic modes $B \to D^{(*)}(n\pi)$.

This reconstruction is intended to be loose in order to retain as much signal efficiency as possible. We are not interested in whether we are exactly right about whether we get the details of the companion B reconstruction correct as long as we know that the tracks we use result in a reconstructed B meson. The reason our reconstruction of the companion B is so loose is due to the unique signature of our signal. With our companion B candidate reconstructed, the only remaining visible particles will belong to our signal kaon. Once this lone kaon (at most two tracks or one track and one π^0) is accounted for, there should be no tracks or showers unaccounted for in a signal event. By imposing tight restrictions on the

number of tracks and showers unused in the event reconstruction, we force the additional tracks and showers into the companion B candidate for background processes. This makes it much more difficult to reconstruct a companion B with reasonable invariant mass and energy. For companion B's in signal events, this is not the case.

In this chapter we will describe the methods used to reconstruct the companion B, the signal B, the restrictions placed on the unused tracks and showers and other whole event variables, and finally the variables used to extract the signal.

4.1 Event Requirements

The real power of this analysis is that when we have candidates for the companion B and signal B, we should have accounted for all products of the $\Upsilon(4S)$ decay. If we have correctly reconstructed a signal event, there should be no leftover tracks or showers. We deal with this in two different ways. For charged tracks, we can simply require that there be no unused charged tracks left in the event after accounting for the companion B and the signal B. The result is a drastic reduction in all types of background. The number of extra charged tracks is illustrated in Figure 4.1 for each of the signal modes. The selection of companion B and signal B candidates is described in the following sections, and the track and shower selection requirements are described in Appendix A. The requirement that there be no extra tracks was applied in all the subsequent figures in this chapter.

For the leftover shower energy, rather than use the number of showers, we

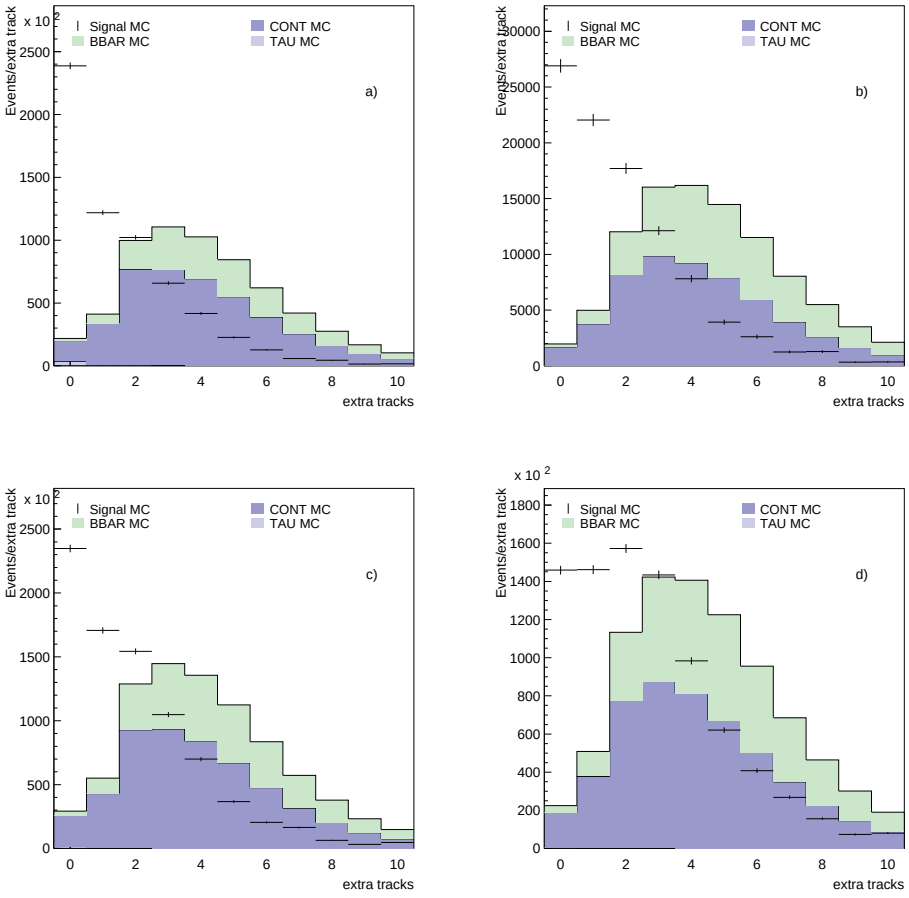

Figure 4.1: Event Requirements: Leftover Track Distributions.

The number of charged tracks left over after both the companion B and signal B have been reconstructed. The four plots are for the four signal modes K (a), K_S (b), K^* (c), and K^{*0} (d). The relative sizes of the background components are set by their cross sections, and the signal is then scaled to have equal area.

add up the energy in all showers not included in the reconstructed event. To be included in this sum, which we call E_{left}, the showers must pass the requirements described in Section A.3. Distributions of E_{left} are shown in Figure 4.2.

We also count the number of π^0 that were not used in the reconstruction but pass the loose π^0 cuts described in Section A.2. We do not require the number of π^0s to be zero, since there may be some signal efficiency to be gained by loosening that requirement. The distributions can be found in Figure 4.3.

The existence of signal with extra tracks, showers, and π^0s should not be misconstrued. Our signal Monte Carlo samples include companion B s which are not limited to $B \to D^{(*)}(n\pi)$. As a result, events in the signal Monte Carlo sample can be badly misreconstructed as $B \to D^{(*)}(n\pi)$and appear as background.

In addition to these "leftovers," we also make a cut on the overall event shape. This is done through the variable R_2 which is the ratio of the second and zeroth Fox-Wolfram moments [32]. R_2 is most useful for suppressing continuum and τ-pair backgrounds as can be seen in Figure 4.4.

4.2 D Reconstruction

In order to know what is left over, we must have candidates for our companion B and signal B. We begin our reconstruction of the decay of the companion B in the modes $B \to D^{(*)}(n\pi)$, with the selection of our D candidates. We reconstruct the D in the decay modes found in Table 4.1. The "dirty modes" have large background and were considered for removal during cut optimization as described

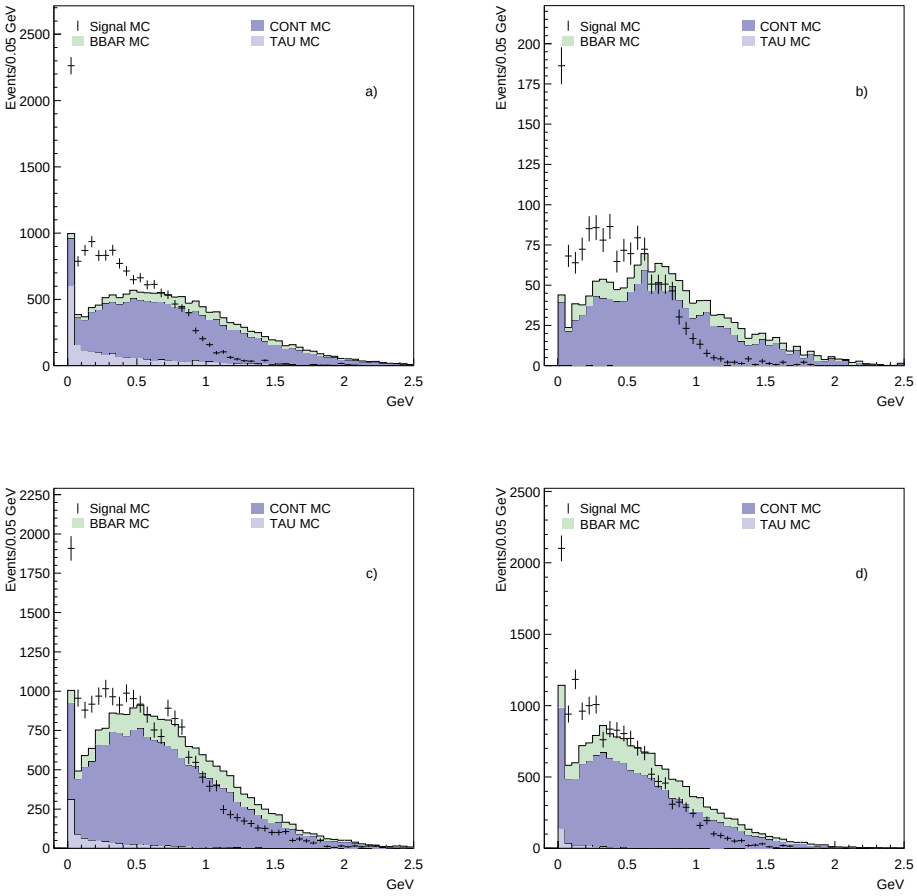

Figure 4.2: Event Requirements: E_{left}.

The amount of energy from showers unused in the reconstructions of the signal modes K (a), K_S (b) K^* (c), and K^{*0} (d). The relative sizes of the background components are set by their cross sections, and the signal is then scaled to have equal area.

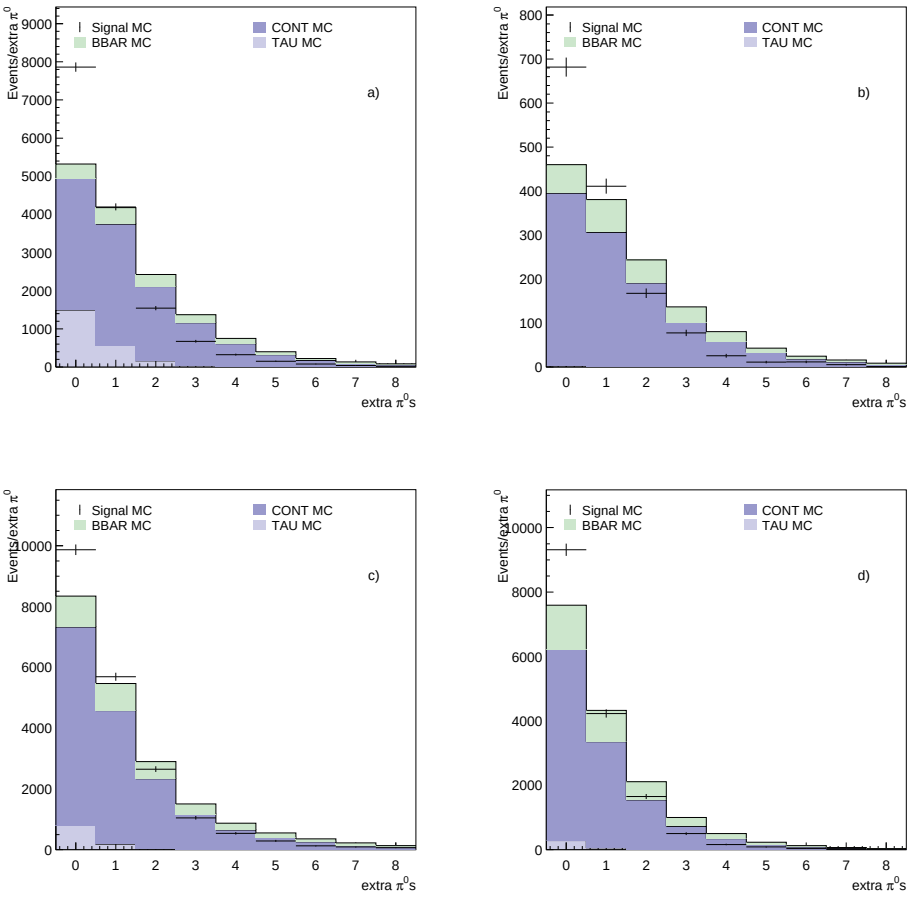

Figure 4.3: Event Requirements: Leftover π^0s.

Number of π^0s not used in the reconstructions of the signal modes K (a), K_S (b) K^* (c), and K^{*0} (d). The relative sizes of the background components are set by their cross sections, and the signal is then scaled to have equal area.

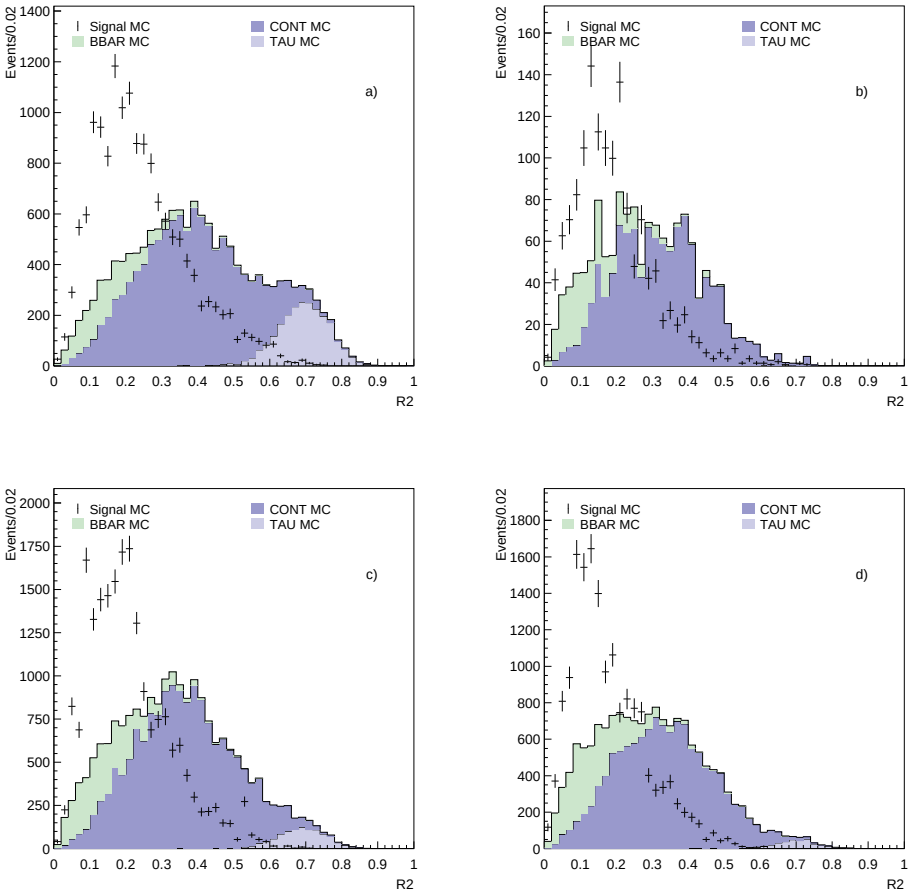

Figure 4.4: Event Requirements: R_2.

Distributions of R_2 for the signal modes K (a), K_S (b) K^* (c), and K^{*0} (d). The relative sizes of the background components are set by their cross sections, and the signal is then scaled to have equal area. The τ pair backgrounds can be seen in the charged signal modes with $R_2 > 0.5$ and are effectively separated in this variable.

Table 4.1: D Reconstruction Modes

$\overline{D}^0$ Mode	D^- Mode
$\overline{D}^0 \to K^+\pi^-$	$D^- \to K_S\pi^-$
$\overline{D}^0 \to K^+\pi^-\pi^0$	$D^- \to K^-\pi^+\pi^-$
$\overline{D}^0 \to K_S\pi^+\pi^-$	$D^- \to K_S\pi^-\pi^0$
$\overline{D}^0 \to K^+\pi^+\pi^-\pi^-$	$D^- \to K^-\pi^+\pi^-\pi^0$
$\overline{D}^0 \to K^+\pi^-\pi^0\pi^0$	$D^- \to K_S\pi^+\pi^-\pi^-$
$\overline{D}^0 \to K^+\pi^+\pi^-\pi^-\pi^0$	$D^- \to K^-\pi^+\pi^-\pi^0\pi^0$
$\overline{D}^0 \to K_S\pi^+\pi^-\pi^0$	$D^- \to K_S\pi^+\pi^-\pi^-\pi^0$
$\overline{D}^0 \to \pi^+\pi^-\pi^0$ ‡	$D^- \to \pi^+\pi^-\pi^-\pi^0$ ‡
$\overline{D}^0 \to K_S\pi^0$	
‡ Dirty Mode	

in Section 5.2. The cuts used to select K_S, π^0, and charged track candidates to use in the reconstruction are described in Appendix A. We define the nominal mass difference (χ_{M_D}) of the D candidate as the difference between the D candidate's reconstructed mass (M_{cand}) and the PDG[24] D mass (M_D) divided by the error on the reconstruction ($\sigma_{M_{cand}}$):

$$\chi_{M_D} = \frac{M_{cand} - M_D}{\sigma_{M_{cand}}} \tag{4.1}$$

We apply a 3σ consistency cut on this variable to keep the more horrendous reconstructions out of the mix. A plot of the χ_{M_D} can be seen in Figure 4.5. We

also require the momentum of the D candidate to be more than 1.0 GeV. This results in a cleaner D sample and reduces the size of the skims that are described in Appendix B.

We also calculate two variables to describe the quality of the identification of the D candidate's decay products. For charged track daughters, we define χ^2_{PID} to represent the quality of the particle identification.

$$\chi^2_{PID} = \sum_{\text{good dE/dx tracks}} \chi^2_{dE/dx} + \sum_{\text{good TOF tracks}} \chi^2_{TOF} \tag{4.2}$$

Here $\chi^2_{dE/dx}$ (χ^2_{TOF}) describe the particle identification information as described in Equation 3.7. For the neutral daughters, π^0 and K_S, we define $\chi^2_{vee\ fit}$ to characterize the quality of the fit.

$$\chi^2_{vee\ fit} = \sum_{\text{all } \pi^0\text{s in cand}} \chi^2_{\pi^0_{fit}} + \sum_{\text{all } \mathrm{K_S}\text{s in cand}} \chi^2_{K_{S_{fit}}} \tag{4.3}$$

The quality of the reconstruction of the π^0 and K_S are quantified by $\chi^2_{\pi^0_{fit}}$ and $\chi^2_{K_S\ fit}$ which are described in Section 3.2.2.

We combine $\chi^2_{M_D}$, χ^2_{PID}, and $\chi^2_{vee\ fit}$ to create a Figure Of Merit (FOM) representing the overall quality of the D candidate reconstruction.

$$\chi^2_{D_{FOM}} = \chi^2_{M_D} + \chi^2_{vee\ fit} + \chi^2_{PID} \tag{4.4}$$

We define our D_{FOM} as the probability of $\chi^2_{D_{FOM}}$ for the number of degrees of freedom used to calculate $\chi^2_{D_{FOM}}$ as described in Section 31.3.2 of Ref. [24]. A plot of D_{FOM} can be seen in Figure 4.5

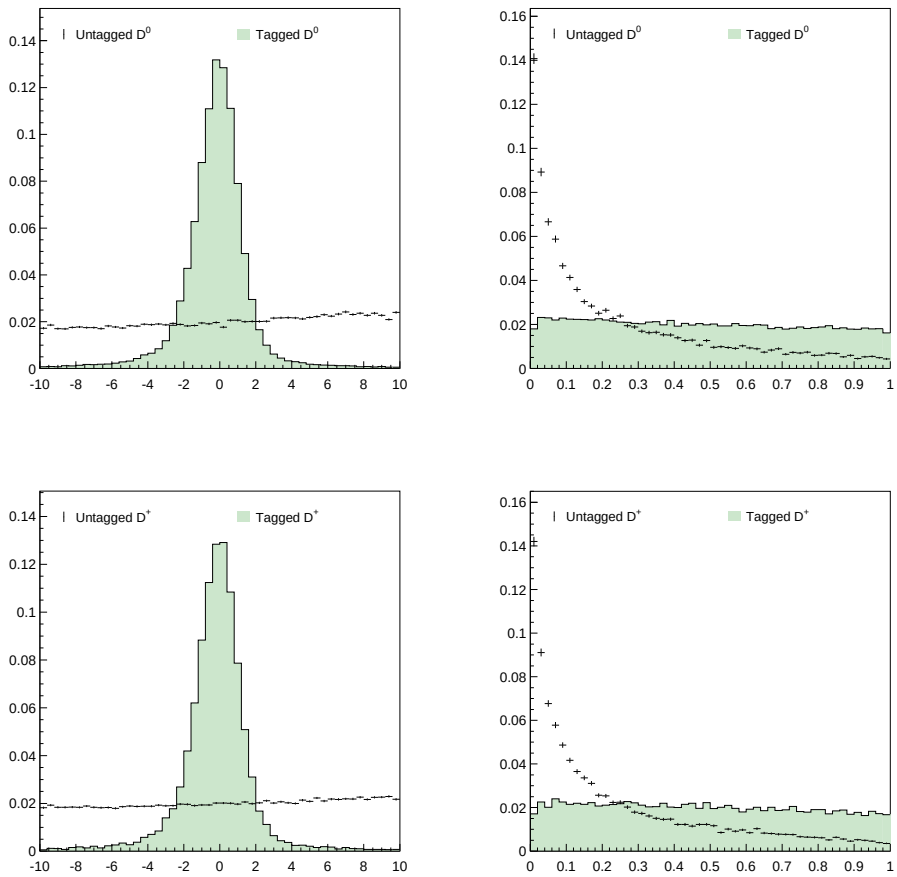

Figure 4.5: D Reconstruction: χ_{M_D} and FOM_D.

The left plots show χ_{M_D} and the right plots show the D_{FOM} from Monte Carlo simulation. The shaded histogram contains tagged D candidates, the points are untagged D candidates which are mainly composed of combinatoric backgrounds. The histograms have been scaled to have unit area.

Table 4.2: $D^* - D$ Mass Difference Cuts

D^* Decay Mode	Cut		
$\overline{D}^{*0} \to \overline{D}^0\pi^0$		$\lvert(M_{\overline{D}^{*0}} - M_{\overline{D}^0} - \Delta M_{PDG}\rvert$	< 0.0025 GeV
$\overline{D}^{*0} \to \overline{D}^0\gamma$	-0.020 GeV $<$	$(M_{\overline{D}^{*0}} - M_{\overline{D}^0} - \Delta M_{PDG})$	< 0.0150 GeV
$D^{*-} \to \overline{D}^0\pi^-$		$\lvert(M_{D^{*-}} - M_{\overline{D}^0} - \Delta M_{PDG}\rvert$	< 0.0025 GeV
$D^{*-} \to D^-\pi^0$		$\lvert(M_{D^{*-}} - M_{D^-} - \Delta M_{PDG}\rvert$	< 0.020 GeV
$D^{*-} \to D^-\gamma$	-0.020 GeV $<$	$(M_{D^{*-}} - M_{D^-} - \Delta M_{PDG})$	< 0.0150 GeV

4.3 D^* Reconstruction

We also reconstruct D^* mesons in the decay modes $D^* \to D\pi$ and $D^* \to D\gamma$. The only cut that we made is that the mass difference between reconstructed D^* and its daughter D be close to the nominal splitting quoted in the PDG [24]. These cuts are listed in table Table 4.2. Plots of these mass differences can be found in Figure 4.6.

4.4 Companion B Reconstruction

The dearth of information present on the signal B side of the event results in the companion B yielding the information that will ultimately define whether a given event is signal or background. We attempt to reconstruct the hadronic decays $B \to D^{(*)}(n\pi)$ listed in Table 4.3. Again, the large background modes are marked

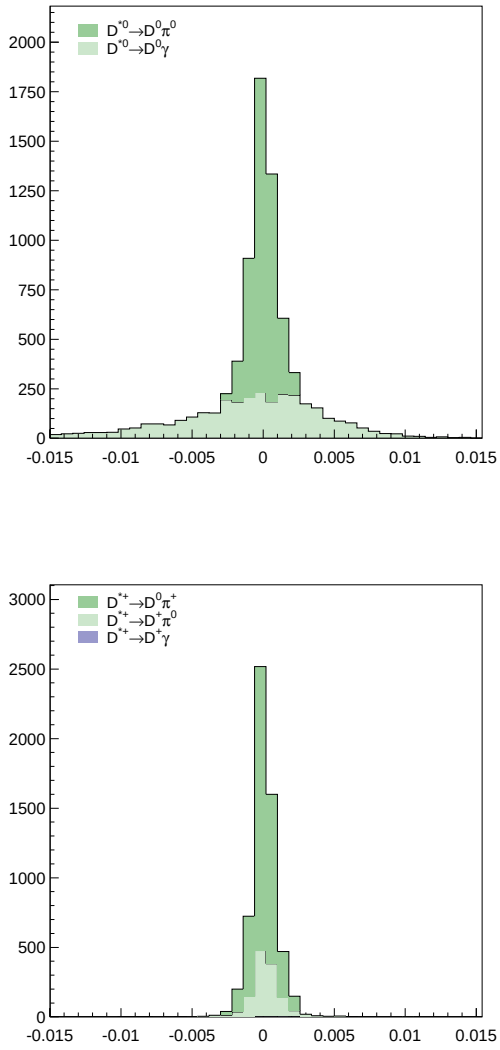

Figure 4.6: D^* Reconstruction: $D^* - D$ Mass Differences.

The $D^* - D$ Mass Difference from Monte Carlo simulation. The upper histograms contain tagged D^{*0} candidates and the lower histograms contain tagged D^+ candidates.

Table 4.3: Companion B Reconstruction Modes

B^+ Mode	B^0 Mode
$B^+ \to \overline{D}^{(*)0}\pi^+$	$B^0 \to D^{(*)-}\pi^+$
$B^+ \to \overline{D}^{(*)0}\pi^+\pi^0$	$B^0 \to D^{(*)-}\pi^+\pi^0$
$B^+ \to \overline{D}^{(*)0}\pi^+\pi^+\pi^-$ ‡	$B^0 \to D^{(*)-}\pi^+\pi^+\pi^-$ ‡
$B^+ \to \overline{D}^{(*)0}\pi^+\pi^0\pi^0$	$B^0 \to D^{(*)-}\pi^+\pi^0\pi^0$
$B^+ \to \overline{D}^{(*)0}\pi^+\pi^+\pi^-\pi^0$ ‡	$B^0 \to D^{(*)-}\pi^+\pi^+\pi^-\pi^0$ ‡
$B^+ \to \overline{D}^{(*)0}\pi^+\pi^+\pi^+\pi^-\pi^-$	$B^0 \to D^{(*)-}\pi^+\pi^+\pi^+\pi^-\pi^-$
‡ Dirty Mode	

as "dirty" and were considered for removal as a part of the cut optimization process described in Section 5.2. The quantities that we define to describe the companion B reconstruction can either be used in the suppression of background or the extraction of yield. (Or a little of both in the case of a fit.) In the end, we chose to cut on some of these quantities to suppress background; while others were used to extract our signal yield and predict the level of background present. How we extract the signal yield from this information is described in Chapter 5.

4.4.1 $(n\pi)$ Invariant Mass

In the hadronic decay of the companion B, $B \to D^{(*)}(n\pi)$, we define q^2 to be the invariant mass of the $(n\pi)$ system. In a correctly reconstructed companion B,

q^2 tends to be small, with structure associated with the light unflavored meson resonances. In misreconstructed candidates, where either too many or incorrect tracks are included in the companion B, the random combinations do not exhibit this structure and tend to larger values of q^2. This can be seen in Figure 4.7. As such, this variable allows us to suppress combinatoric backgrounds, which are particularly prevalent in $B\bar{B}$ backgrounds.

4.4.2 Thrust Axis

To reduce the amount of $q\bar{q}$ (continuum) background, we take advantage of the fact that the direction of tracks in continuum events are correlated. This is not the case in $B\bar{B}$ events (signal and background) since the B momenta are small in the lab frame. As a result B decays tend to be more isotropic than continuum events. We define the the angle between the signal B kaon and the thrust axis of the companion B to be θ_{thrust}. The distributions of $|\cos\theta_{thrust}|$ can be seen in Figure 4.8.

4.4.3 Beam Constrained Parameters

We construct two quantities using the precisely known energy of the electron-positron beams: the beam constrained mass M_B, and the beam energy difference ΔE.

$$M_B = \sqrt{E_{beam}^2 - |\vec{p}_B|^2} \tag{4.5}$$

$$\Delta E = E_B - E_{beam} \tag{4.6}$$

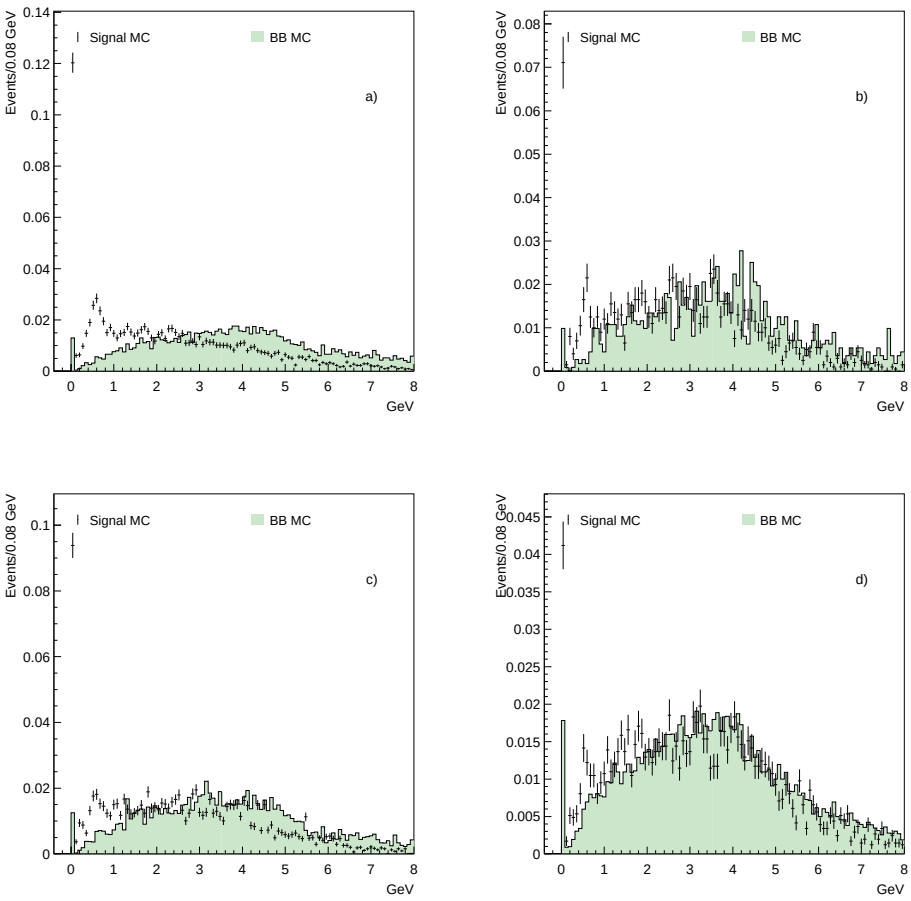

Figure 4.7: Companion B Reconstruction: q^2.

The $(n\pi)$ invariant mass (q^2) for the signal modes K (a), K_S (b), K^* (c), and K^{*0} (d). All histograms are scaled to unit area. Note the peak for the signal π peak at m_π. Also visible is the ρ peak. The hump at large q^2 is the result of combinatoric background, and as the signal mode multiplicity increases, so does the size of this hump.

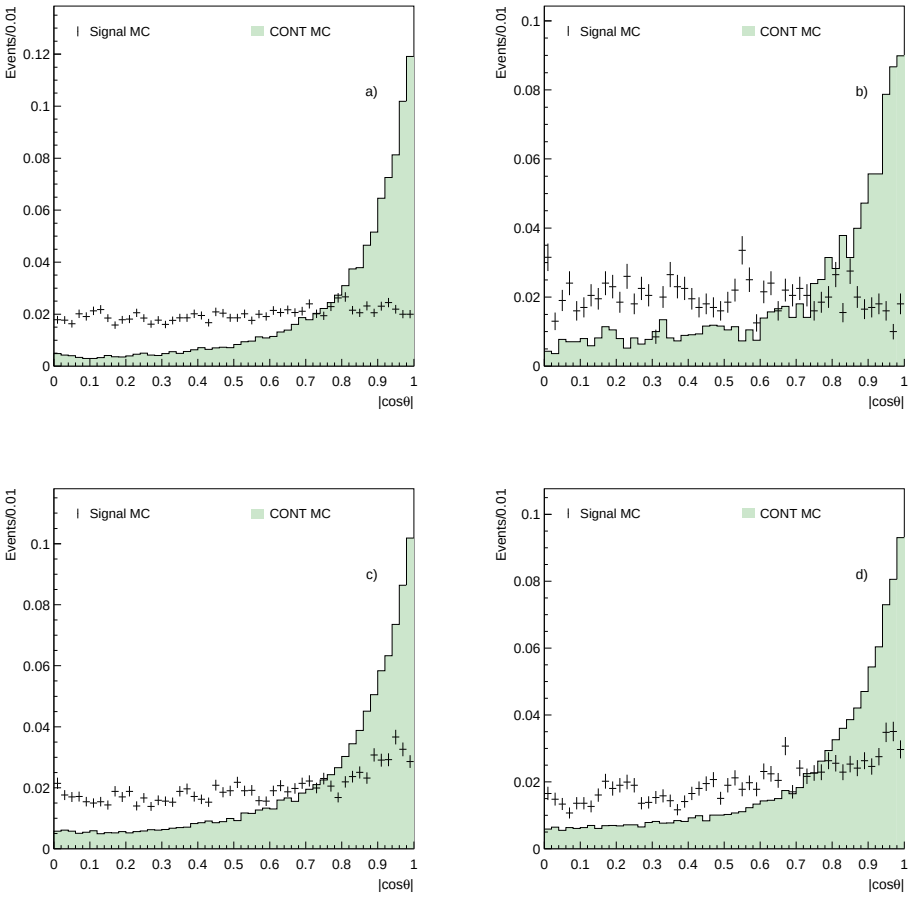

Figure 4.8: Companion B Reconstruction: $|\cos\theta_{thrust}|$.

The distributions $|\cos\theta_{thrust}|$ for the signal modes K (a), K_S (b), K^* (c), and K^{*0} (d). All histograms are scaled to unit area.

Here, E_B and $|\vec{p}_B|$ are the reconstructed energy and momentum of the candidate companion B. We can see in the plot of M_B in Figure 4.9 that signal Monte Carlo shows a peak at the B mass of 5.28 GeV.

Some important features of the ΔE spectrum are visible in Figure 4.10. First is the signal peak at $\Delta E = 0$ GeV. This is the ΔE value we expect when the event is correctly reconstructed. But, there is another peak at $\Delta E \sim -0.2$ GeV. This is due to signal events in which the reconstruction has misidentified $B \to D^*(n\pi)$ as $B \to D(n\pi)$ by losing the slow pion from the D^* decay. This satellite peak contains real signal, and as such we consider including these candidates in out cut optimization process described in Section 5.2.

We constrain ourselves to event candidates where there are no good tracks left unused in the reconstruction. In a signal event the maximum value ΔE can attain is limited by the energy taken away by the two neutrinos. For background, however, the only way to satisfy this requirement is to force extra tracks into the candidate companion B. This allows the ΔE spectrum to attain large positive values. We will use this in the cases where there are more than one candidate reconstruction. By selecting the candidates with the largest signed value for ΔE, we are assured that we will not push signal out of the signal peak, and additionally we know we will not be concentrating background around $\Delta E = 0$ GeV as we would by naïvely selecting the "best" candidate.

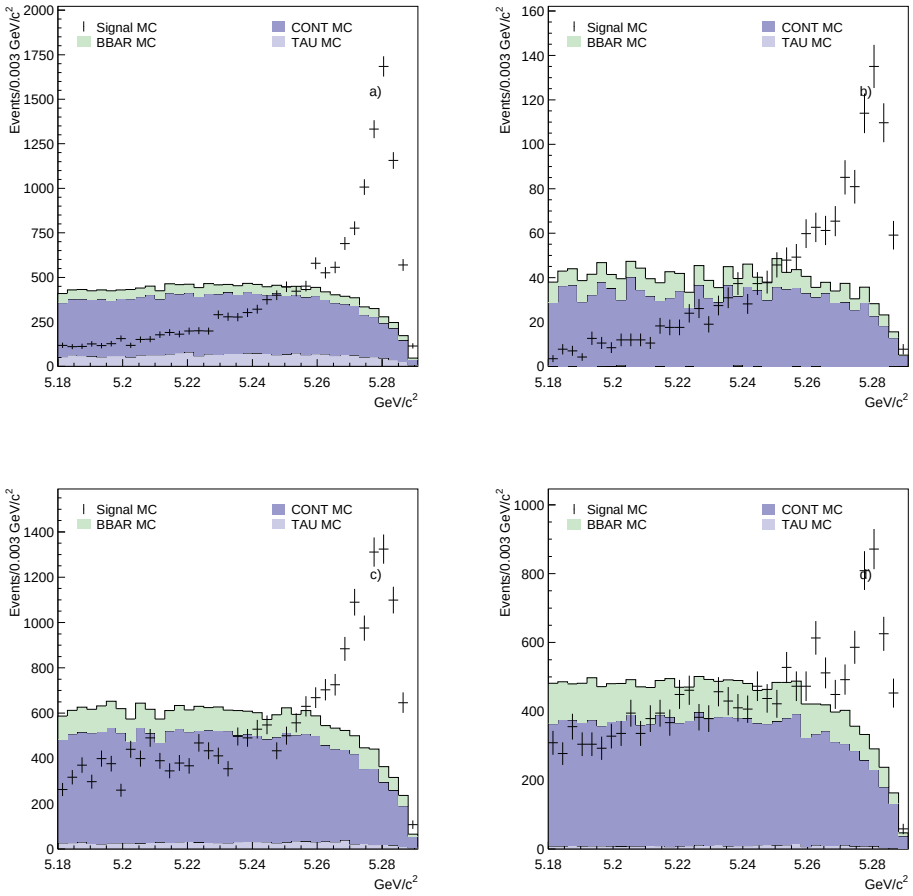

Figure 4.9: Companion B Reconstruction: M_B.

The distributions of M_B for the signal modes K (a), K_S (b), K^* (c), and K^{*0} (d). The signal Monte Carlo has been scaled to have area equal to the background histograms.

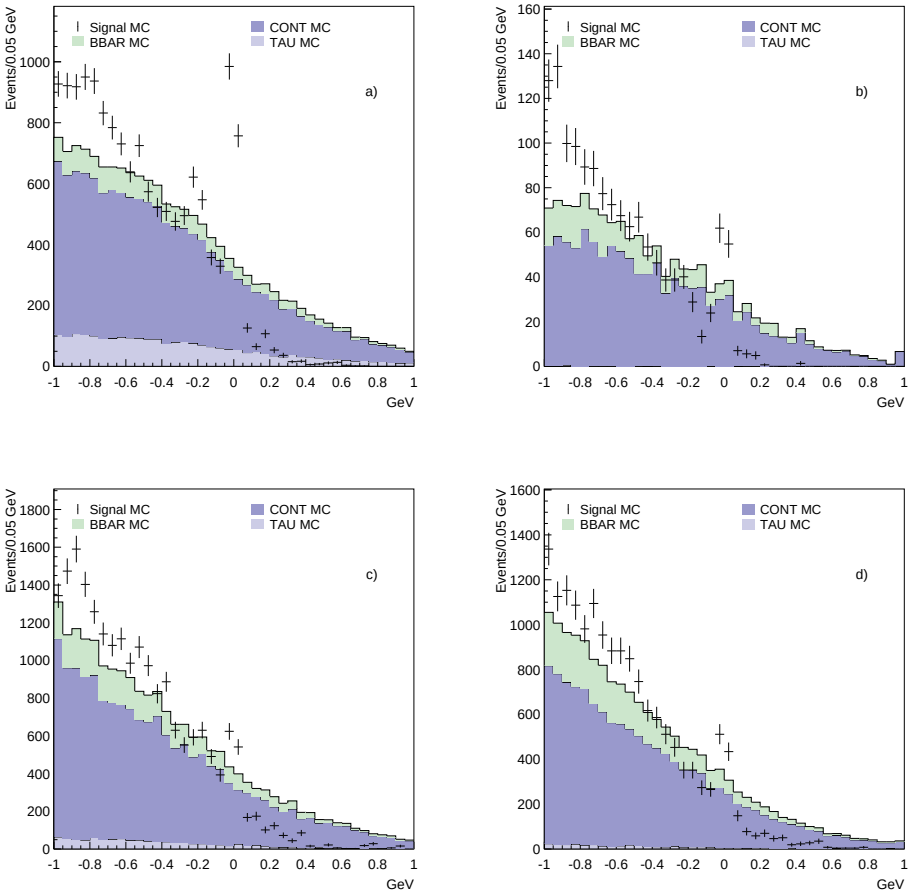

Figure 4.10: Companion B Reconstruction: ΔE.

The distributions of ΔE for the signal modes K (a), K_S (b), K^* (c), and K^{*0} (d). The signal Monte Carlo has been scaled to have area equal to the background histograms.

Table 4.4: $B \to K\nu\bar{\nu}$ Reconstruction Modes

Signal B Mode
$B^- \to K^-\nu\bar{\nu}$
$B^- \to K^{*-}\nu\bar{\nu}$
$\overline{B}^0 \to K_S\nu\bar{\nu}$
$\overline{B}^0 \to \overline{K}^{*0}\nu\bar{\nu}$

4.5 Signal B Reconstruction

The reconstruction of the signal B modes (listed in Table 4.4) is left intentionally loose. As the signal B's only visible decay product is a kaon, there is little to discriminate between signal and background. (Kaons can be found in most events at the $\Upsilon(4S)$.) Apart from trying to ensure that the kaon is really a kaon by the usual tools of particle ID and kinematic fitting (for the K_S and K^* modes,) the only kinematic variable for us to use is the momentum of the signal kaon. The direction of the kaon is already used in the variable $\cos\theta_{thrust}$. The magnitude of the momentum could be a useful quantity (models favor high kaon momenta for the scalar kaon modes [9]), but we avoid it since to cut on it would require good knowledge of the kaon spectrum, thereby introducing model dependency.

4.6 Data-Monte Carlo Agreement

We proceed to apply our reconstruction method to our various data samples which are summarized in Appendix C. Roughly speaking, they can be broken down into three samples, Signal Monte Carlo, Background Monte Carlo, and CLEO Data. Since we use the Monte Carlo samples to optimize our cut values, we need to have some confidence that these samples model the data accurately. However, we need to do so in a way that doesn't bias our analysis. That is to say, we need to look in the sidebands. This is natural enough when we think of our signal box variables of M_B and ΔE, but in addition, we are able to utilize a less obvious sideband. We look at events in which there is exactly one track leftover after the reconstruction. This benefits us in two ways, we were able to look at the full ranges of M_B and ΔE, and the one extra track sample has higher statistics than the normal ΔE sideband. We also compare Off Resonance Data to Monte Carlo. This can be thought of as a $\sqrt{s}$ sideband.

Figures 4.11-4.16 show the variables defined previously in the ΔE sideband, and Figures 4.17-4.22 show the same in the one extra track sideband. Figures 4.23-4.28 show the Off Resonance Data compared to Continuum and Tau Pair Monte Carlo. ($B\bar{B}$ production is not present in the Off Resonance Data.) In all of the figures, the relative sizes of the background Monte Carlo samples are fixed by their cross sections, then the overall background rate is scaled to have equal area as the Data.

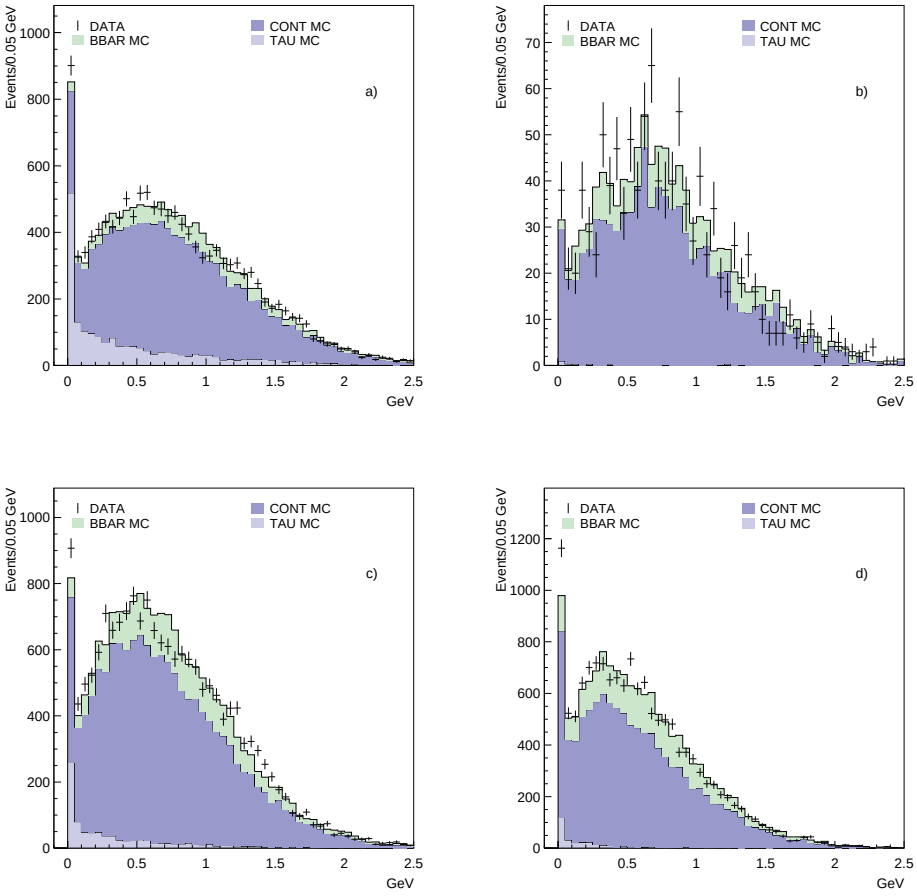

Figure 4.11: Data-MC Comparison, M_B-ΔE sideband: E_{left}.

The amount of energy from showers unused in the reconstructions of the signal modes K (a), K_S (b) K^* (c), and K^{*0} (d) from the M_B-ΔE sideband. The relative background sizes are fixed by their cross sections, and the total background is then scaled to equal the Data area.

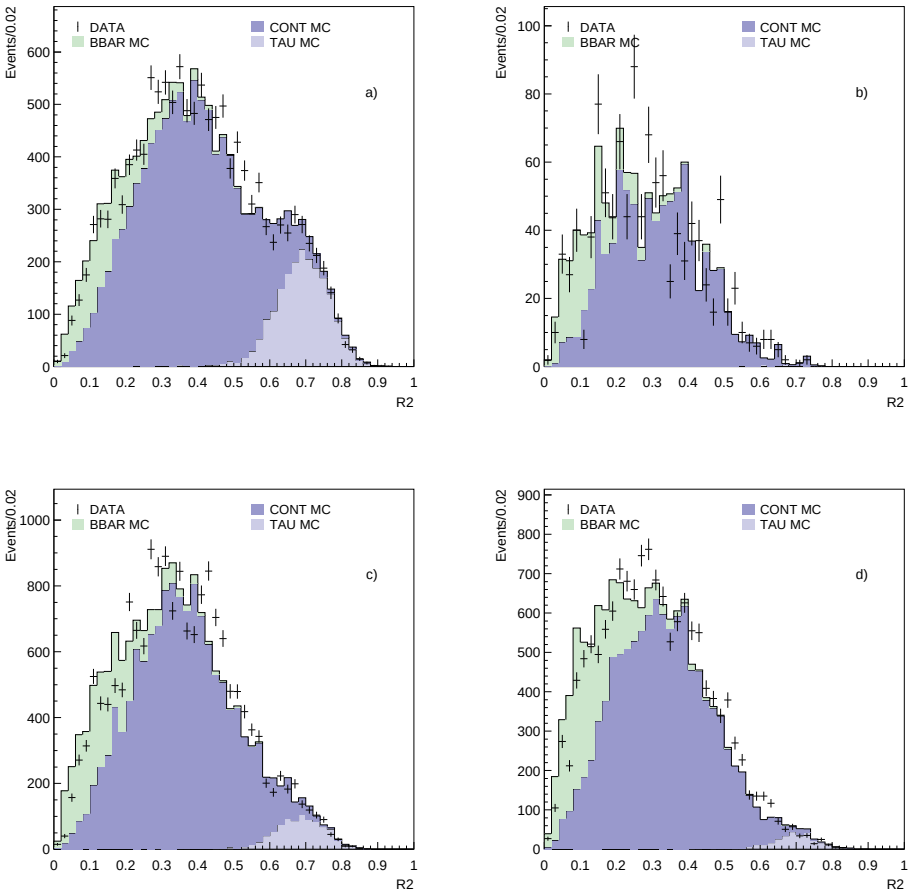

Figure 4.12: Data-MC Comparison, M_B-ΔE sideband: R_2.

Distributions of R_2 for the signal modes K (a), K_S (b) K^* (c), and K^{*0} (d) from the M_B-ΔE sideband. The relative background sizes are fixed by their cross sections, and the total background is then scaled to equal the Data area.

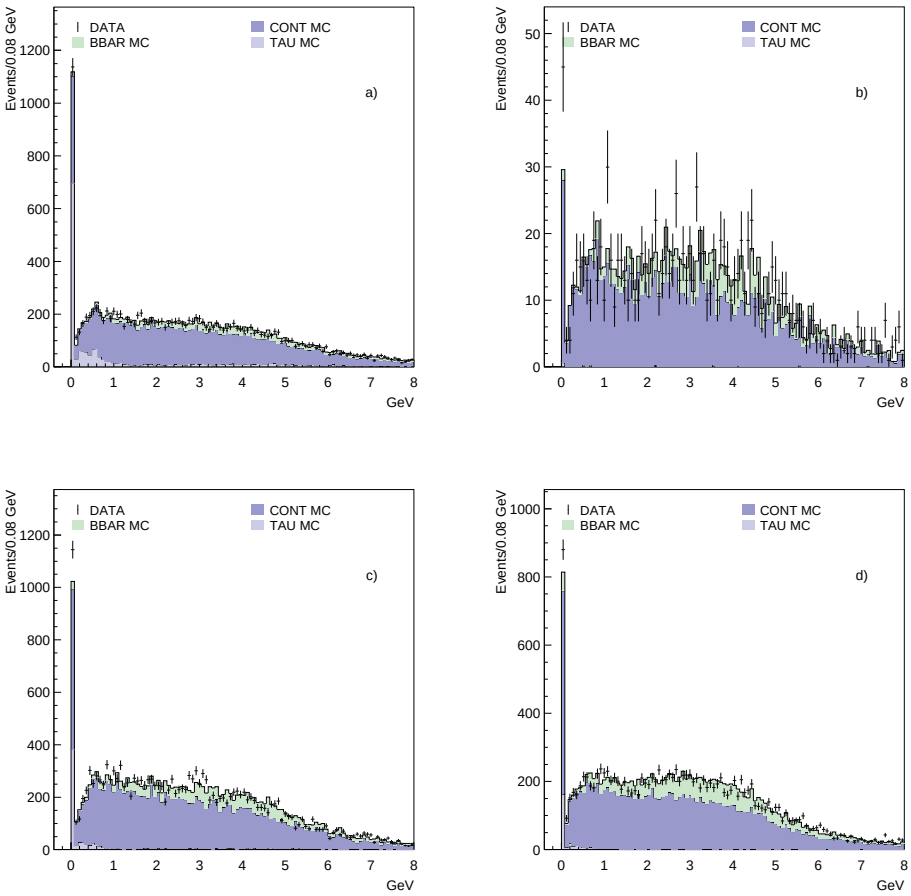

Figure 4.13: Data-MC Comparison, M_B-ΔE sideband: q^2.

The $(n\pi)$ invariant mass (q^2) for the signal modes K (a), K_S (b), K^* (c), and K^{*0} (d) from the M_B-ΔE sideband. The relative background sizes are fixed by their cross sections, and the total background is then scaled to equal the Data area.

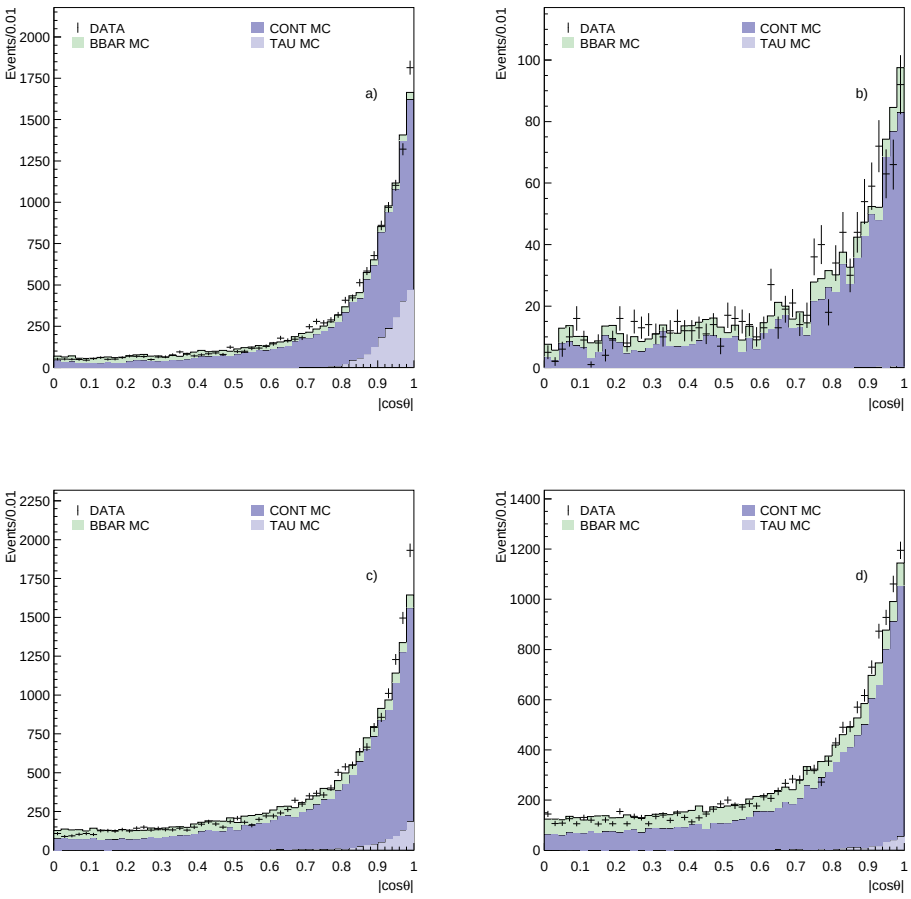

Figure 4.14: Data-MC Comparison, M_B-ΔE sideband: $|\cos\theta_{thrust}|$.
The distributions $|\cos\theta_{thrust}|$ for the signal modes K (a), K_S (b), K^* (c), and K^{*0} (d) from the M_B-ΔE sideband. The relative background sizes are fixed by their cross sections, and the total background is then scaled to equal the Data area.

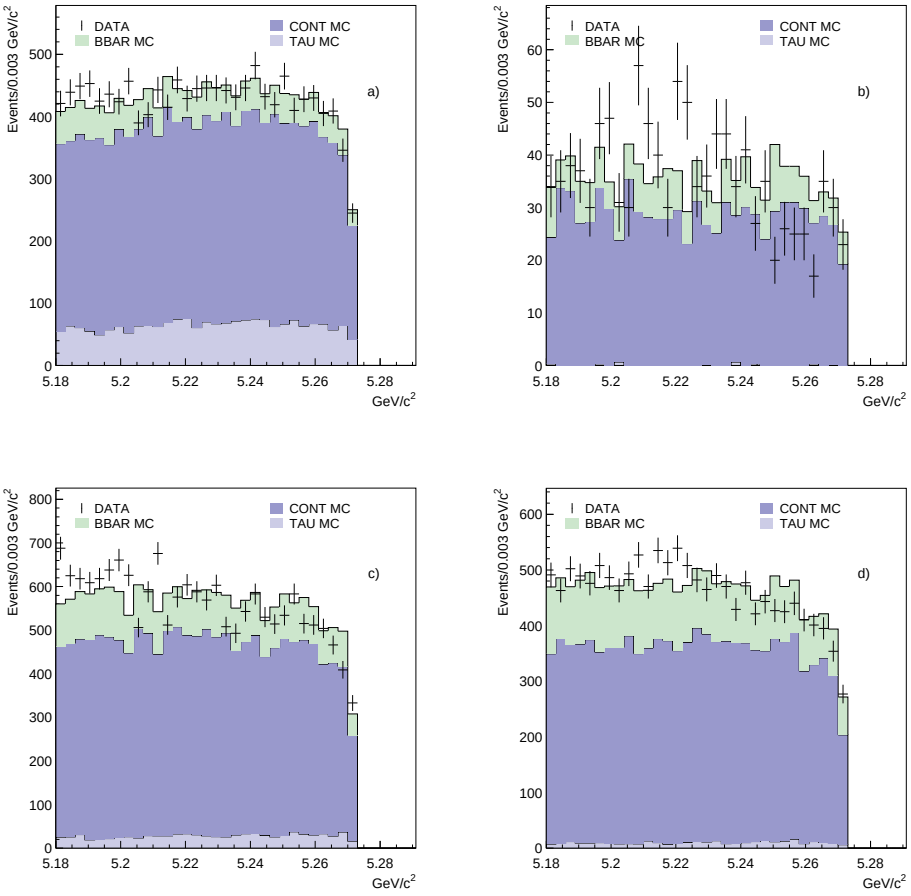

Figure 4.15: Data-MC Comparison, M_B-ΔE sideband: M_B.

The distributions of M_B for the signal modes K (a), K_S (b), K^* (c), and K^{*0} (d) from the M_B-ΔE sideband. The relative background sizes are fixed by their cross sections, and the total background is then scaled to equal the Data area. Note the exclusion of the signal region.

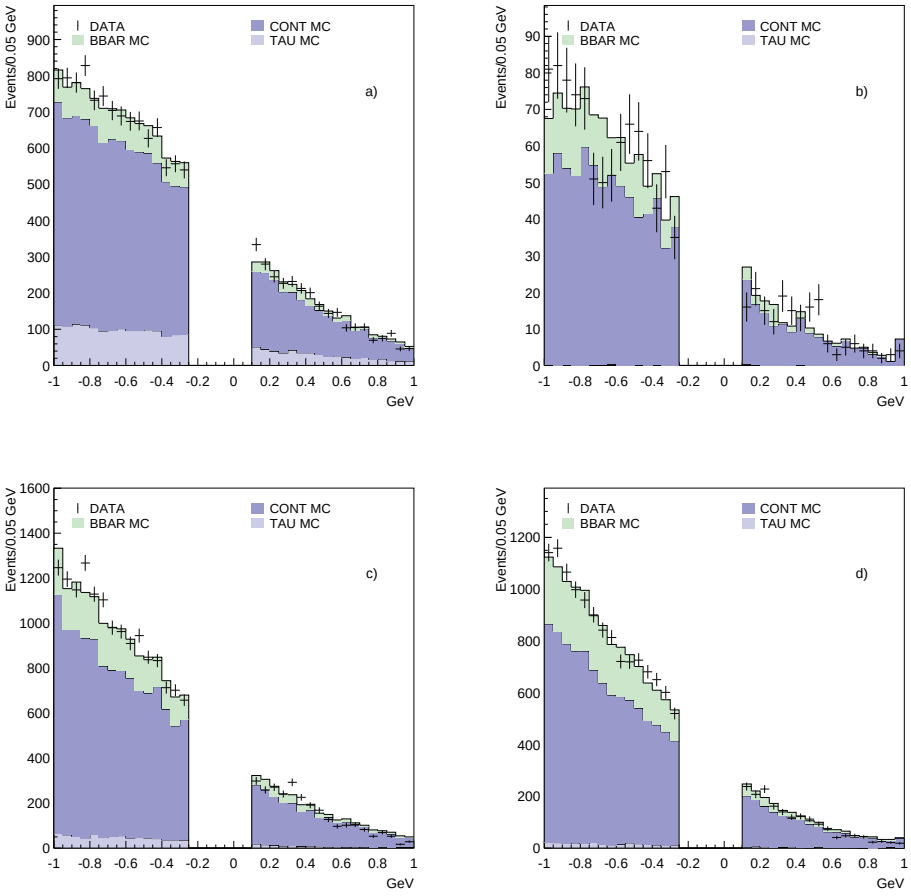

Figure 4.16: Data-MC Comparison, M_B-ΔE sideband: ΔE.

The distributions of ΔE for the signal modes K (a), K_S (b), K^* (c), and K^{*0} (d) from the M_B-ΔE sideband. The relative background sizes are fixed by their cross sections, and the total background is then scaled to equal the Data area. Note the exclusion of the signal region.

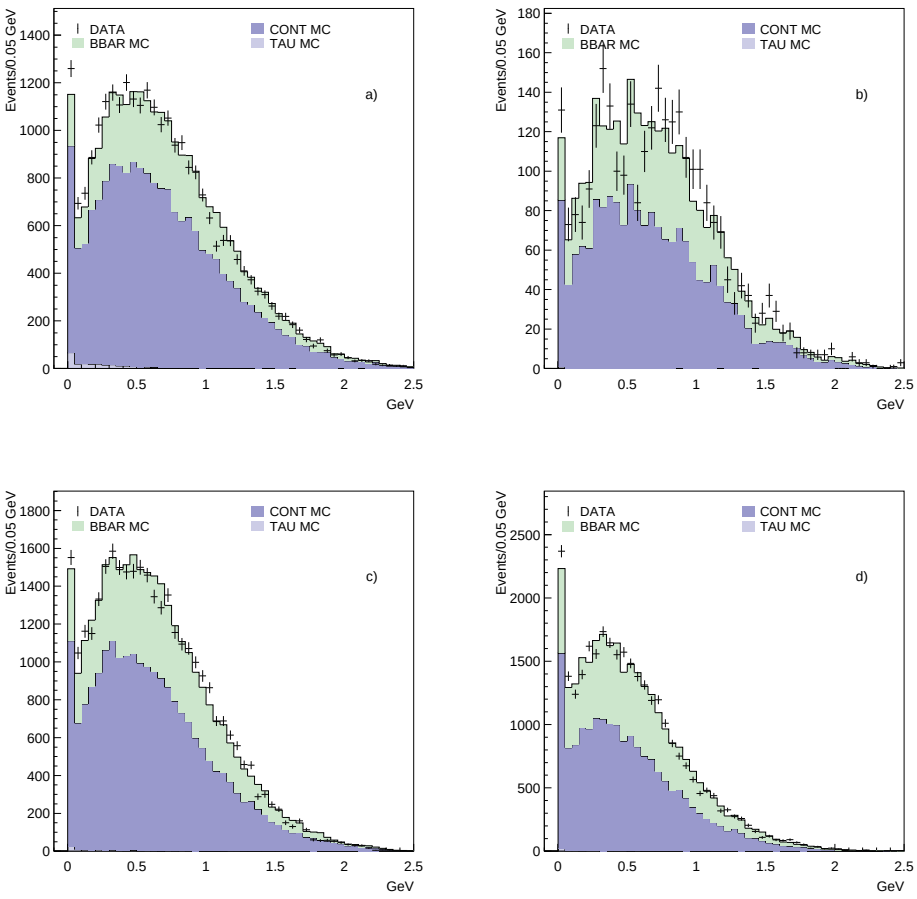

Figure 4.17: Data-MC Comparison, One extra track sideband: E_{left}. The amount of energy from showers unused in the reconstructions of the signal modes K (a), K_S (b) K^* (c), and K^{*0} (d) from the one extra track sideband. The relative background sizes are fixed by their cross sections, and the total background is then scaled to equal the Data area.

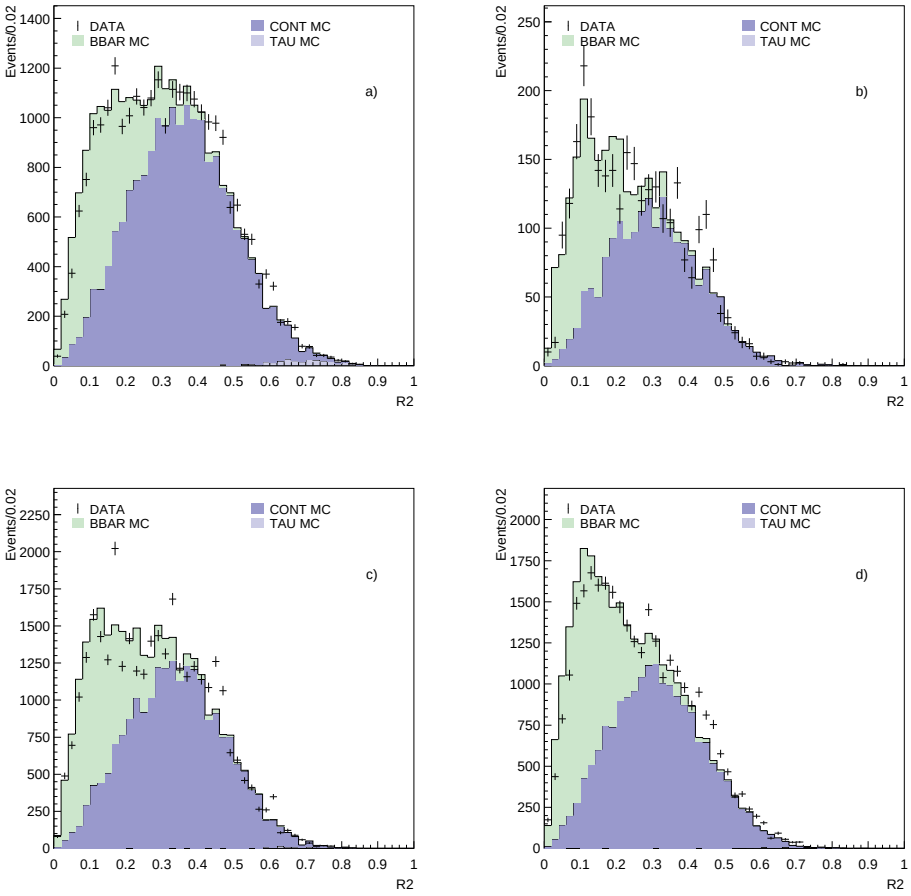

Figure 4.18: Data-MC Comparison, One extra track sideband: R_2.

Distributions of R_2 for the signal modes K (a), K_S (b) K^* (c), and K^{*0} (d) from the one extra track sideband. The relative background sizes are fixed by their cross sections, and the total background is then scaled to equal the Data area. It is clear from these plots, that there is very little τ pair background in this sideband.

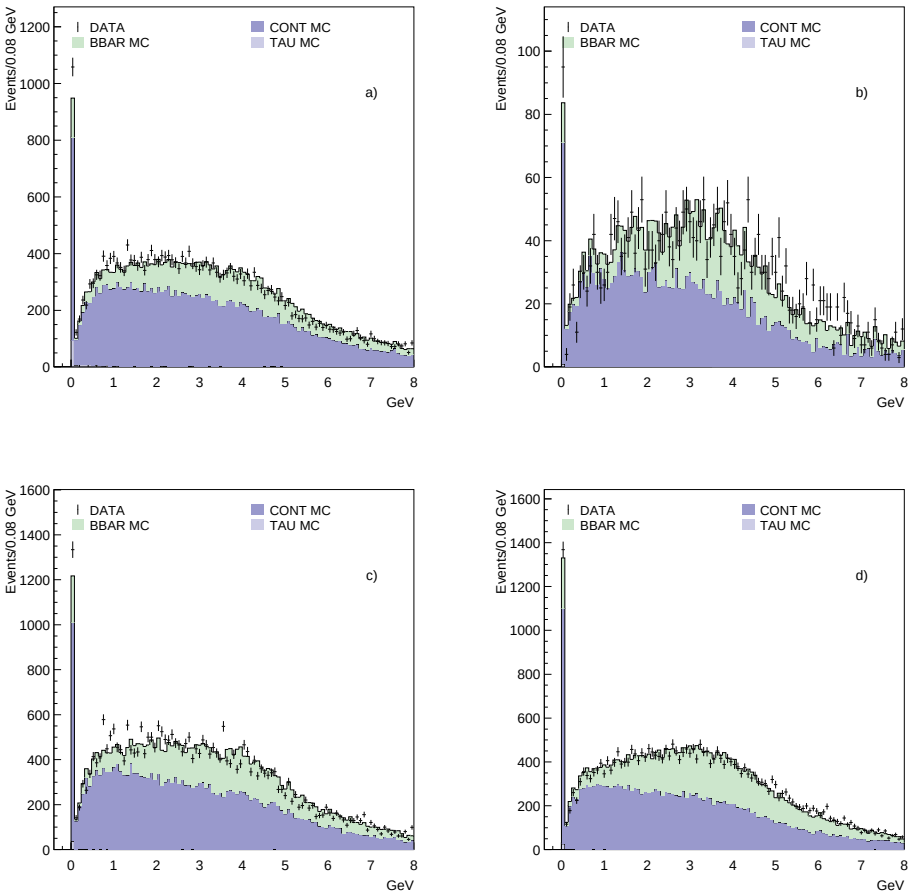

Figure 4.19: Data-MC Comparison, One extra track sideband: q^2.

The $(n\pi)$ invariant mass (q^2) for the signal modes K (a), K_S (b), K^* (c), and K^{*0} (d) from the one extra track sideband. The relative background sizes are fixed by their cross sections, and the total background is then scaled to equal the Data area.

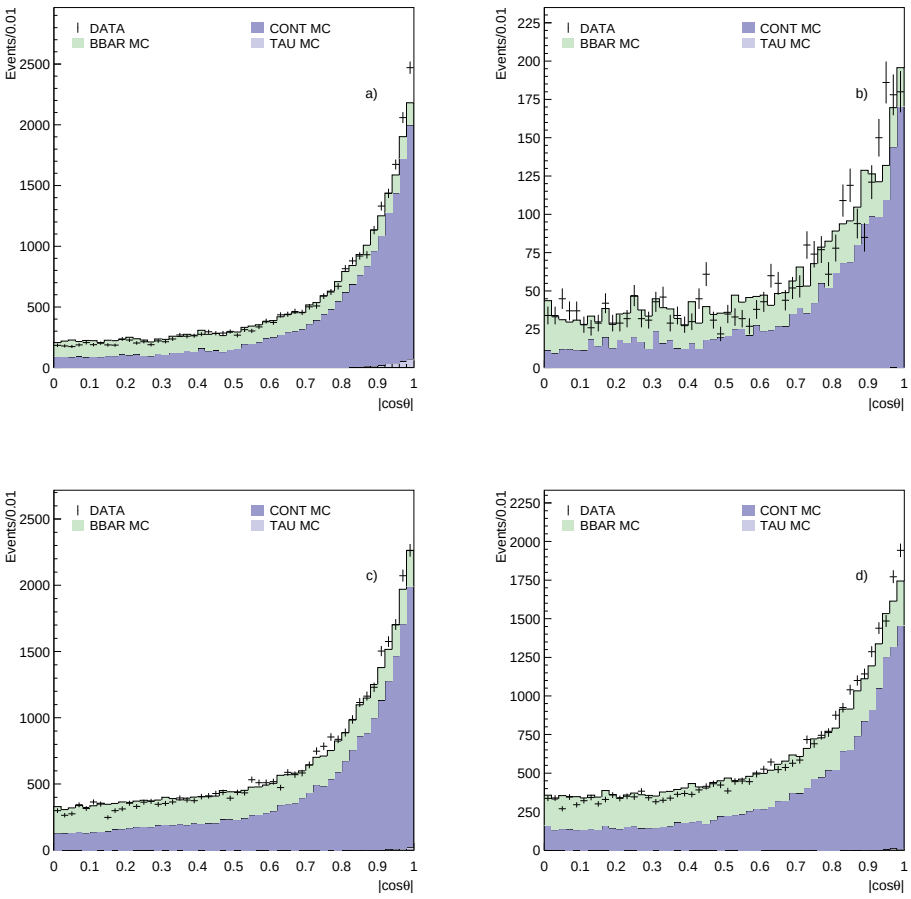

Figure 4.20: Data-MC Comparison, One extra track sideband: $|\cos\theta_{thrust}|$. The distributions $|\cos\theta_{thrust}|$ for the signal modes K (a), K_S (b), K^* (c), and K^{*0} (d) from the one extra track sideband. The relative background sizes are fixed by their cross sections, and the total background is then scaled to equal the Data area.

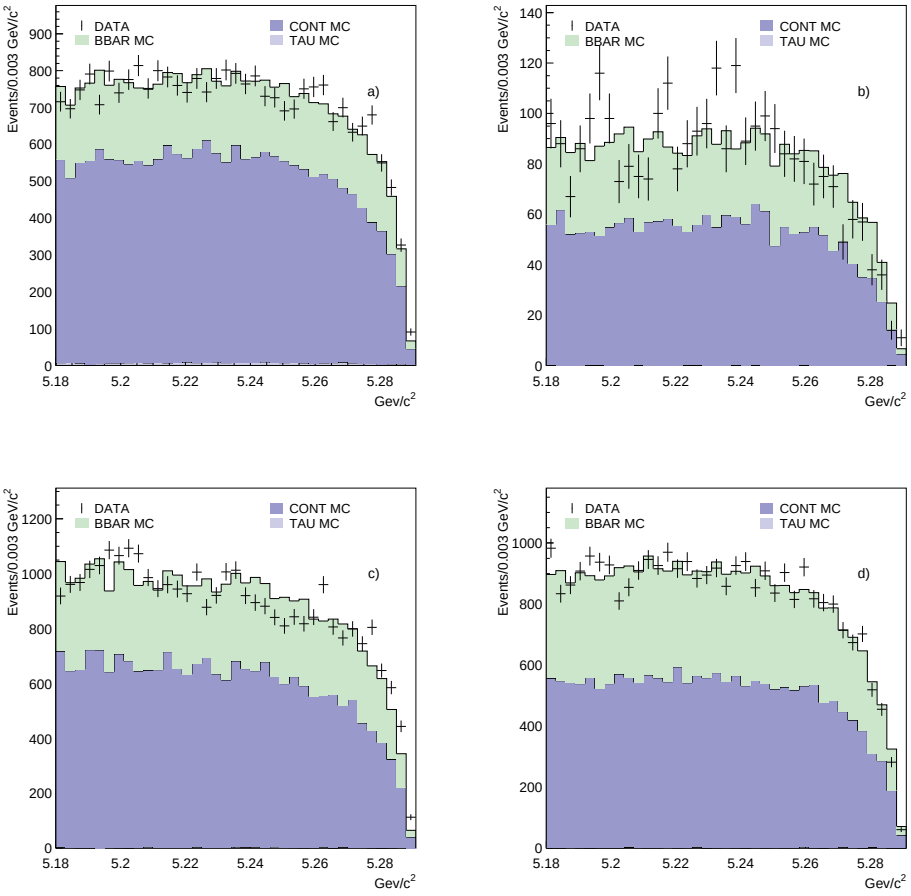

Figure 4.21: Data-MC Comparison, One extra track sideband: M_B.

The distributions of M_B for the signal modes K (a), K_S (b), K^* (c), and K^{*0} (d) from the one extra track sideband. The relative background sizes are fixed by their cross sections, and the total background is then scaled to equal the Data area.

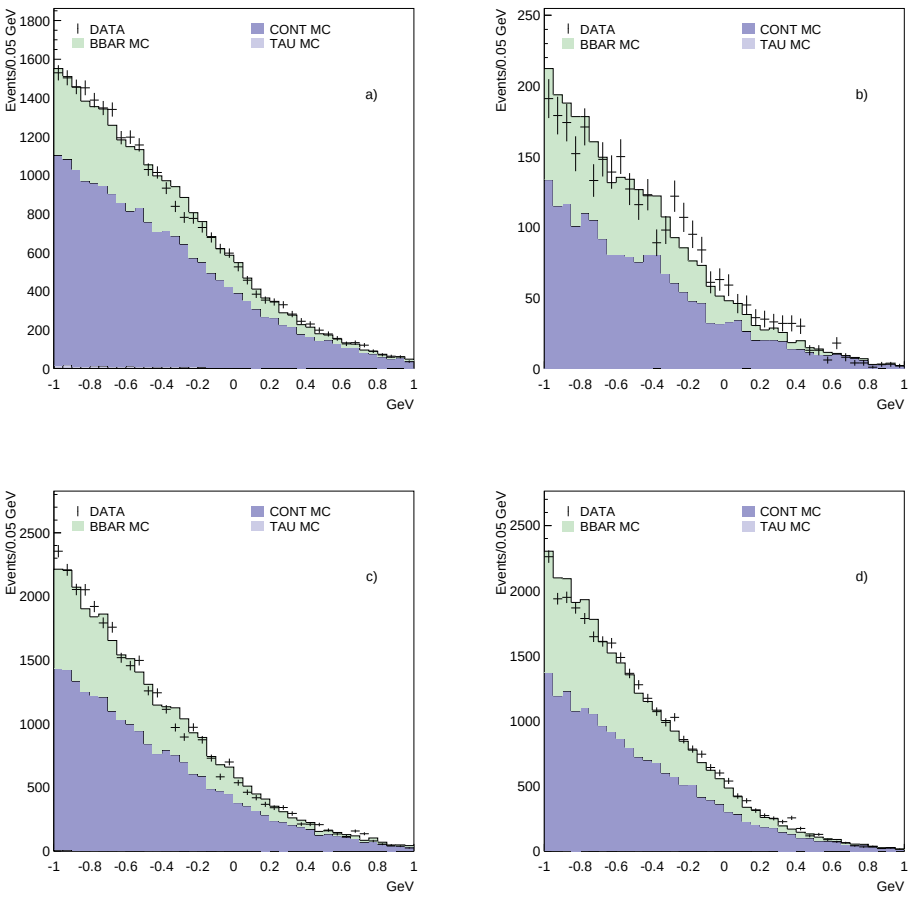

Figure 4.22: Data-MC Comparison, One extra track sideband: ΔE.

The distributions of ΔE for the signal modes K (a), K_S (b), K^* (c), and K^{*0} (d) from the one extra track sideband. The relative background sizes are fixed by their cross sections, and the total background is then scaled to equal the Data area.

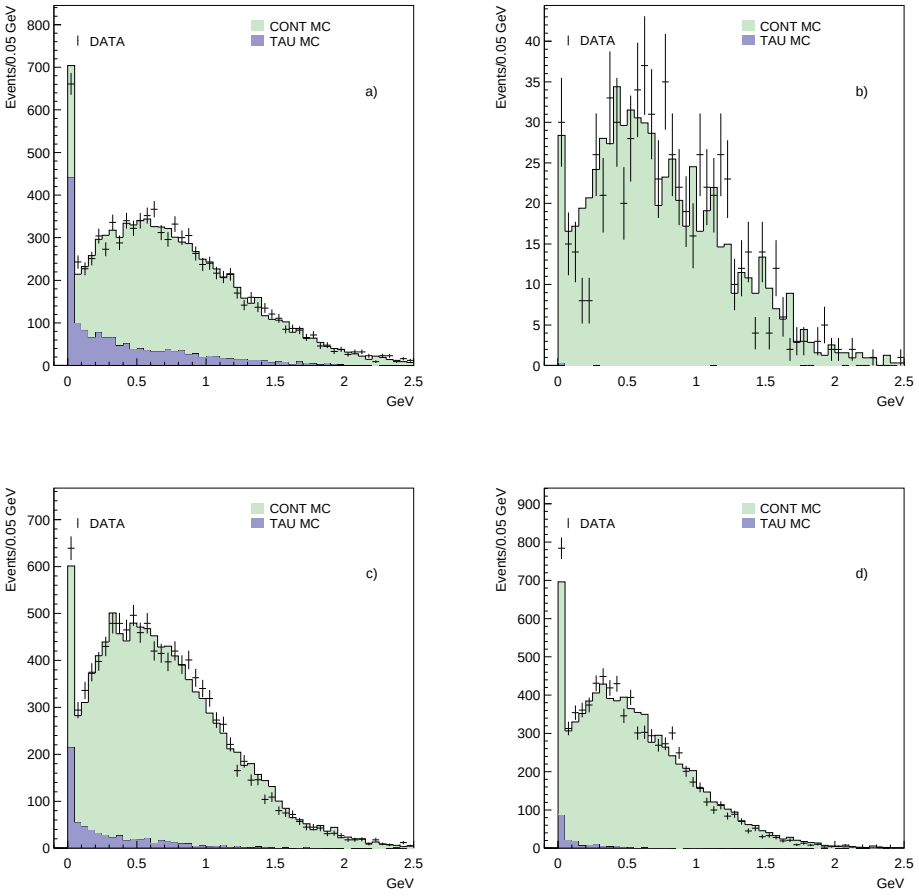

Figure 4.23: Data-MC Comparison, Off Resonance Data: E_{left}.

The amount of energy from showers unused in the reconstructions of the signal modes K (a), K_S (b) K^* (c), and K^{*0} (d) from the off resonance data. The relative background sizes are fixed by their cross sections, and the total background is then scaled to equal the Data area.

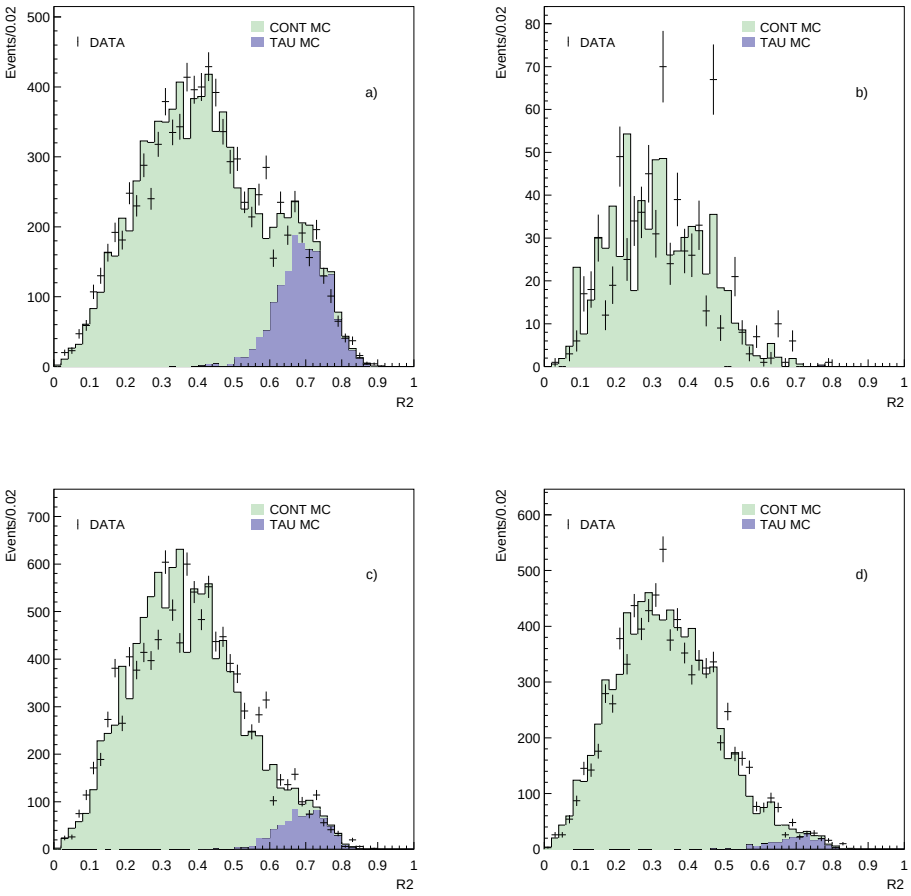

Figure 4.24: Data-MC Comparison, Off Resonance Data: R_2.

Distributions of R_2 for the signal modes K (a), K_S (b) K^* (c), and K^{*0} (d) from the off resonance data. The relative background sizes are fixed by their cross sections, and the total background is then scaled to equal the Data area.

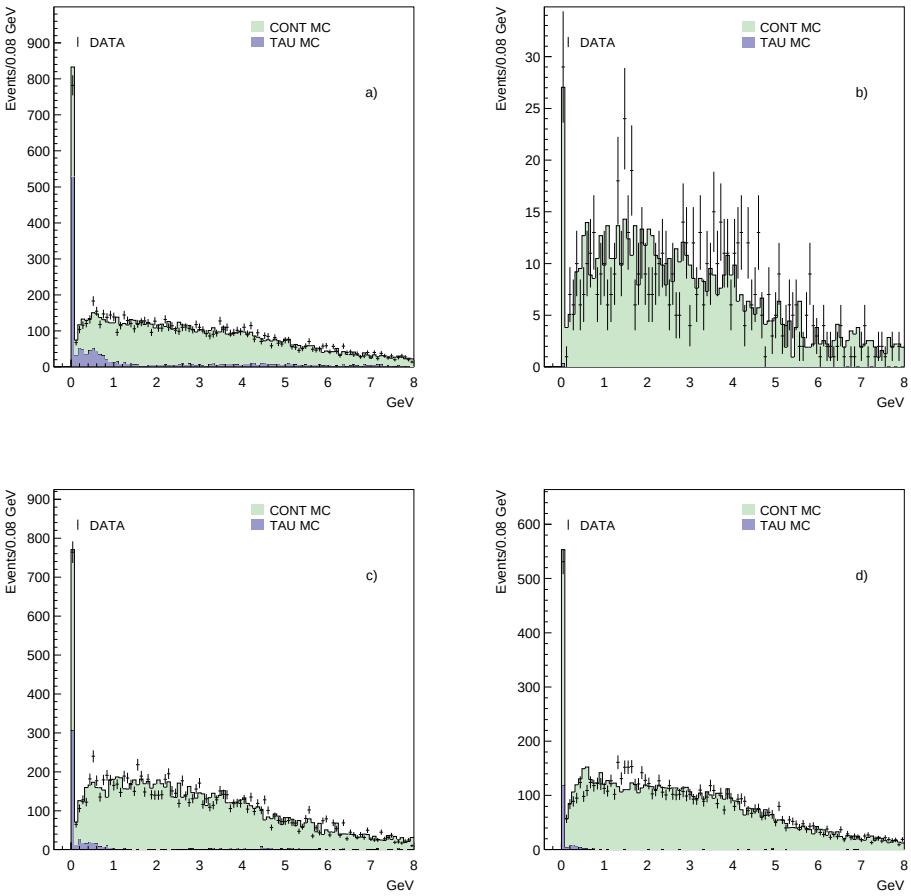

Figure 4.25: Data-MC Comparison, Off Resonance Data: q^2.

The $(n\pi)$ invariant mass (q^2) for the signal modes K (a), K_S (b), K^* (c), and K^{*0} (d) from the off resonance data. The relative background sizes are fixed by their cross sections, and the total background is then scaled to equal the Data area.

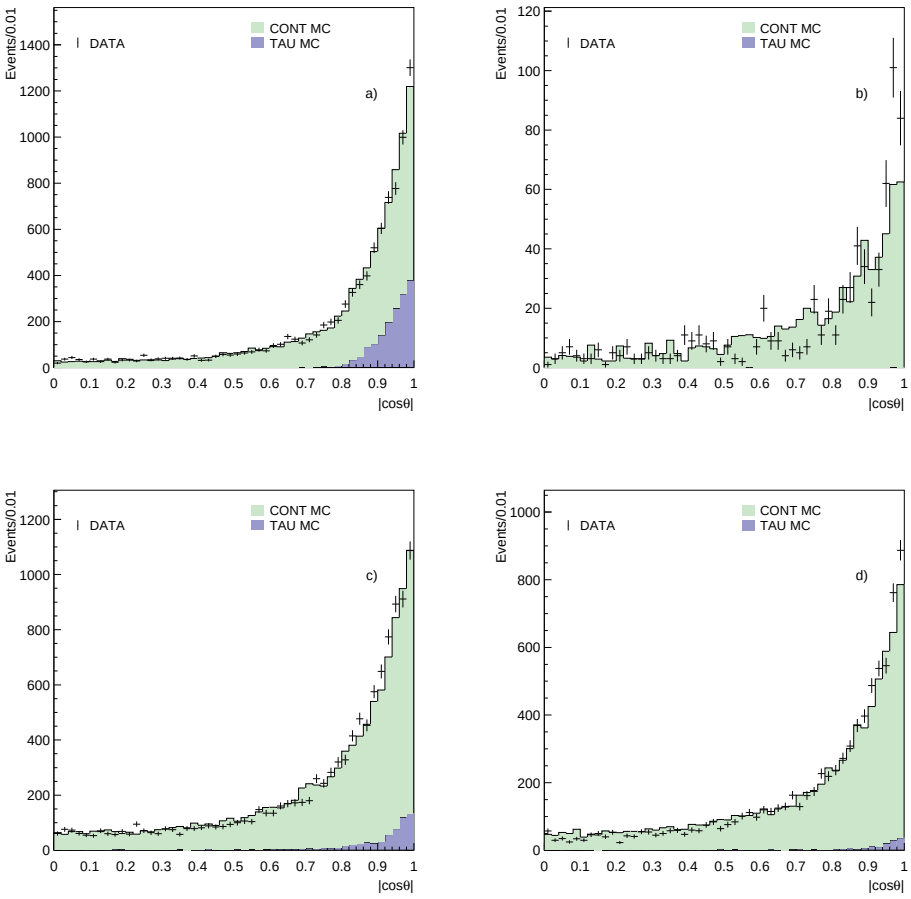

Figure 4.26: Data-MC Comparison, Off Resonance Data: $|\cos\theta_{thrust}|$. The distributions $|\cos\theta_{thrust}|$ for the signal modes K (a), K_S (b), K^* (c), and K^{*0} (d) from the off resonance data. The relative background sizes are fixed by their cross sections, and the total background is then scaled to equal the Data area.

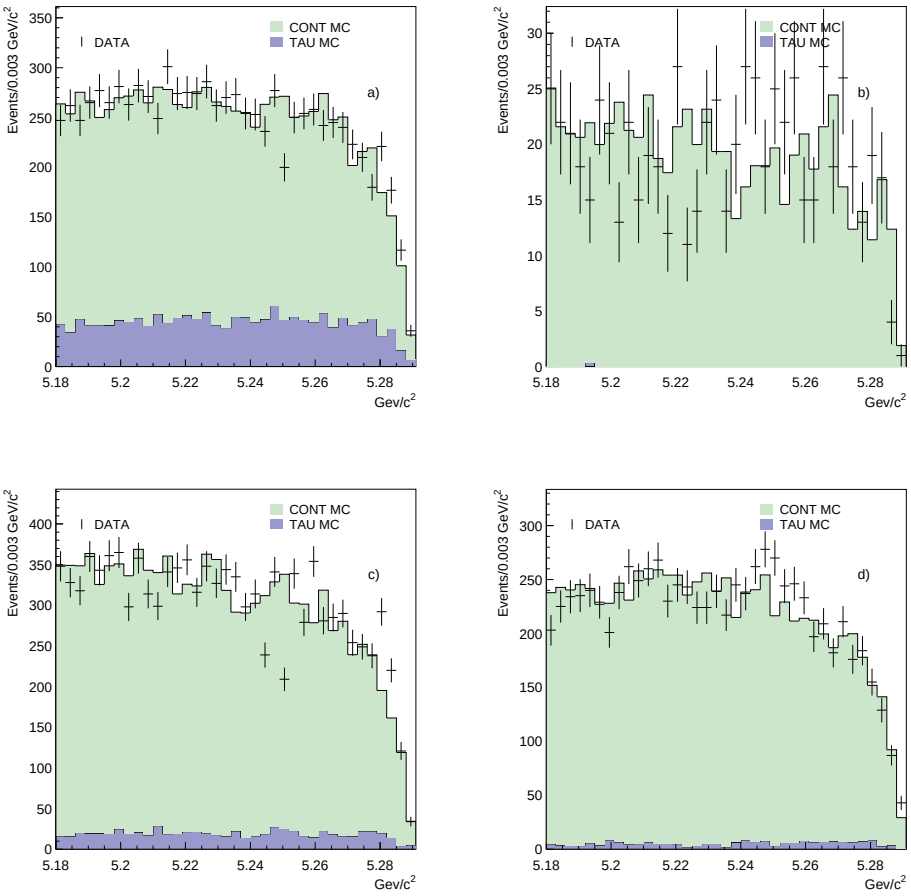

Figure 4.27: Data-MC Comparison, Off Resonance Data: M_B.

The distributions of M_B for the signal modes K (a), K_S (b), K^* (c), and K^{*0} (d) from the off resonance data. The relative background sizes are fixed by their cross sections, and the total background is then scaled to equal the Data area.

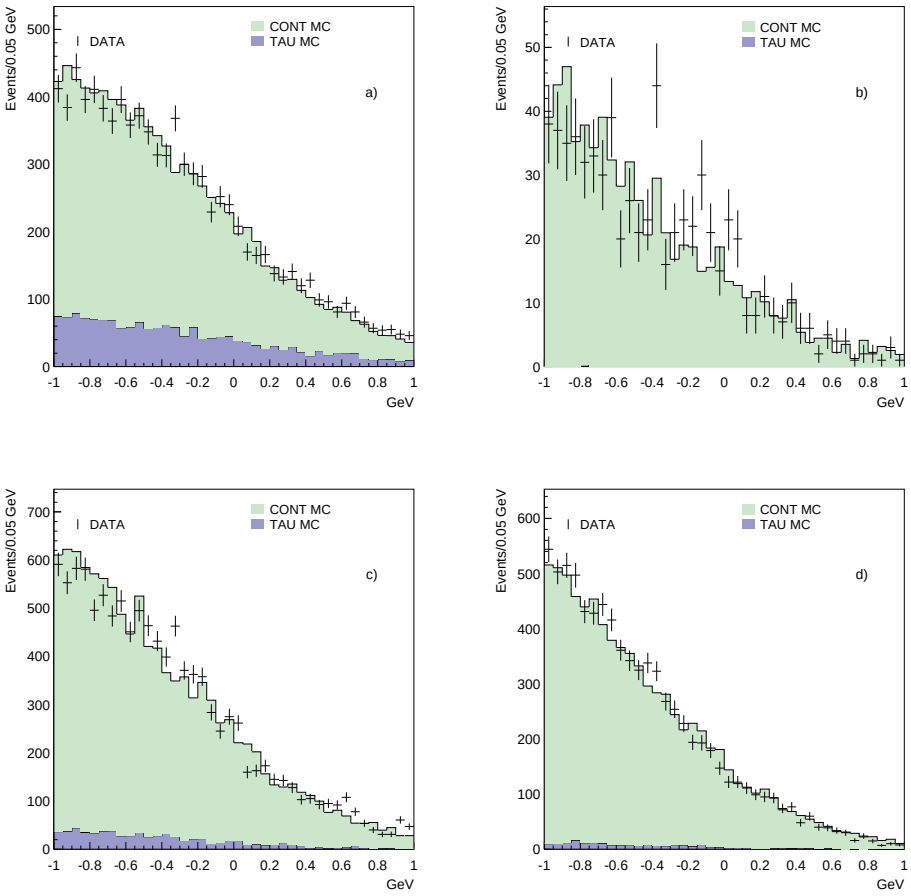

Figure 4.28: Data-MC Comparison, Off Resonance Data: ΔE.

The distributions of ΔE for the signal modes K (a), K_S (b), K^* (c), and K^{*0} (d) from the off resonance data. The relative background sizes are fixed by their cross sections, and the total background is then scaled to equal the Data area.

CHAPTER 5

UPPER LIMIT CALCULATION

5.1 Yield Extraction

In order to determine the upper limit on the Branching Fractions of $B \rightarrow K\nu\bar{\nu}$, we must decide on a method to measure the yields of both signal and background events in Data. There are three methods which we considered: an unbinned maximum likelihood fit, a simple cut assuming that there is no background, and a simple cut in the presence background. This analysis exists in a regime where we expect no signal and little background. To determine the best method of extracting the yields, we used a toy Monte Carlo study in which we used simple signal and background PDFs and calculated signal yield upper limits using all three methods. To do this we chose the signal PDF to be a unit Gaussian and the background PDF to be flat.

Using these PDFs. we generated 200 Monte Carlo experiments for each combination of signal and background $0 \leq n_S \leq 5$ and $1 \leq n_B \leq 20$. For each experiment, we extracted the signal yield in three ways. First, we performed an unbinned maximum likelihood fit and calculated the signal and background yields and the 90% confidence level upper limit on the signal yield. Second, we applied

cuts at $\pm 1\sigma$, $\pm 2\sigma$, and $\pm 3\sigma$, and simply assumed that all events which fell within the cuts were signal. Third, we applied cuts at $\pm 1\sigma$, $\pm 2\sigma$, and $\pm 3\sigma$ and performed a background subtraction using the average yield outside the cuts to determine the amount of background in the signal box. A comparison of these methods can be seen in Figure 5.1.

We use Equation 5.1 to calculate the 90% confidence level upper limit on the signal yield. It defines the probability $1 - \epsilon$ that for a known background rate μ_B and signal rate $\mu_S = N$ that n_0 or more events are observed with $n_B \leq n_0$, from Section 28.6.4 of Ref. [33]. To extract the signal upper limit for a known μ_B and n_0 we adjust N until we obtain the desired confidence level.

$$1 - \epsilon = 1 - \frac{e^{-(\mu_B+N)} \sum_{n=0}^{n_0} \frac{(\mu_B+N)^n}{n!}}{e^{(-\mu_B)} \sum_{n=0}^{n_0} \frac{\mu_B^n}{n!}} \tag{5.1}$$

For the case where we count all events in the signal box as signal, we are simply setting $\mu_B = 0$. We also calculate the upper limit in the presence of background by estimating μ_B from the sidebands. The results of this calculation can be seen in Figure 5.2 for the 3 simple cuts in comparison with the upper limit derived from the fit in the cases where no signal events were generated and where three signal events were generated.

The conclusion we draw from this is that in the regime of small expected signal and background yields, statistical fluctuations in the Data exert far more influence over the final limit than does the method of limit calculation. In other words, it makes little difference whether we use a fit or cut. Another way to reconcile the lack of difference between the fit and cut methods is the realization that applying

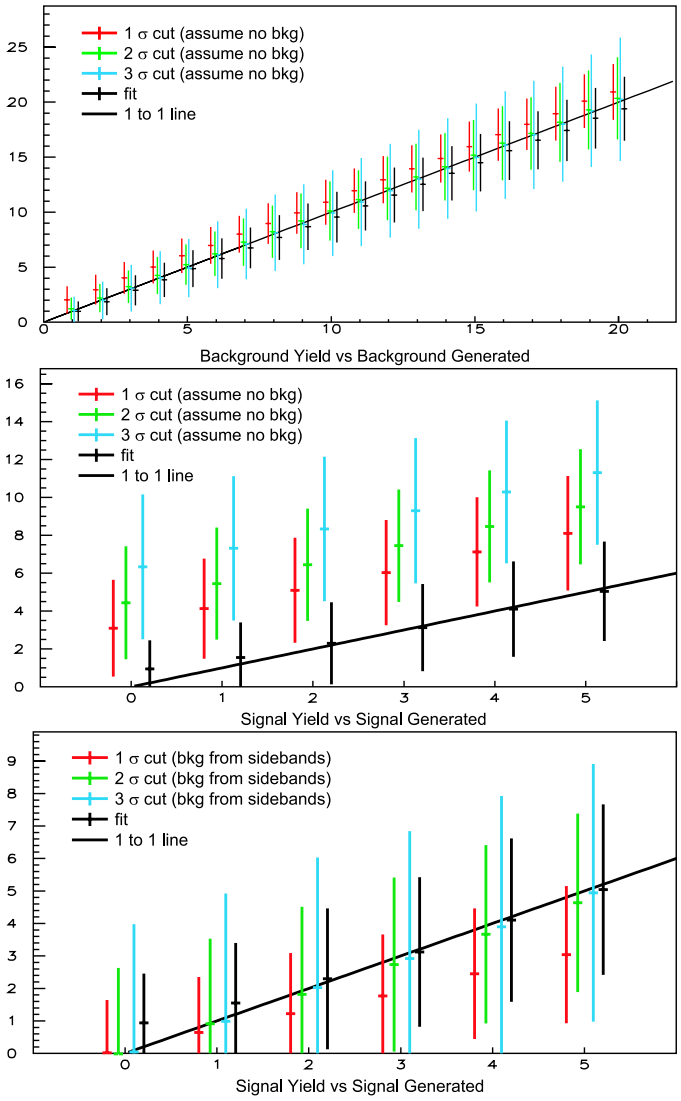

Figure 5.1: Yield Extraction Study: Yields.

Background and signal yields versus the number of events generated of each. The error bars are representative of the spread of values in each bin. In the top plot, each point is summed over the different amounts of signal generated, similarly, in the bottom two, each bin contains all generated amounts of background.

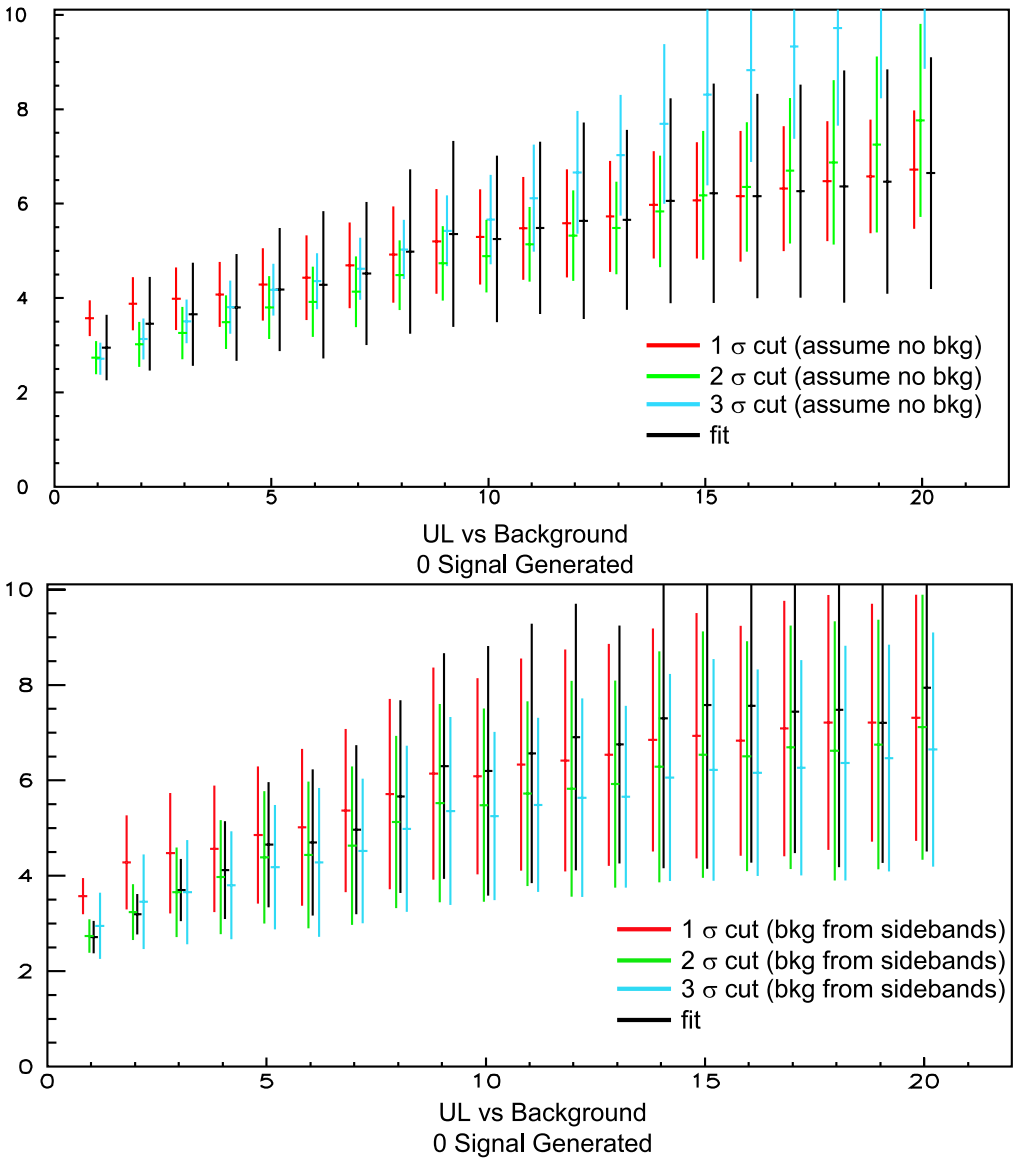

Figure 5.2: Yield Extraction Study: Upper Limits.

Comparisons of upper limits calculated using a fit and 3 sets of cuts with and without the assumed presence of background. Again, the error bars represent the spread of the 200 toy Monte Carlo experiments.

cuts is equivalent to fitting with a notch shaped PDF. In this sparsely populated regime, there is little to be gained by changing the weight assigned to events that just happen to fall in the wings of the signal PDF. The exception is in the case where we assume $\mu_B = 0$, we can see that for the loosest cut ($\pm 3\sigma$), when the background gets large the limit does increase faster. This should not come as a surprise and simply illustrates the importance of selecting reasonable cuts.

5.2 Cut Optimization

After deciding to use a simple cut yield extraction, we use that method to optimize the cut values. First we need to decide what constitutes our signal box and which variables define the cut space. We are compelled by the limited information available in our signal B and our desire to avoid using specific models of the decay $B \to K\nu\bar{\nu}$ to not use any information from the signal B. Due to this, in the following discussion it is important to remember that though we choose to use variables which are familiar to B meson decay analyses, without exception, the variables which define our signal box and cut space refer to the companion B. That said, we define our signal box using the beam constrained mass (M_B) and energy (ΔE) of the companion B. Detailed descriptions of these variables can be found in Section 4.4.

The goal of our cut optimization is to use Monte Carlo to choose a set of cuts that result in the best limit on the branching fraction of each $B \to K\nu\bar{\nu}$ mode in

an unbiased way. Our branching fraction is of the form

$$\mathcal{B} \sim \frac{Y_{sig}}{\epsilon_{sig}} \tag{5.2}$$

where the signal yield (Y_{sig}) can be the result of background subtracted yield from the signal box, and ϵ_{sig} is the signal reconstruction efficiency. Similarly, the upper limit on the branching fraction is of the form

$$U_{\mathcal{B}} \sim \frac{U_{Y_{sig}}}{\epsilon_{sig}}. \tag{5.3}$$

It would be incorrect to simply choose cuts which minimize the upper limit in Equation 5.3. The Monte Carlo sample we use represents a single sample which is representative of our Data sample. So rather than the set of cuts which minimizes the upper limit on this particular sample, we would like to find a method for generalizing Equation 5.3 to the ensemble of data sets of which the CLEO data set is one.

To this end, we define the Poisson sensitivity (S_α) to be the average upper limit, at confidence level α, achieved over an ensemble of samples assuming there is no signal ($\mu_S = 0$) and the background is Poisson distributed with mean μ_B. The Poisson sensitivity for a given background rate μ_B and confidence level α is given by

$$S_\alpha(\mu_B) = \sum_{n=0}^{\infty} U_\alpha(n, \mu_B) P(n, \mu_B) \tag{5.4}$$

where $U_\alpha(n, \mu_B)$ is the upper limit as calculated from Equation 5.1 with background rate μ_B, observed events n, at confidence level α. $P(n, \mu_B)$ is the value of a Poisson distribution at n with mean μ_B. The sensitivity is therefore the upper limit

calculated for all possible measured background yields weighted by the probability of seeing that yield which is Poisson distributed with mean μ_B.

The expression that will represent the best upper limit on the branching fraction over an ensemble of experiments (our cut figure of merit) with background rate μ_B and no measured signal yield follows from Equation 5.3 and Equation 5.4.

$$FOM = \frac{S_\alpha(\mu_B)}{\epsilon_{sig}} \tag{5.5}$$

For each cut combination, we extract μ_B and ϵ_{sig} from our background Monte Carlo samples. Then we assume that the background yield is equal to the mean background rate seen over an ensemble of independent experiments and calculate the sensitivity. Then we calculate the signal efficiency from the signal yield. With a value of the FOM for each cut combination, we choose the cut which results in the smallest FOM.

In order to get a more global picture of the "cut space" including correlations we proceeded to apply all combinations of the cuts listed in Table 5.1 for the charged and neutral kaon signal modes. In addition to the variables described in Chapter 4 we also investigated the effect of not reconstructing the so-called "dirty modes" marked in Table 4.1 and Table 4.3. For the neutral modes, we also investigated changing the signal box, as seen in the last line of Table 5.1. Permutations being what they are, this resulted in a large number of cut combinations that were then applied to all Monte Carlo samples: Signal, Generic $B\bar{B}$, Generic Continuum, and τ Pair, for each signal mode analysis. Then we calculated $S_{90\%}(\mu_B)$ and ϵ_{sig} for each combination.

Table 5.1: Cut Optimization Ranges

Cut	Analysis	
	K^+,K^{*+}	K_S, K^{*0}
$\|cos\theta_{thrust}\| <$	0.65, 0.70, 0.75, 0.80, 0.85, 0.90, 0.95	0.80, 0.85
$E_{left} <$	0.10, 0.20, 0.30, 0.40, 0.50, 0.60, 0.70, 0.80, 0.90, 1.00, 1.25, 1.50, 1.75, 2.00	0.10, 0.20, 0.30, 0.40, 0.50, 1.00, 1.50, 2.00, 2.50, 3.00
$q^2 <$	0.25, 0.50, 1.00, 1.20, 1.40, 1.60, 1.80, 2.00, 2.25, 2.50, 2.75, 3.00, 3.50, 4.00	1.00, 2.00, 3.00, 4.00, 5.00, 6.00, 7.00, 8.00
$N_{\pi^0\ left} \leq$	0, 1, 2	0, 1, 2, 3, 4, 5
R_2	0.5	0.1, 0.2, 0.3, 0.4, 0.5
$M_B >$	5.2725	5.2400, 5.2500, 5.2600, 5.2700. 5.2725
$\Delta E >$	-0.25	-0.25, -0.1

Figures 5.3 to 5.6 show ϵ_{sig} versus $S_{90\%}(\mu_B)$. The region of cut space that is of interest is the outer envelope of this plot, where the signal efficiency is highest and the background is lowest. If there are optimum cuts they will occur at "knees" in the plot where the signal efficiency begins decreasing faster as the background upper limit sensitivity decreases. This is to say we want to maximize the denominator in Equation 5.5, ϵ_{sig} and minimize $S_{90\%}(\mu_B)$. (Maximize signal and minimize background, quite an intellectual breakthrough.) For clarity, we also plot the FOM versus ϵ_{sig} and $S_{90\%}(\mu_B)$. These plots can be seen in Figures 5.7 to 5.14.

In the end, we found the cuts that gave the optimum figure of merits for each analysis and these are listed in Table 5.2. We found that we gained nothing by leaving out the dirty D reconstruction modes, but we did by leaving out all of the dirty B modes.

5.3 Background Check

In Section 4.6, we showed the agreement between Data and Monte Carlo samples while only requiring there be no tracks leftover after the reconstruction. With optimum cuts in hand, we returned to check the background predictions of our Monte Carlo simulation. Figures 5.15 and 5.16 show the agreement in shape between the Data and Monte Carlo samples. As before, the relative contributions of background Monte Carlo samples are set by their branching fractions, and then the background is then scaled to equal the area of the Data plot. This is a correction of approximately 10%.

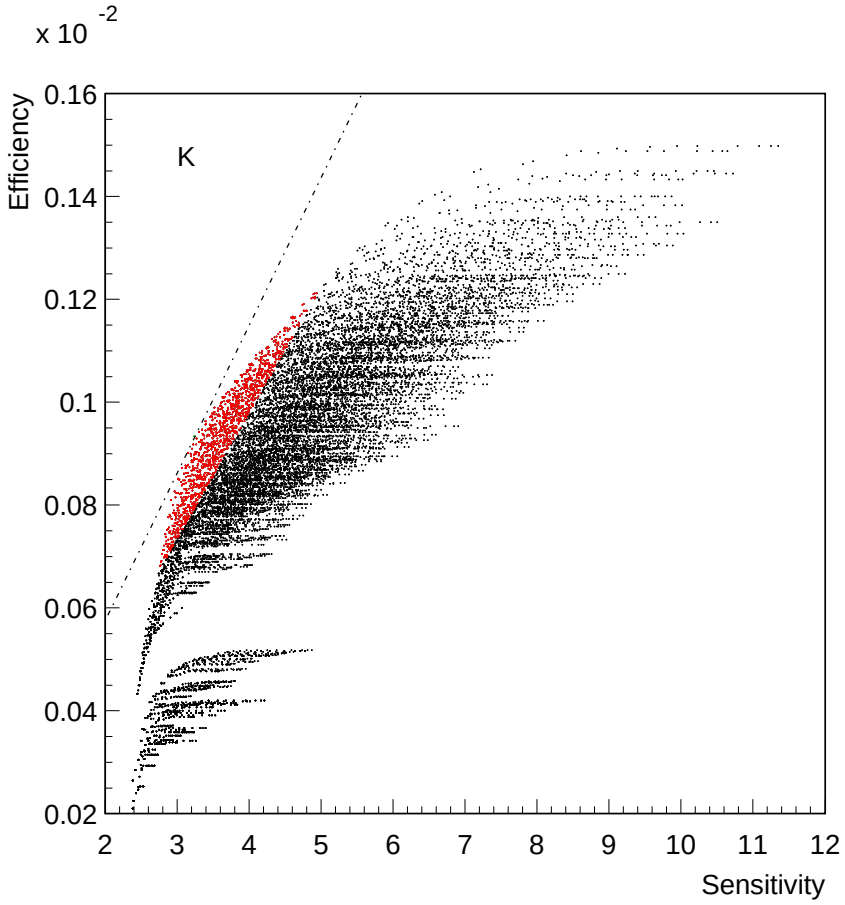

Figure 5.3: Cut Optimization: ϵ_{sig} vs. $S_{90\%}(\mu_B)$, K^+.

Each dot represents a single combination of cut values. The break in the plot at low efficiency and sensitivity is due to the non-uniformity of the cuts. The line is tangent to the distribution at the optimum cut value. This line is repeated in Figures 5.7 and 5.8.

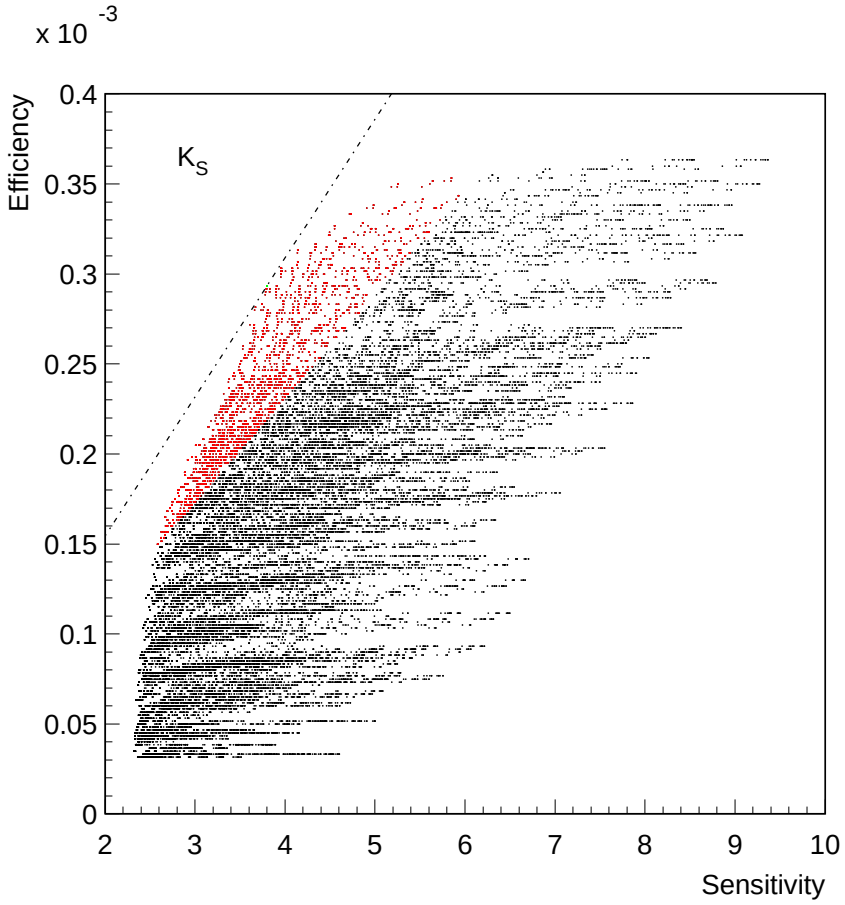

Figure 5.4: Cut Optimization: ϵ_{sig} vs. $S_{90\%}(\mu_B)$, K_S.

Each dot represents a single combination of cut values. The break in the plot at low efficiency and sensitivity is due to the non-uniformity of the cuts. The line is tangent to the distribution at the optimum cut value. This line is repeated in Figures 5.9 and 5.10.

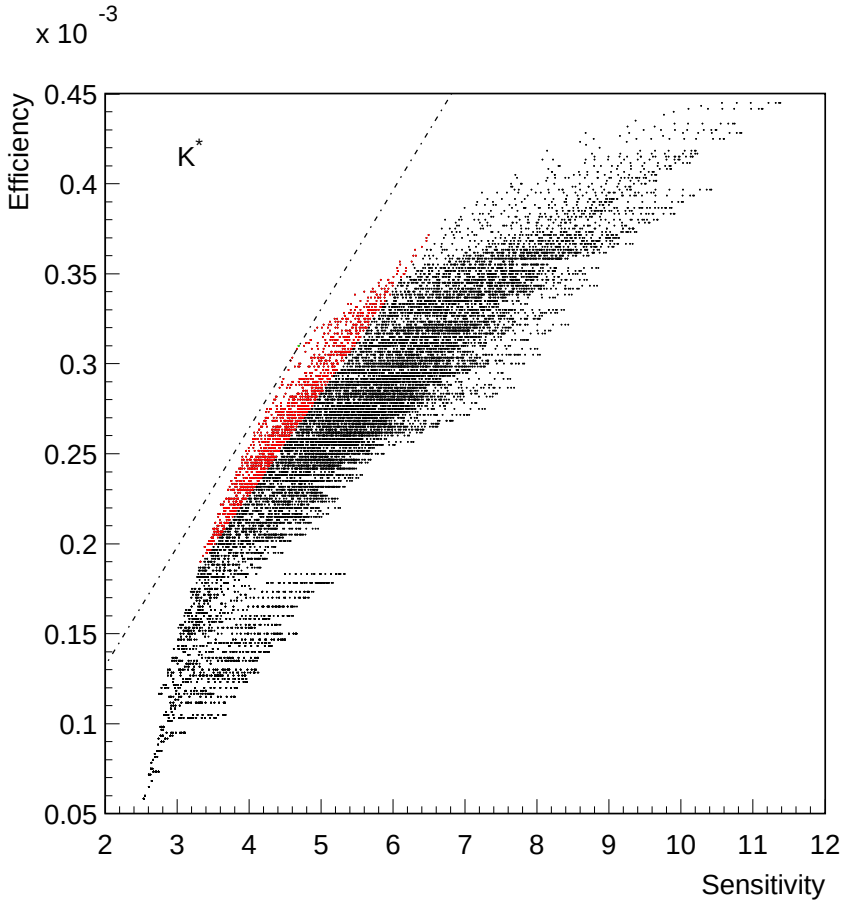

Figure 5.5: Cut Optimization: ϵ_{sig} vs. $S_{90\%}(\mu_B)$, K^{*+}.

Each dot represents a single combination of cut values. The break in the plot at low efficiency and sensitivity is due to the non-uniformity of the cuts. The line is tangent to the distribution at the optimum cut value. This line is repeated in Figures 5.11 and 5.12.

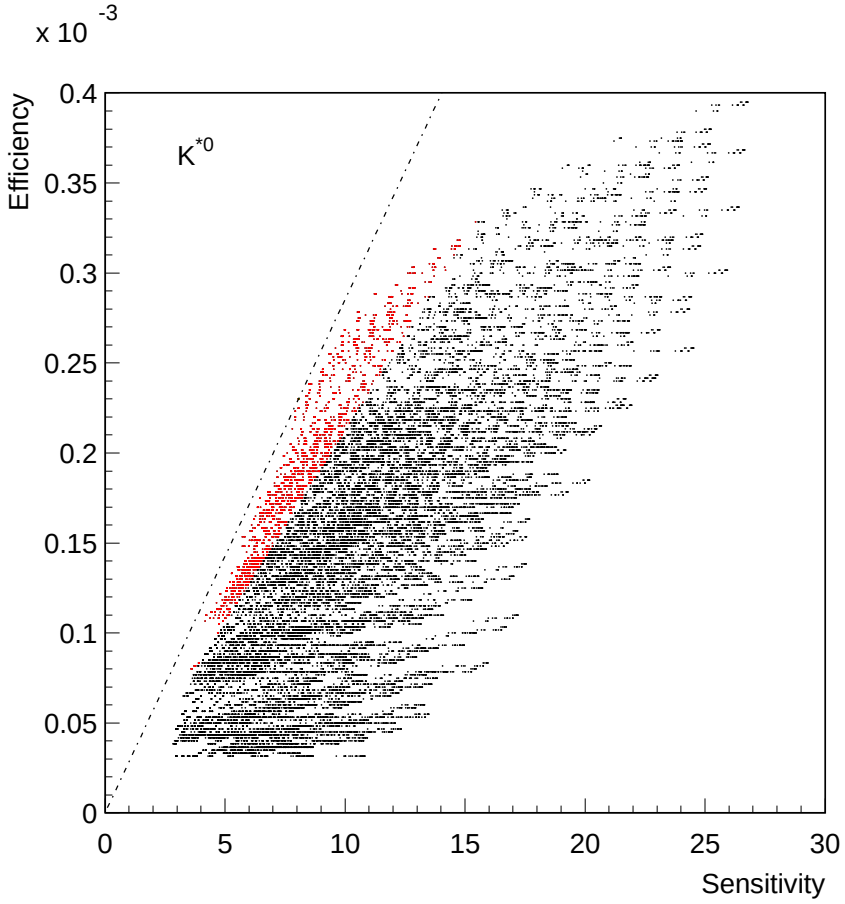

Figure 5.6: Cut Optimization: ϵ_{sig} vs. $S_{90\%}(\mu_B)$, K^{*0}.

Each dot represents a single combination of cut values. The line is tangent to the distribution at the optimum cut value. This line is repeated in Figures 5.13 and 5.14.

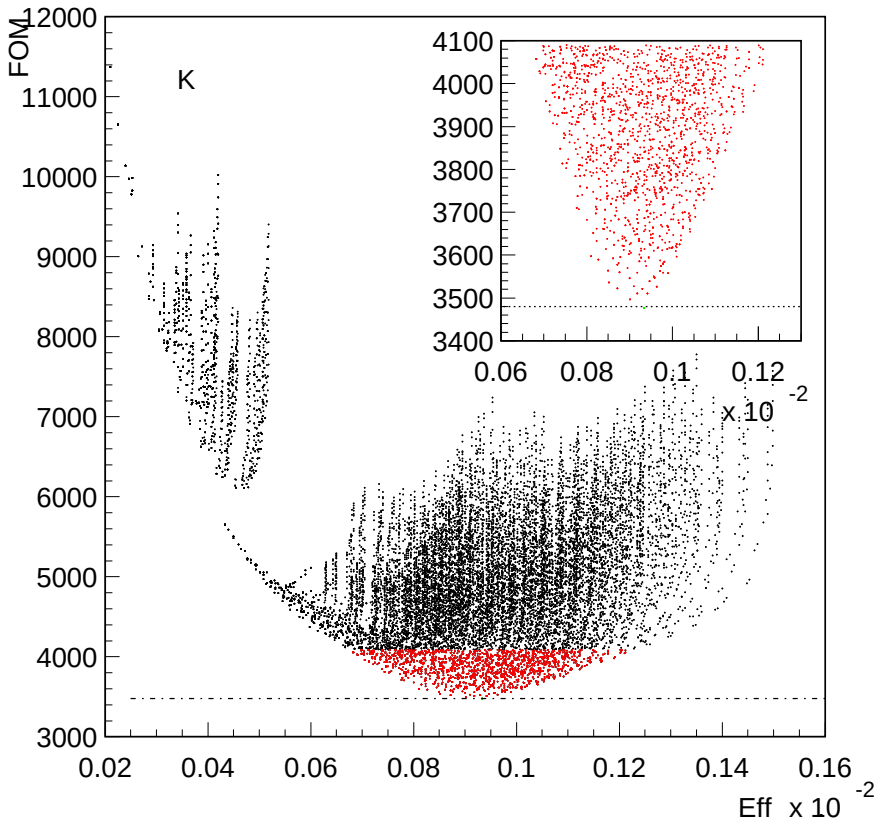

Figure 5.7: Cut Optimization: Cut FOM vs. ϵ_{sig}, K^+.

This distribution represents the same information as in Figure 5.3. The optimum cut combination is the minimum value of the cut FOM and is marked by the line. The inset contains the best 10% combinations and is included to show the well defined nature of the minimum.

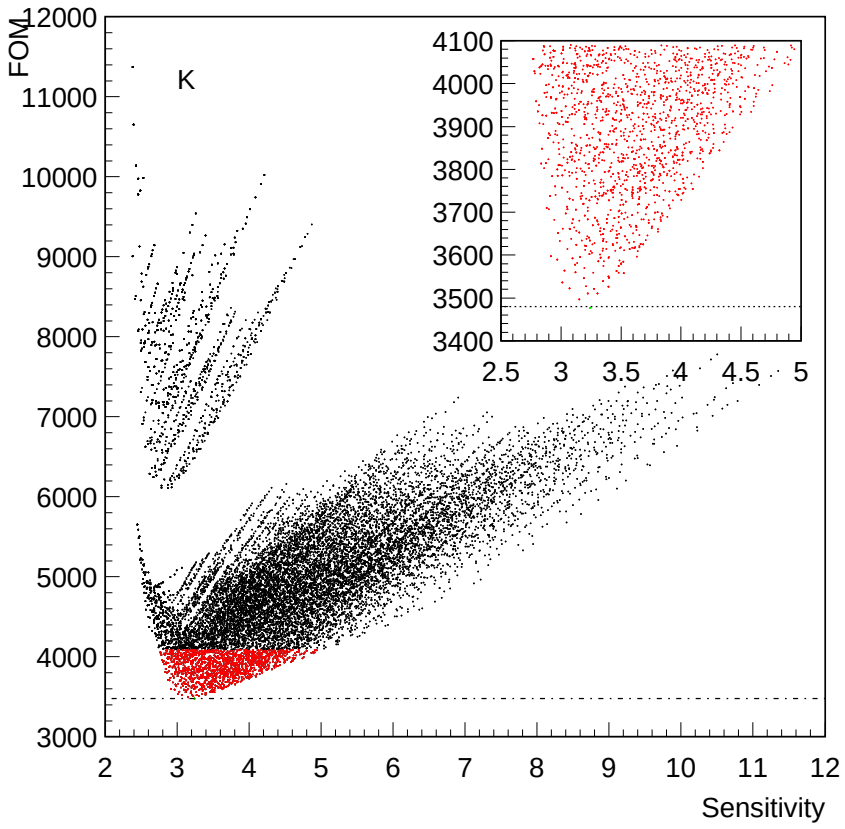

Figure 5.8: Cut Optimization: Cut FOM vs. $S_{90\%}(\mu_B)$, K^+.

This distribution represents the same information as in Figure 5.3. The optimum cut combination is the minimum value of the cut FOM and is marked by the line. The inset contains the best 10% combinations and is included to show the well defined nature of the minimum.

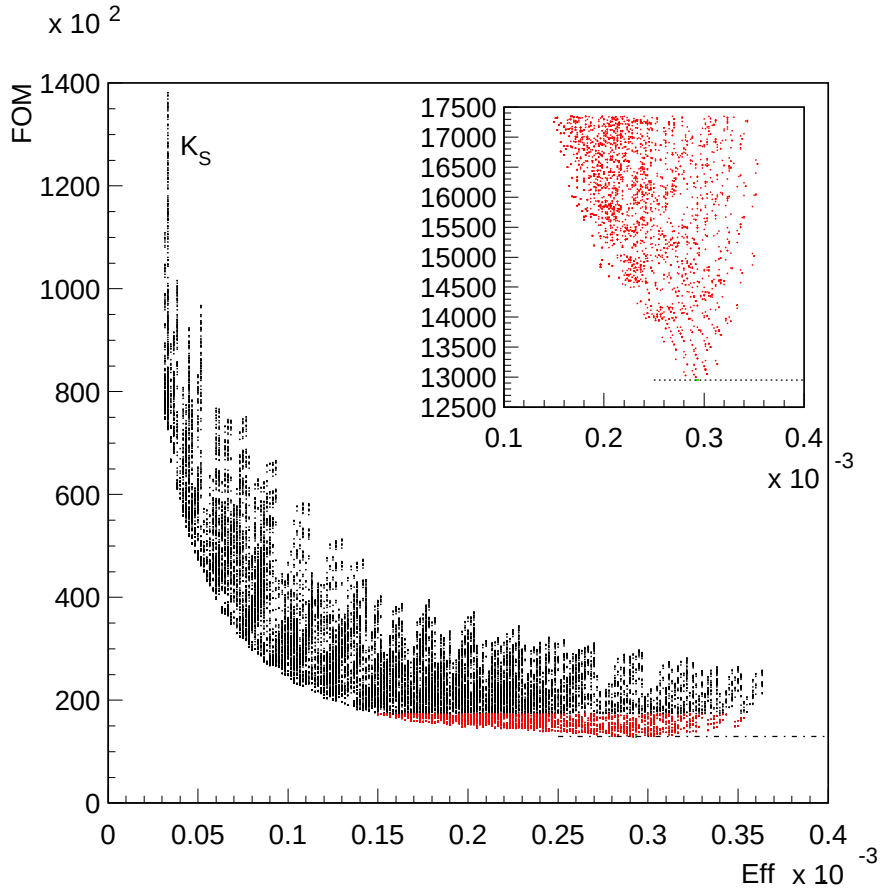

Figure 5.9: Cut Optimization: Cut FOM vs. ϵ_{sig}, K_S.

This distribution represents the same information as in Figure 5.4. The optimum cut combination is the minimum value of the cut FOM and is marked by the line. The inset contains the best 10% combinations and is included to show the well defined nature of the minimum.

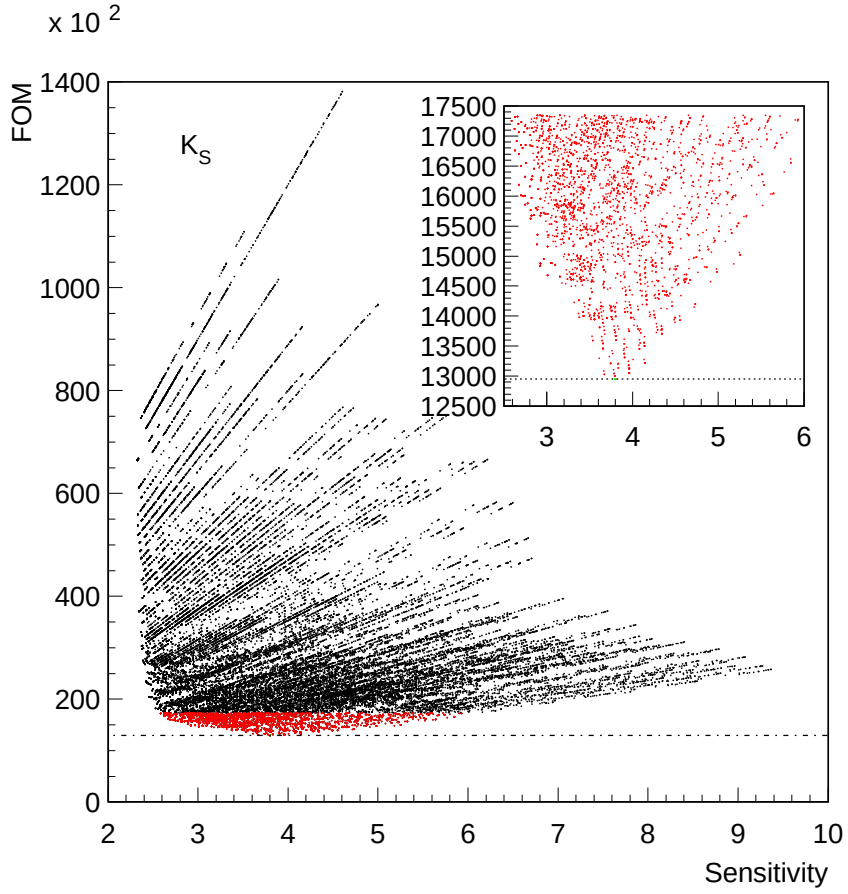

Figure 5.10: Cut Optimization: Cut FOM vs. $S_{90\%}(\mu_B)$, K_S.

This distribution represents the same information as in Figure 5.4. The optimum cut combination is the minimum value of the cut FOM and is marked by the line. The inset contains the best 10% combinations and is included to show the well defined nature of the minimum.

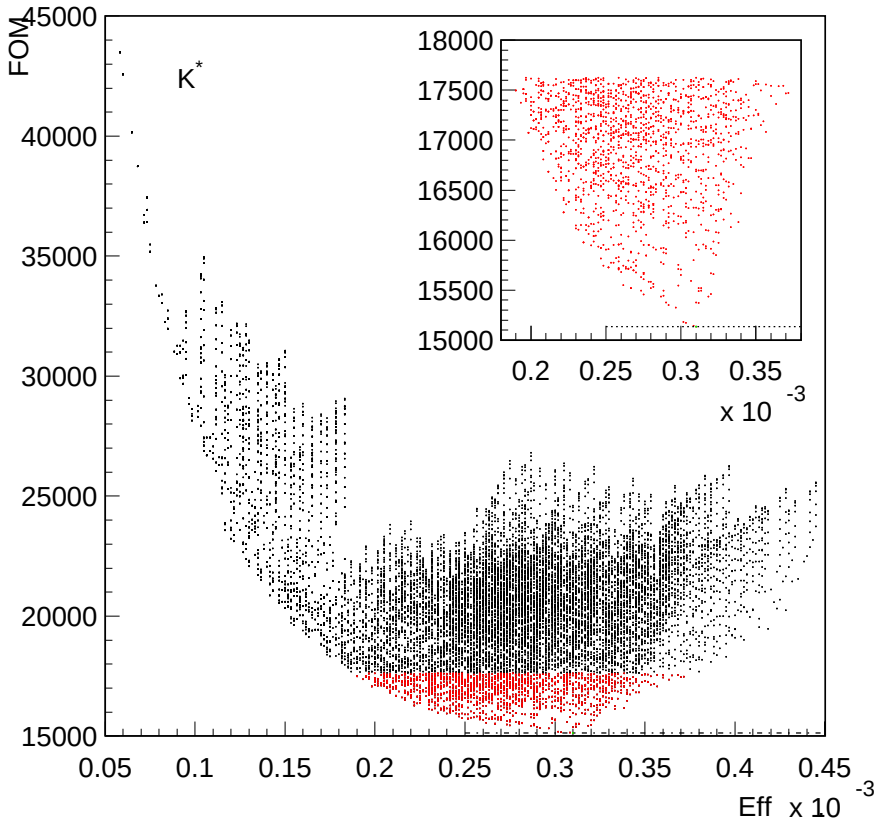

Figure 5.11: Cut Optimization: Cut FOM vs. ϵ_{sig}, K^*.

This distribution represents the same information as in Figure 5.5. The optimum cut combination is the minimum value of the cut FOM and is marked by the line. The inset contains the best 10% combinations and is included to show the well defined nature of the minimum.

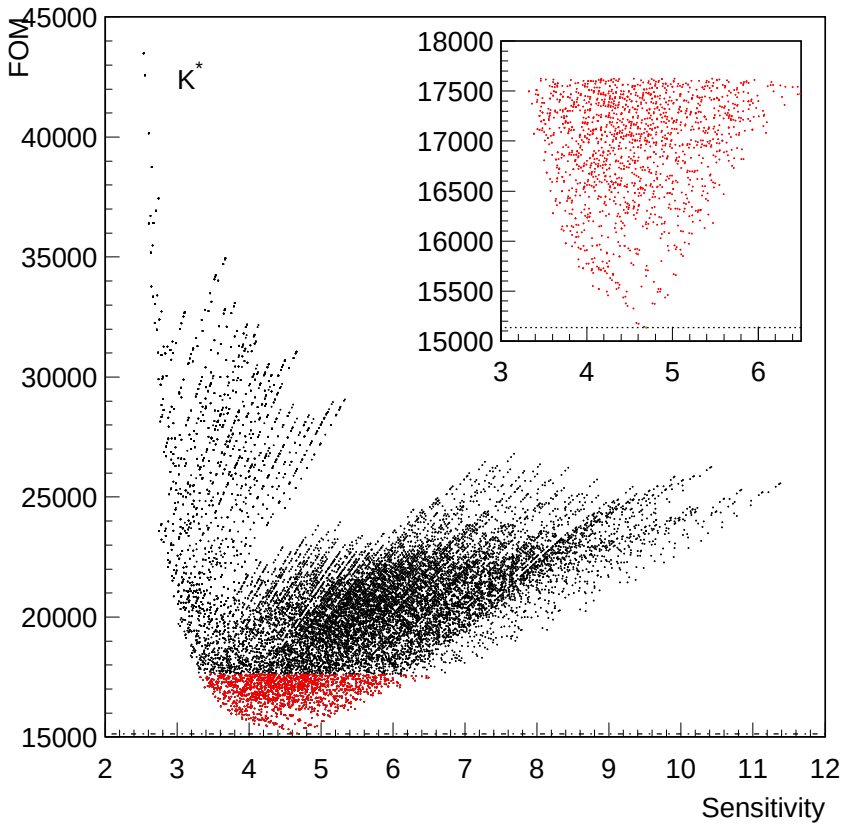

Figure 5.12: Cut Optimization: Cut FOM vs. $S_{90\%}(\mu_B)$, K^*.

This distribution represents the same information as in Figure 5.5. The optimum cut combination is the minimum value of the cut FOM and is marked by the line. The inset contains the best 10% combinations and is included to show the well defined nature of the minimum.

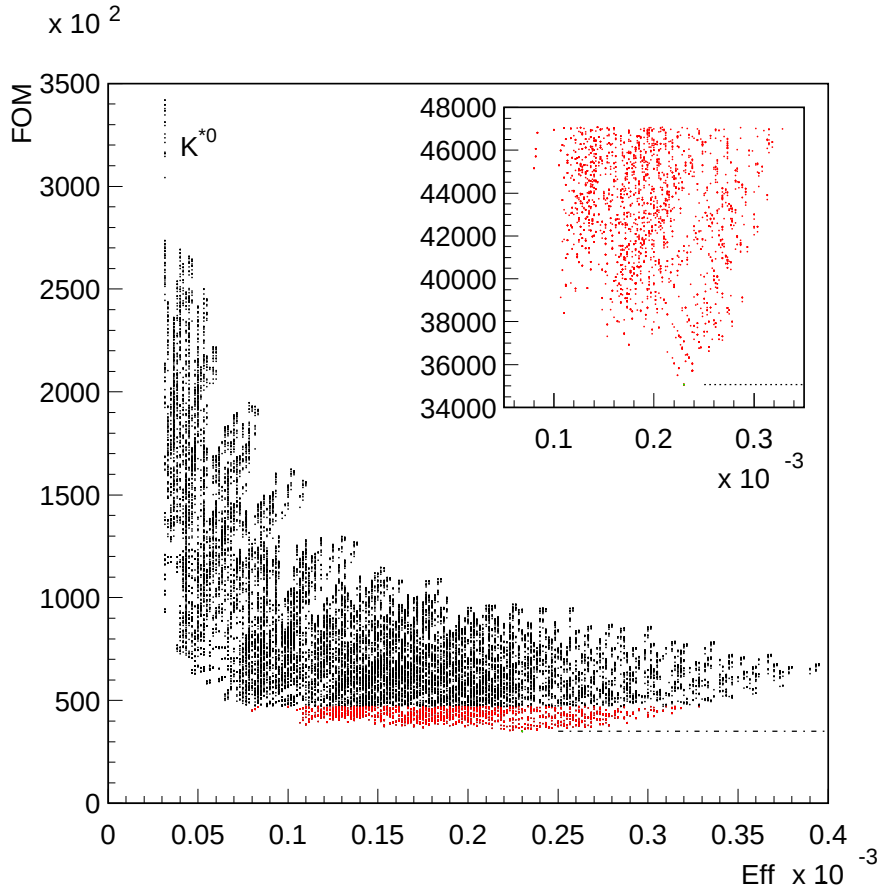

Figure 5.13: Cut Optimization: Cut FOM vs. ϵ_{sig}, K^{*0}.

This distribution represents the same information as in Figure 5.6. The optimum cut combination is the minimum value of the cut FOM and is marked by the line. The inset contains the best 10% combinations and is included to show the well defined nature of the minimum.

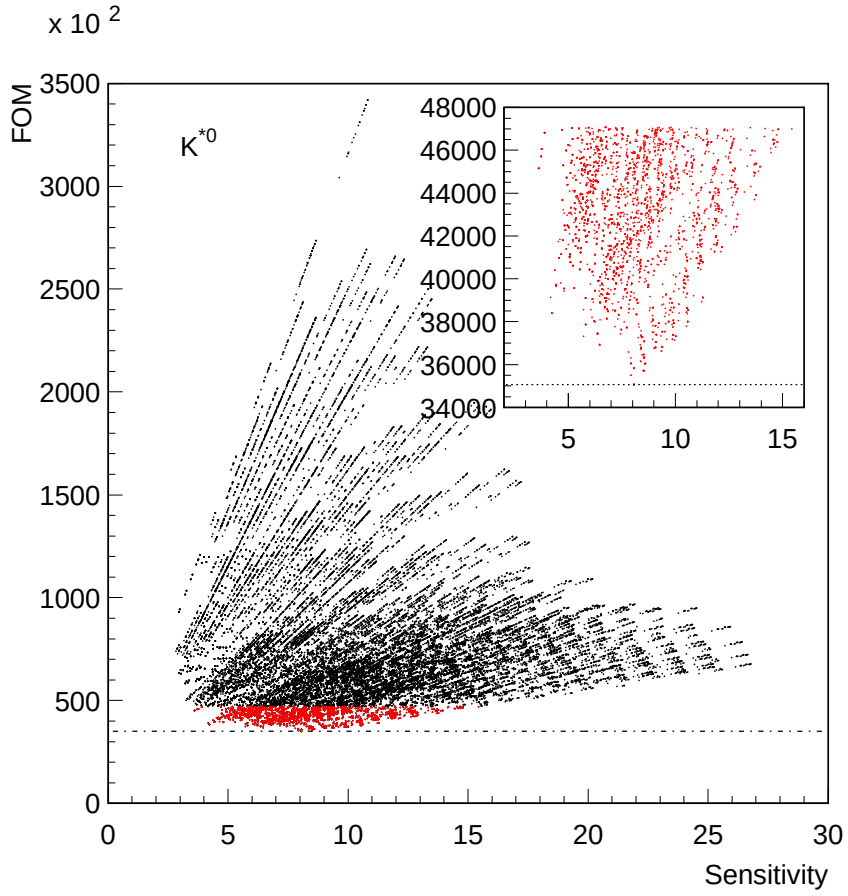

Figure 5.14: Cut Optimization: Cut FOM vs. $S_{90\%}(\mu_B)$, K^{*0}.

This distribution represents the same information as in Figure 5.6. The optimum cut combination is the minimum value of the cut FOM and is marked by the line. The inset contains the best 10% combinations and is included to show the well defined nature of the minimum.

Table 5.2: Optimum Cuts

Cut	Analysis			
	K^+	K^{*+}	K_S	K^{*0}
$\|cos\theta_{thrust}\| <$	0.80	0.85	0.80	0.80
$E_{left} <$	0.20	0.30	0.30	0.20
$q^2 <$	2.75	2.50	8.00	8.00
$N_{\pi^0\ left} \leq$	2	2	5	1
R_2	0.5	0.5	0.5	0.4
M_B	5.2725	5.2725	5.2725	5.2725
ΔE	-0.25	-0.25	-0.25	-0.25
$S_{90\%}(\mu_B)$	3.246	4.692	3.799	8.065
ϵ_{sig} $(\times 10^{-4})$	9.333	3.100	2.933	2.300
Cut FOM	3477	15140	12950	35060

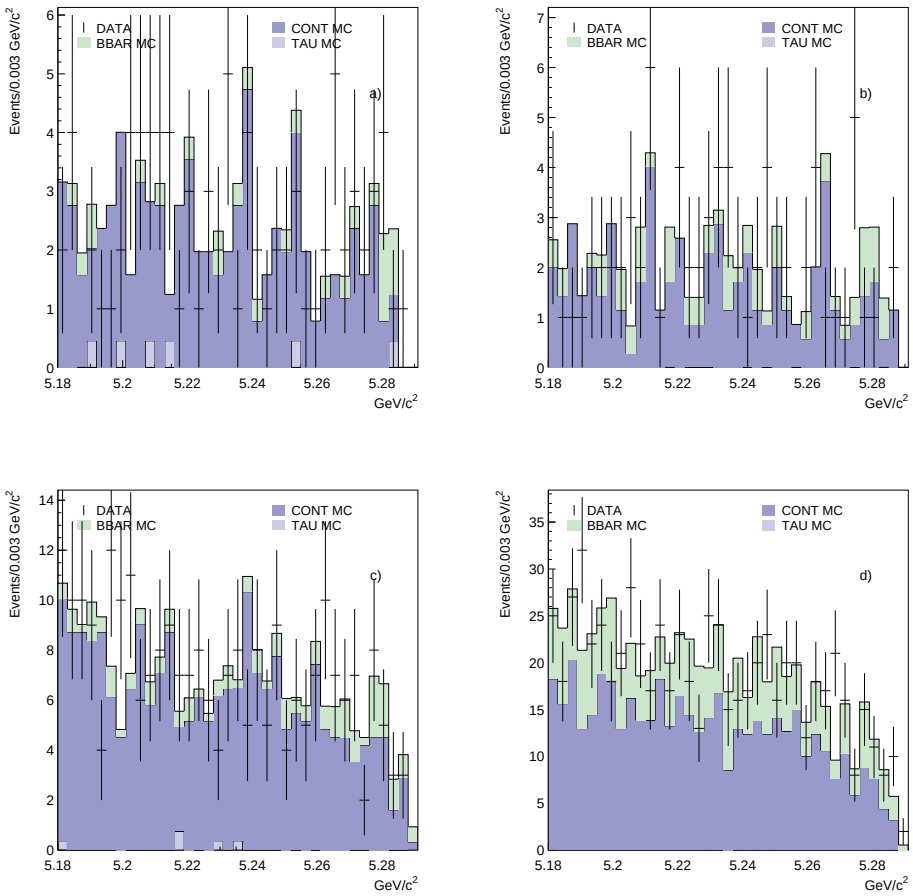

Figure 5.15: Data-MC Comparison: Optimum Cuts, M_B.

The distributions of B_{cm} for the signal modes K (a), K_S (b), K^* (c), and K^{*0} (d) after applying optimum cuts. The background Monte Carlo sample has been scaled to have the same area as the Data.

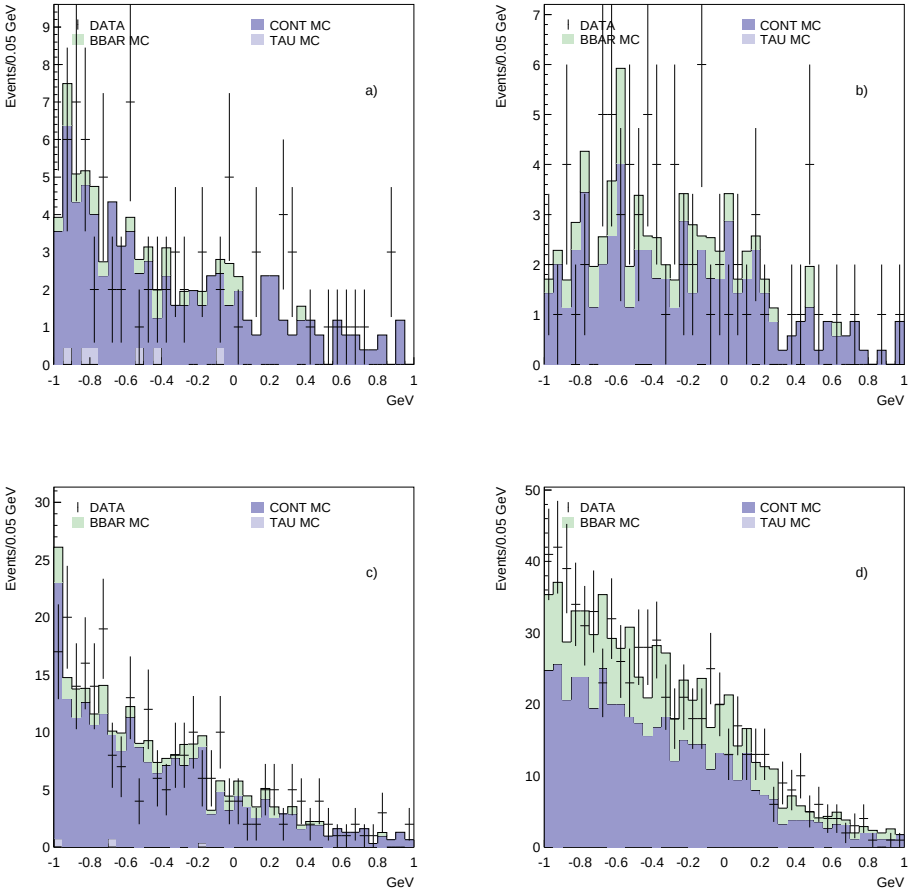

Figure 5.16: Data-MC Comparison: Optimum Cuts, ΔE.

The distributions of ΔE for the signal modes K (a), K_S (b), K^* (c), and K^{*0} (d) after applying optimum cuts. The background Monte Carlo sample has been scaled to have the same area as the Data.

5.4 Signal Yield Upper Limit

To use Equation 5.1 to calculate the upper limit we must know the yield in the signal box n_0, and the background rate μ_B. Extracting the signal yield is straightforward, but μ_B is a touch more complicated. We use the ΔE sideband to estimate the background rate in the signal box. To project the background into the signal box, we use the slope of the background Monte Carlo ΔE sideband distributions. These distributions with their fits can be seen in Figure 5.17.

Using the slope of the background and the yield in the high and low data sidebands, we estimate the background in the signal box. With the number of observed events in the signal box, we are able to use Equation 5.1, but there is a complication. As explained in Section 5.1, the background rate μ_B in Equation 5.1 is known with perfect certainty. In our case this is not true. In order to account for this we did $50,000$ toy Monte Carlo experiments in which we threw a Poisson distributed number for the yield in the low and high sideband regions and the signal box. The means of these distributions were set to the observed data values. For each experiment, the signal box background rate, μ_B was calculated and Equation 5.1 used to calculate the 90% Confidence Level upper limit on the signal component of the yield in the signal box. The final Data distributions are shown in Figure 5.18 and the results are summarized in Table 5.3.

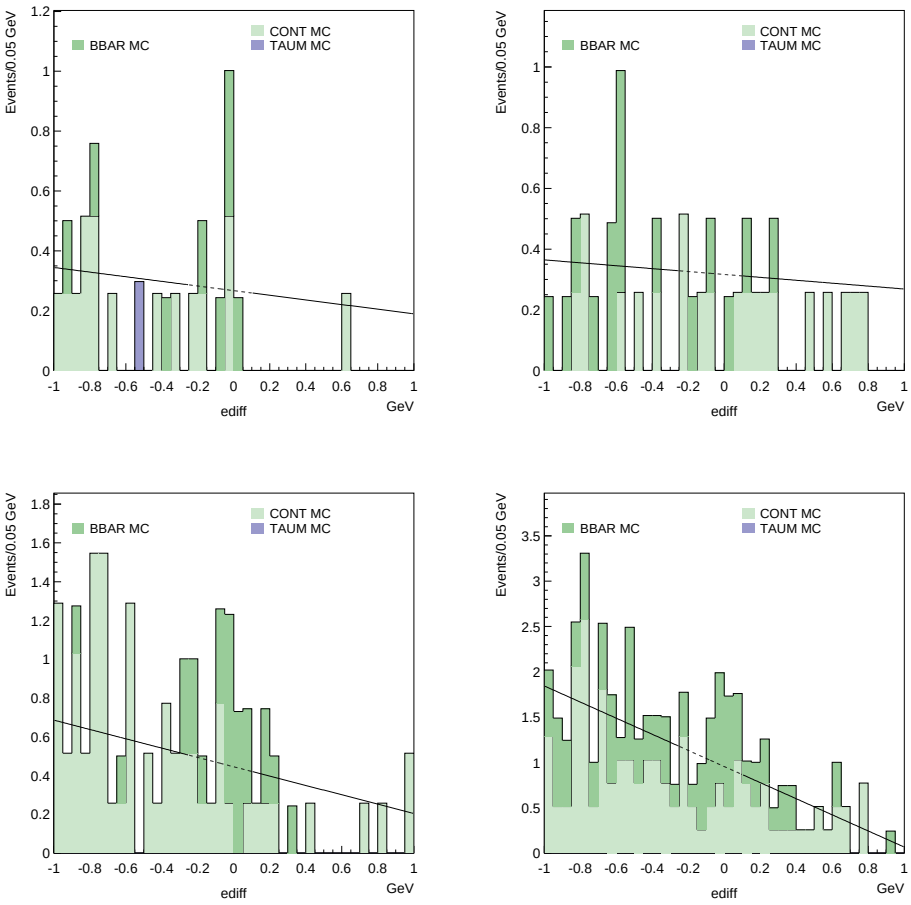

Figure 5.17: Signal Yield: μ_B Fit.

The ΔE distributions of background MC with the associated fit used to estimate the background rate in the signal box for modes K (a), K_S (b), K^* (c), and K^{*0} (d) after applying optimum cuts and the cut on M_B. The dotted signal box regions were not used in the fits

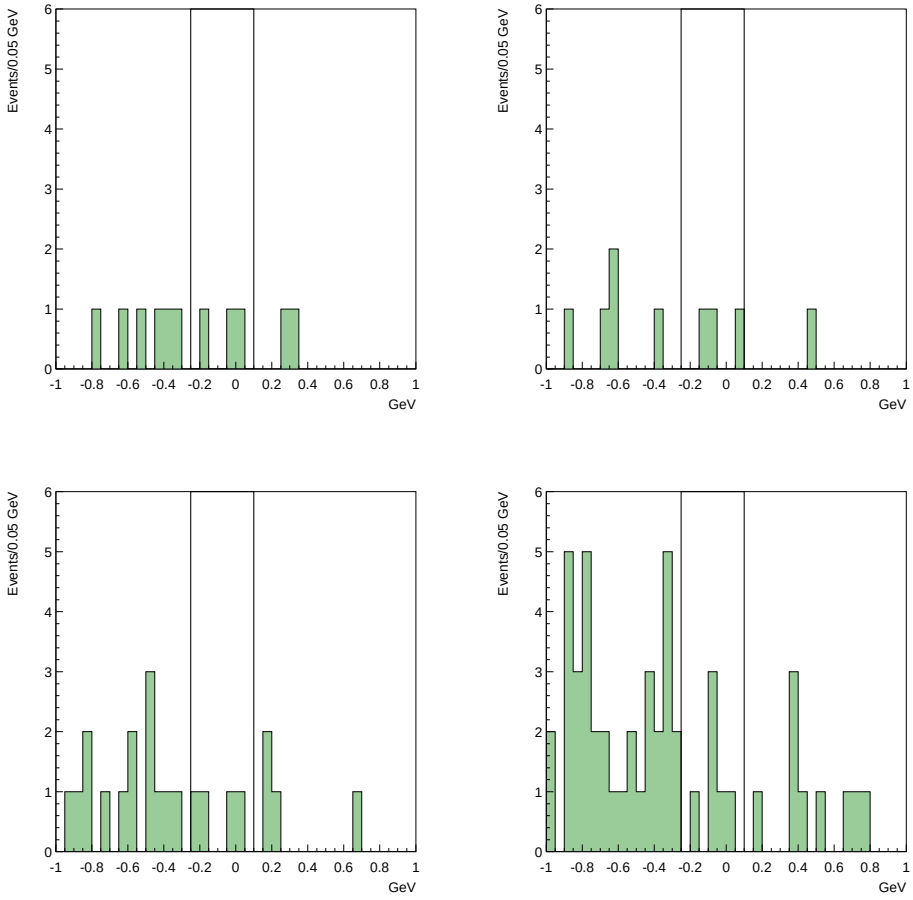

Figure 5.18: Signal Yield: Final Data ΔE Distribution.

The ΔE distributions for Data with the low and high sidebands and the signal box marked for for modes K (a), K_S (b), K^* (c), and K^{*0} (d).

Table 5.3: Summary of Yield Extraction

	Analysis			
	K^+	K_S	K^{*+}	K^{*0}
Background Slope $\left(\frac{\text{Events}}{\text{GeV}}\right)$	-1.549	-0.9585	-4.811	-17.77
Low Sideband (Events)	6	5	14	36
High Sideband (Events)	2	1	4	9
μ_B (Events)	1.809	1.374	4.108	10.38
Signal Box Yield (Events)	3	3	4	6
Signal Upper Limit (Events)	5.06	5.40	4.74	4.08
Smeared μ_B (Events)	1.813	1.373	4.106	10.38
Smeared Sig UL (Events)	5.216	5.525	5.030	4.329

5.5 Signal Efficiency

The signal efficiency is straightforward to calculate. The ΔE distribution for signal Monte Carlo is shown in Figure 5.19. A more difficult task is to quantify the systematic error on the signal reconstruction efficiency. This error has a significant impact on the final branching fraction upper limit. Since we base our signal reconstruction efficiency on our signal Monte Carlo samples, we must have a measure of how well our Monte Carlo simulation models Data. As our reconstruction depends on placing requirements on leftover tracks and energy, we choose to measure this agreement in terms of charged track and shower multiplicity.

In our signal Monte Carlo simulation, the companion B decays generically, just as in the Generic $B\bar{B}$ Monte Carlo, so one way to compare the modeling of our signal Monte Carlo is to compare the multiplicities of Generic $B\bar{B}$ to Continuum subtracted On Resonance Data, hereafter On-Off Data. We define the charged track multiplicity as simply the number of tracks which pass our track quality cuts (outlined in Appendix A.4). This is not a measure of the true multiplicity of $B\bar{B}$ events at the $\Upsilon(4S)$, but rather, what we will call reconstructed multiplicity. A measurement of the true charged track multiplicity at the $\Upsilon(4S)$ is described elsewhere [34]. Similarly, we measure the multiplicity of showers which pass our isolated shower cuts described in Appendix A.3. The energy of these showers make up the leftover energy E_{left}.

We can think of the total signal reconstruction efficiency in the following way. An $\Upsilon(4S)$will decay to a mode of multiplicity i, with a branching fraction B_i. Our

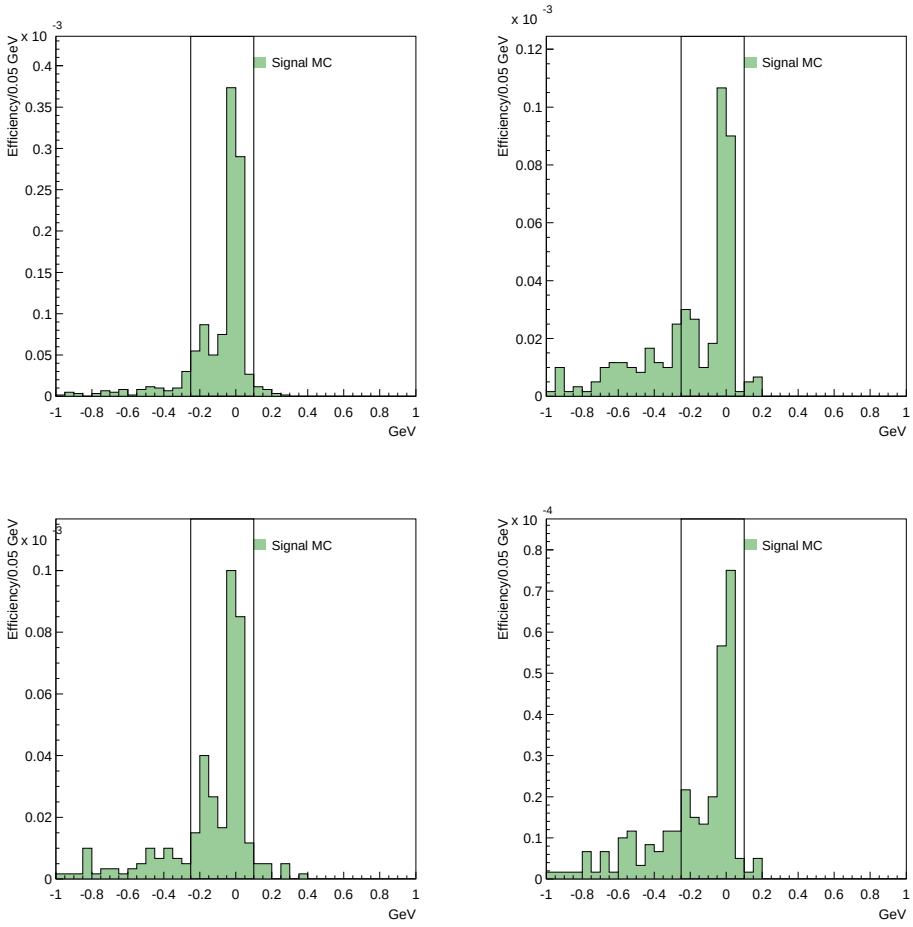

Figure 5.19: Signal Efficiency: Signal MC ΔE Distribution.

The ΔE distributions for Signal Monte Carlo with the low and high sidebands and the signal box marked for for modes K (a), K_S (b), K^* (c), and K^{*0} (d).

efficiency for reconstructing an event with multiplicity i as an event of multiplicity j is ϵ_{ij}. The total efficiency is then given by

$$\epsilon_{tot} = \sum_j \sum_i B_i \epsilon_{ij}. \tag{5.6}$$

Luckily, we don't need to calculate the efficiency using this equation. Instead we use it as a guide to calculating the systematic error on the total reconstruction efficiency. By comparing On-Off Data and $B\bar{B}$ Monte Carlo samples as a function of multiplicity, we get an estimate of the error on B_i as shown in Figure 5.20. This error is an estimate of how well our Monte Carlo simulation models the branching fractions of the various multiplicities.

For ϵ_{ij} we assign a systematic error of 2% for each charged track and 3% for each shower. Combined with the multiplicities shown in Figures 5.21 and 5.22 we calculate the contributions to the efficiency systematic error for charged track and shower multiplicities. These results are summarized in Table 5.4.

5.6 To the Limit

Now that we have the signal yield upper limit and the signal reconstruction efficiency, we are able to calculate the upper limit on the branching fractions of $B \to K\nu\bar{\nu}$. The equation for the branching fraction upper limit is

$$U_{\mathcal{B}} = \frac{U_{Y_{sig}}}{2 f_{+-(00)} N_{B\bar{B}} \epsilon_{sig} \left(1 - 1.28 \frac{\sigma_{fN\epsilon}}{fN\epsilon}\right)} \tag{5.7}$$

where $f_{+-(00)}$ is the fraction of $\Upsilon(4S)$ decays to charged $(+-)$ and neutral (00) B's [35], $N_{B\bar{B}}$ is the number of $B\bar{B}$ pairs analyzed, and ϵ_{sig} is the reconstruction

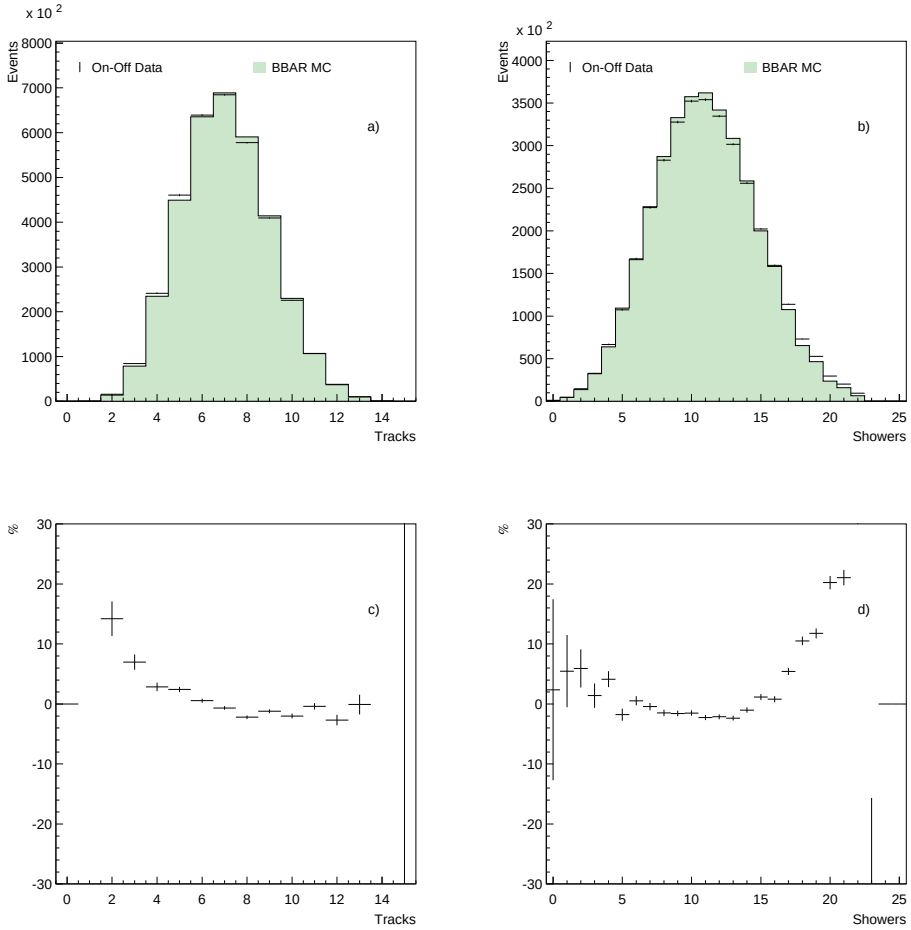

Figure 5.20: Signal Efficiency: Track and Shower Multiplicity.

$B\bar{B}$ Monte Carlo sample compared to On-Off Data. a) Charged Track Multiplicity and c) percent difference. b) Shower Multiplicity and d) percent difference.

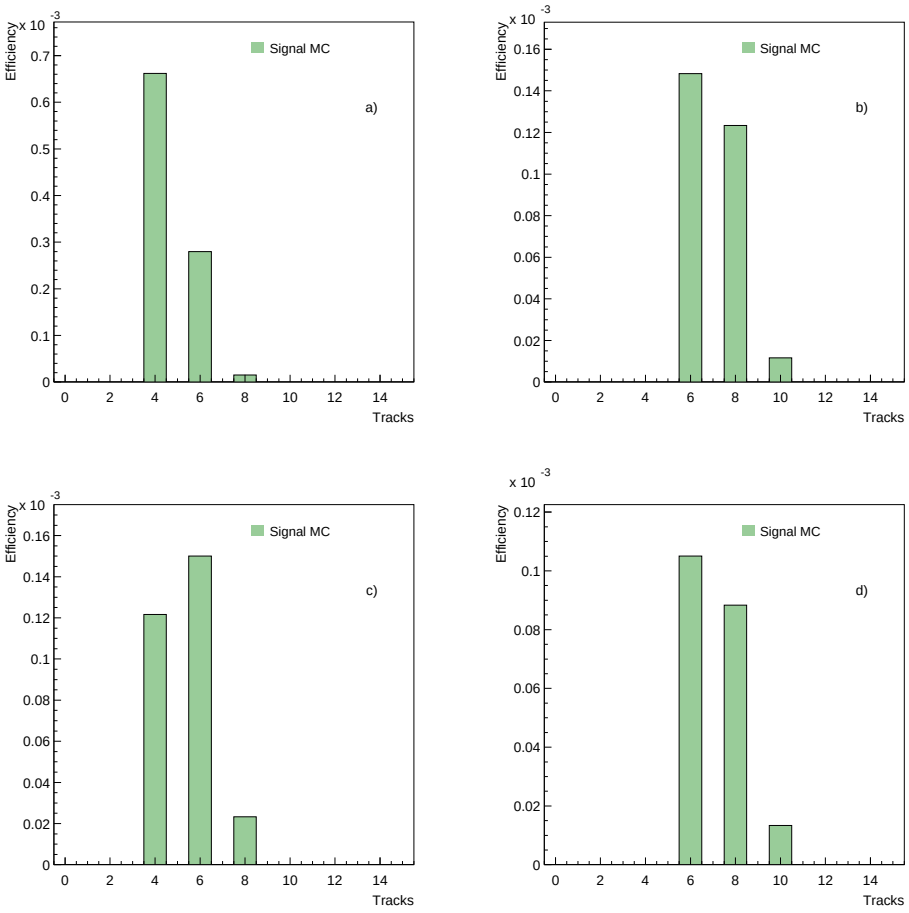

Figure 5.21: Signal Efficiency: ϵ_{sig} vs. Track Multiplicity.

Signal Monte Carlo efficiencies versus event charged track multiplicity for the signal modes K (a), K_S (b), K^* (c), and K^{*0} (d).

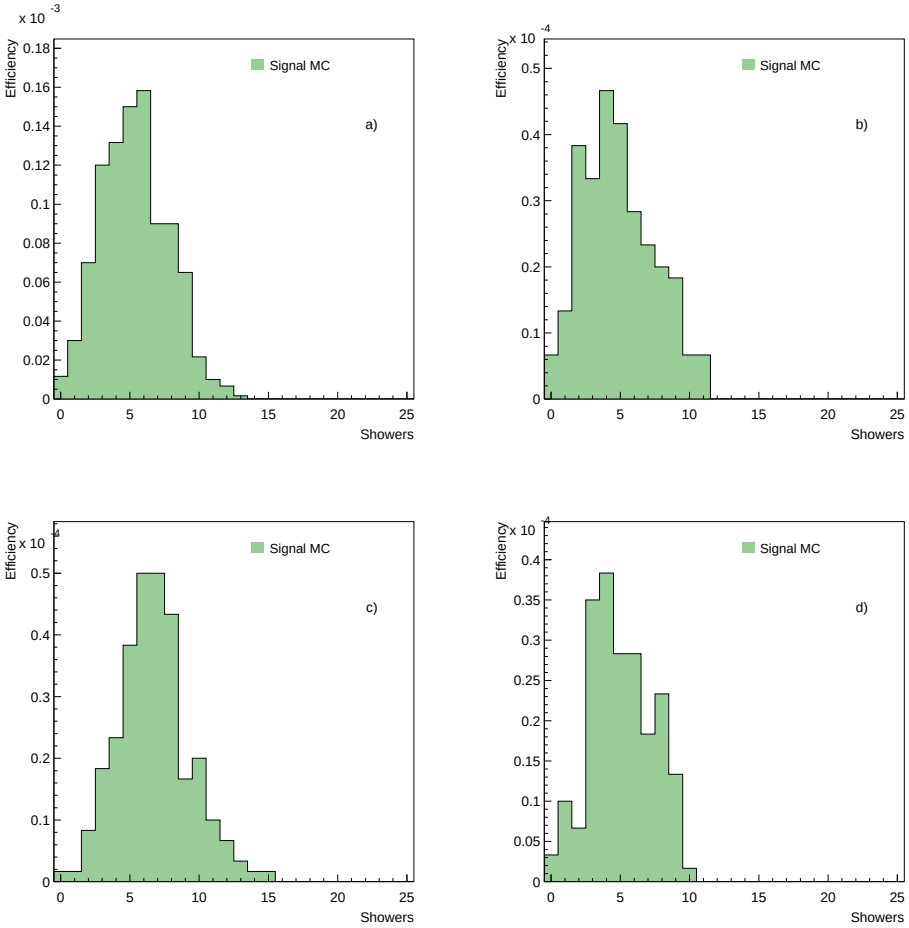

Figure 5.22: Signal Efficiency: ϵ_{sig} vs. Shower Multiplicity.

Signal Monte Carlo efficiencies versus total shower energy for the signal modes K (a), K_S (b), K^* (c), and K^{*0} (d).

Table 5.4: Summary of Signal Efficiency

	Analysis			
	K^+	K_S	K^{*+}	K^{*0}
ϵ_{sig}	9.567×10^{-4}	2.833×10^{-4}	2.950×10^{-4}	2.067×10^{-4}
σ_ϵ $(stat)$	4.2%	7.7%	7.5%	9.0%
σ_ϵ^{track} $(syst)$	3.7%	3.7%	3.3%	3.6%
σ_ϵ^{shower} $(syst)$	2.5%	2.4%	2.7%	2.6%
σ_ϵ $(total)$	6.1%	8.8%	8.6%	10%

efficiency. The denominator is then deflated its error ($\sigma_{fN\epsilon}$). The results are summarized in Table 5.5.

We have searched for the exclusive decays $B \to (K^+, K_S, K^{*+}, K^{*0})\nu\bar{\nu}$ in a sample of 9.7 million charged and neutral B meson decays recorded with the CLEO detector at the $\Upsilon(4S)$resonance. The technique was one of full event reconstruction where after selecting a signal B candidate the remainder of the event was required to be consistent with a hadronic $B \to D^{(*)}(n\pi)$ decay. No signals were observed so the following 90% confidence level upper limits were set: $\mathcal{B}(B^+ \to K^+\nu\bar{\nu}) < 6.1 \times 10^{-4}$, $\mathcal{B}(B^0 \to K_S\nu\bar{\nu}) < 2.3 \times 10^{-3}$, $\mathcal{B}(B^+ \to K^{*+}\nu\bar{\nu}) < 2.0 \times 10^{-3}$, and $\mathcal{B}(B^0 \to K^{*0}\nu\bar{\nu}) < 2.6 \times 10^{-3}$.

Table 5.5: Summary $\mathcal{B}$ Upper Limits

	Analysis			
	K^+	K_S	K^{*+}	K^{*0}
$U_{Y_{sig}}$	5.216	5.525	5.0297	4.329
$f_{+-(00)}$	0.51 ± 0.02	0.49 ± 0.02	0.51 ± 0.02	0.49 ± 0.02
$N_{B\bar{B}}$	$(9.700 \pm 0.19) \times 10^6$			
ϵ_{sig}	9.567×10^{-4}	2.833×10^{-4}	2.950×10^{-4}	2.067×10^{-4}
$\sigma_{\epsilon_{sig}}$	6.1%	8.8%	8.6%	10%
$U_{\mathcal{B}}$	6.1×10^{-4}	2.3×10^{-3}	2.0×10^{-3}	2.6×10^{-3}

APPENDIX A

TRACK SELECTION

This section describes the criteria for selecting the tracks and showers that are used in the reconstruction of the $D^{(*)}$ and $(n\pi)$ from $B \to D^{(*)}(n\pi)$.

A.1 K_S Selection

K_S candidates are selected using the kinematic fitter package `KNVF` [36, 31]. The following quality cuts are applied:

- No Z-escapes or dredge seed tracks are allowed as K_S daughter tracks.
- $|M_{cand} - M_{K_S}| < 0.01$ GeV
- $0 < \chi^2_{fit} < 10.0$
- $\left|\frac{r_{3D}}{\sigma_{r_{3D}}}\right| > 3.0$, where r_{3D} is the signed, 3D, flight distance of the K_S from the beamspot.
- χ^2 of each K_S daughters to point back to the beamspot > 3.0

A.2 π^0 Selection

The following quality cuts were applied to select π^0s:

- $\left|\frac{M_{cand}-M_{\pi^0}}{\sigma_{M_{\pi^0}}}\right| < 3.0$
- $\chi^2_{fit} < 10.0$
- Both π^0 daughter showers must be Splitoff (`SPLTF`) [37] approved.

In addition, for slow π^0s from the decay $B \to D^*\pi^0$ we apply the cut:

- 0.025 GeV $< |\vec{\mathrm{p}}_{\pi^0}| <$ 0.250 GeV

A.3 Isolated Shower (γ) Selection

To select isolated photons we apply the following cuts:

- 0.050 GeV $<$ E$_\gamma <$ 0.350 GeV
- Must not be matched to a track.
- Must not be the daughter of a π^0 as defined in Section A.2 but within 2σ of M_{π^0}.
- Must be in the portion of the calorimeter with polar angle $|\theta_\gamma| < 0.90$.
- For showers $0.80 < |\theta_\gamma| < 0.90$, we require $E_\gamma > 0.10$ GeV

A.4 Charged Track Selection

We apply the following cuts to select charged tracks:

- We require the curvature of the track to be nonzero (`CUCD` $\neq 0$).
- We require the track be Trackman [38] approved (`TNG` ≥ 0).
- We require the track to be classified as `KINCD` $= 0$ or `KINCD` $= -2$ as defined in [39].
- Track may not be used as a daughter of a K_S as defined in Section A.1.
- For hadron candidates, a reduced χ^2, ($\frac{\chi^2}{N_{dof}}$) is calculated combining dE/dx and Time of Flight identification (where available). For $K^{\pm}$ candidates this $\chi^2_{PID_K} < 3.0$, for $\pi^{\pm}$ candidates $\chi^2_{PID_\pi} < 4.0$
- We require that the track not be identified as a lepton (`DPTHMU` < 3.0 or `R2ELEC` < 2.0).

APPENDIX B

SKIMS

The full reconstruction technique is a CPU intensive one, and in order to process the full amount of Generic Monte Carlo and Data samples, we were required to "thin the herd" a little prior to proceeding. This was done by skimming the samples with a stripped down reconstruction described below.

First we found the tracks and vees using the same cuts as the full analysis which were described in Appendix A. Then, we simply summed the number of tracks and showers. We made cuts on these sums as seen in Figures B.1 and B.2. Additionally, we made a diagonal cut on the combination of these variables as seen in Figure B.3.

We then did a simple reconstruction by assuming that all the tracks were pions and all the showers belonged to the companion B. We then removed one track as the signal B and calculated the beam constrained mass and energy difference as we did for the full reconstruction described in Chapter 4. We then made loose cuts on these variables as seen in Figures B.4 and B.5. We also made a cut on the cosine of the missing momentum along the beam axis. This was to removed events whose missing momentum was most likely due to particles lost down the beampipe. For events which pass these cuts, we then require that there be at least one reconstructible D using the same criteria as for the full reconstruction.

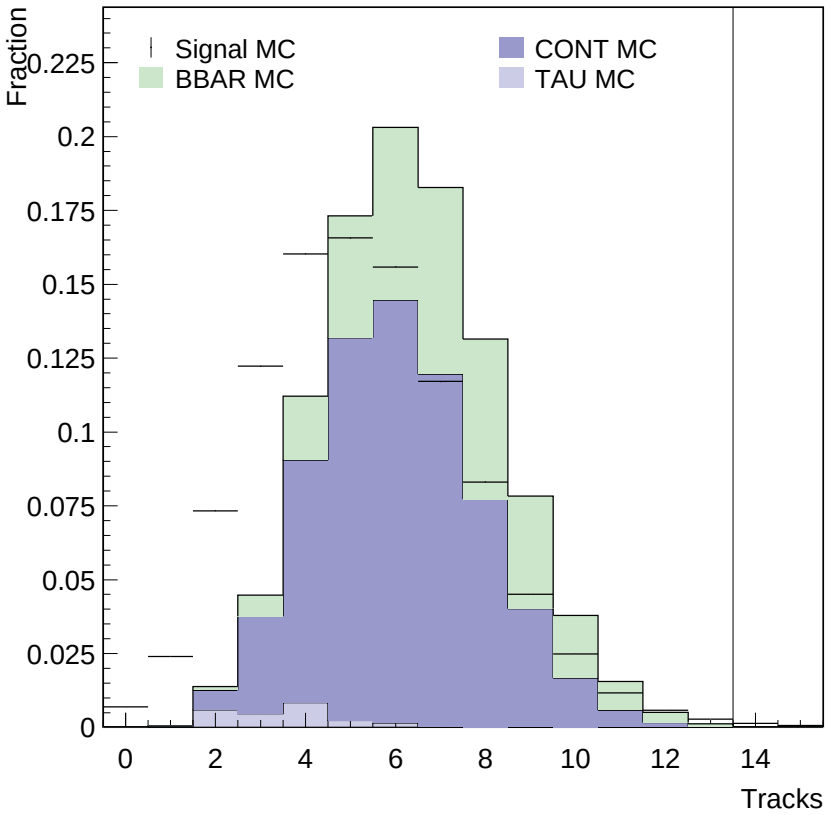

Figure B.1: Number of tracks in the event used for skimming.

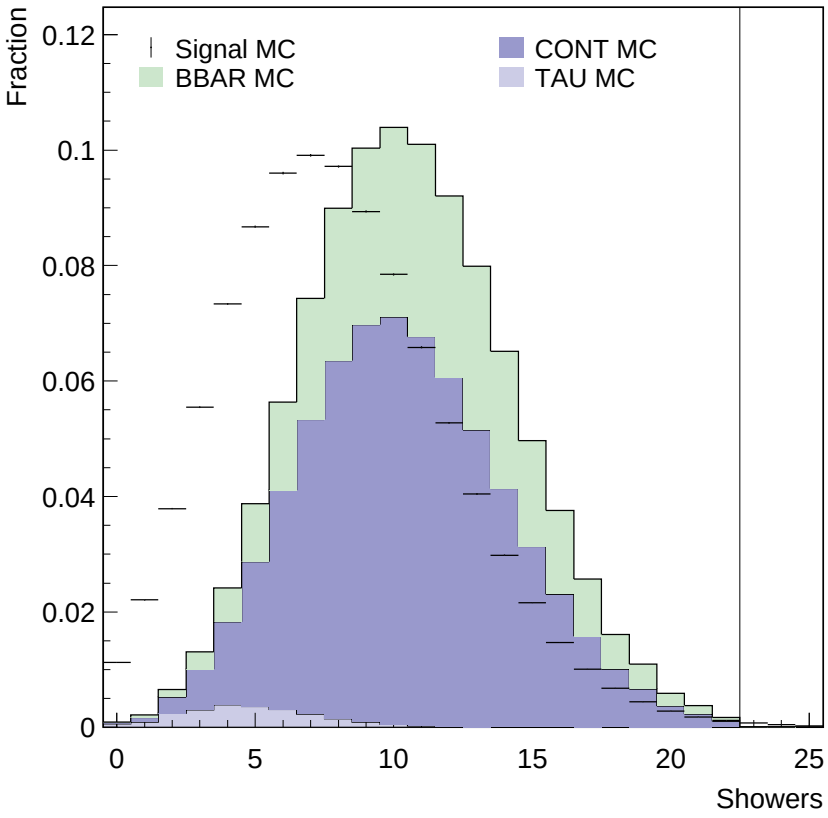

Figure B.2: Number of showers in event used for skimming.

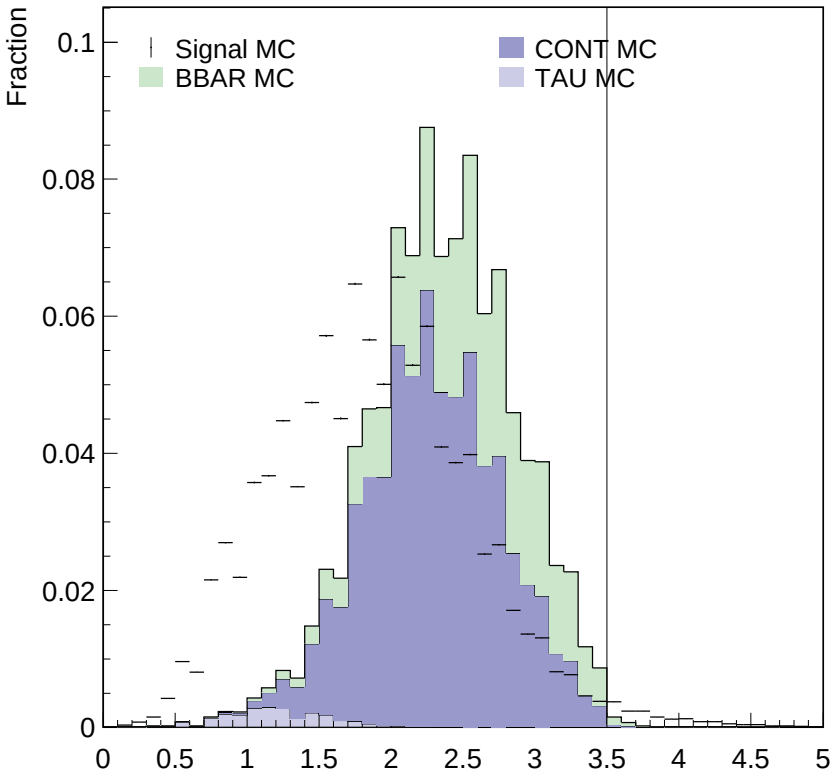

Figure B.3: Linear combination of number of tracks and showers.

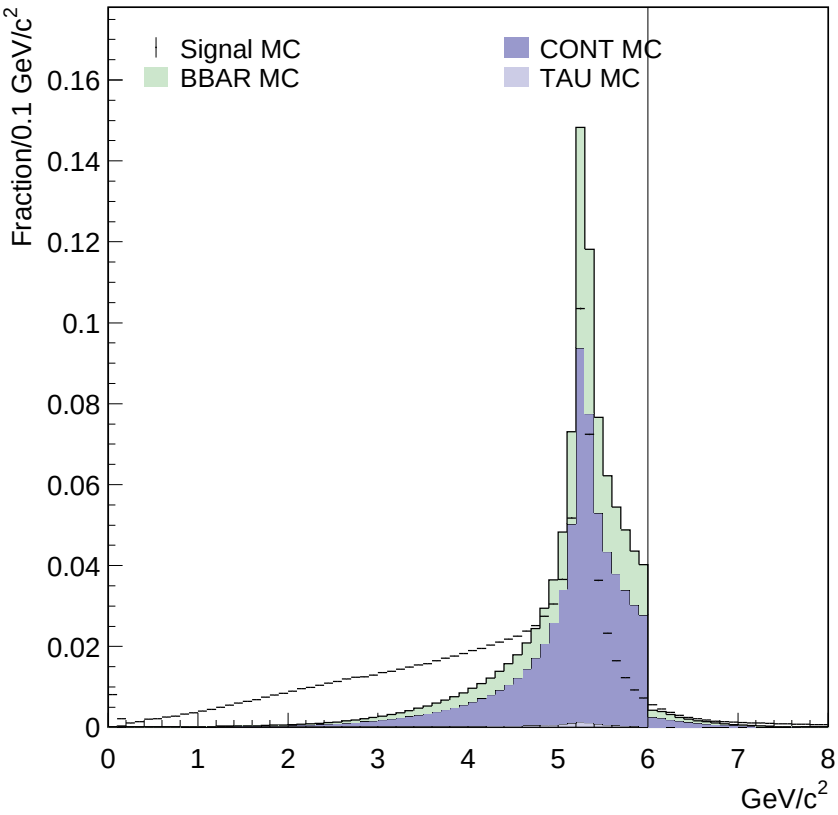

Figure B.4: Skim Beam Constrained Mass.

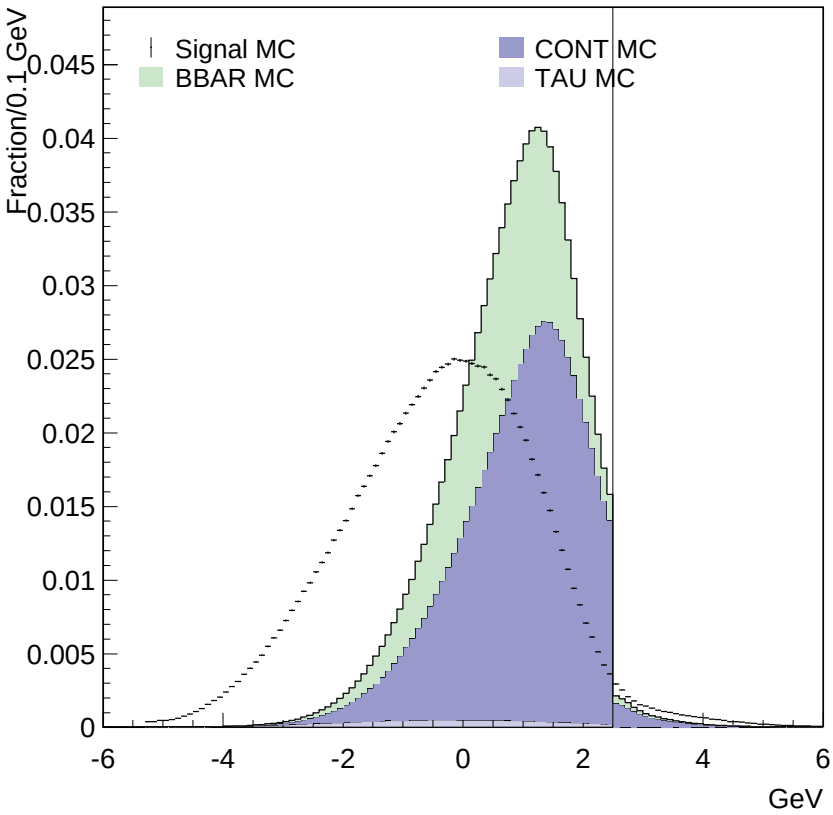

Figure B.5: Skim Beam Energy Difference

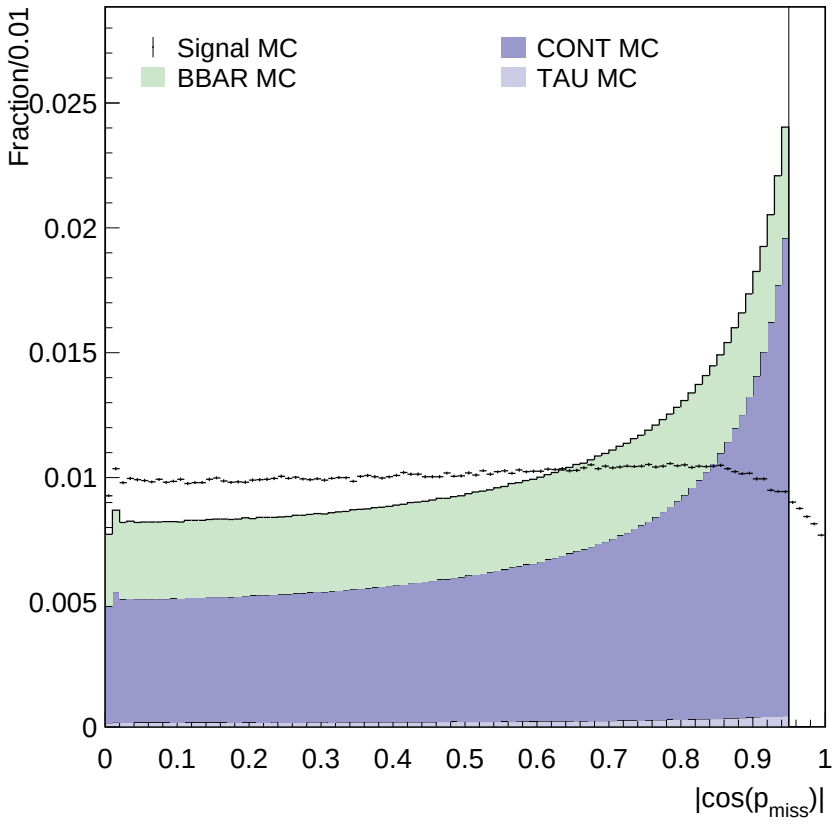

Figure B.6: The cosine of the angle between the missing momentum and the z axis, $|\cos_z(p_{miss})|$

APPENDIX C

DATA SAMPLES

This is a summary of the Data and Monte Carlo samples that were used in this analysis.

Table C.1: Monte Carlo Samples

MC Type	On Resonance Events	Off Resonance Events
K^+ Signal	600,000	
K^{*+} Signal	600,000	
K_S Signal	600,000	
K^{*0} Signal	600,000	
Generic $B\overline{B}$	39,533,543	
Generic Continuum	91,912,406	43,326,699
Generic τ Pair	26,829,840	12,979,644

Table C.2: Data Samples

Data Type	Luminosity (nb^{-1})	$N_{B\overline{B}}$
CLEO II On Resonance	3,136,762.6	3,327,922
CLEO II.V On Resonance	6,028,673.2	6,371,624
Total On Resonance	**9,165,435.8**	9,699,546
CLEO II Off Resonance	1,608,202.5	
CLEO II.V Off Resonance	2,943,593.9	
Total Off Resonance	**4,551,796.4**	

REFERENCES

[1] John C. Taylor. *Hidden Unity in Natural Laws*. Cambridge University Press, 2001.

[2] Klein and Lachièze-Rey. *The Quest for Unity*. Oxford University Press, 1999.

[3] Isaac Asimov. *History of Physics*. Walker and Company, 1966.

[4] David Griffiths. *Introduction to Elementary Particles*. John Wiley and Sons, 1987.

[5] N. Cabibbo. Unitary symmetry and leptonic decays. *Phys. Rev. Lett.*, 10:531–532, 1963.

[6] M. Kobayashi and T. Maskawa. CP violation in the renormalizable theory of weak interaction. *Prog. Theor. Phys.*, 49:652–657, 1973.

[7] S. L. Glashow, J. Iliopoulos, and L. Maiani. Weak interactions with lepton - hadron symmetry. *Phys. Rev.*, D2:1285–1292, 1970.

[8] Andrzej J. Buras. Flavor dynamics: CP violation and rare decays. *hep-ph/0101336*, 2001.

[9] P. Colangelo, F. De Fazio, P. Santorelli, and E. Scrimieri. Rare $B \to K^{(*)}\nu\bar{\nu}$ decays at B factories. *Phys. Lett.*, B395:339–344, 1997.

[10] Ahmed Ali. B decays, flavour mixings and CP violation in the standard model. *hep-ph/9606324*, 1996.

[11] C. S. Kim, Yeong Gyun Kim, and T. Morozumi. New physics effects in $B \to K^{(*)}\nu\bar{\nu}$ decays. *Phys. Rev.*, D60:094007, 1999.

[12] Yuval Grossman, Zoltan Ligeti, and Enrico Nardi. First limit on inclusive $B \to X_s\nu\bar{\nu}$ decay and constraints on new physics. *Nucl. Phys.*, B465:369–398, 1996.

[13] D. Melikhov, N. Nikitin, and S. Simula. Right-handed currents in rare exclusive $B \to (K, K^*)\bar{\nu}$ decays. *Phys. Lett.*, B428:171–178, 1998.

[14] T. M. Aliev and C. S. Kim. Measuring $|V_{td}/V_{ub}|$ through $B \to M\nu\bar{\nu}$ ($M = \pi, K, \rho, K^*$) decays. *Phys. Rev.*, D58:013003, 1998.

[15] T. M. Aliev, A. Ozpineci, and M. Savci. Rare $B \to K^*\nu\bar{\nu}$ decay beyond standard model. *Phys. Lett.*, B506:77–84, 2001.

[16] Z. Ligeti and M. B. Wise. $|V_{ub}|$ from exclusive B and D decays. *Phys. Rev.*, D53:4937, 1996.

[17] M. Wirbel, B. Stech, and Manfred Bauer. Exclusive semileptonic decays of heavy mesons. *Z. Phys.*, C29:637, 1985.

[18] E. Blum et al. Performance of the Cornell High Intensity Linac Injector. CBN 83-8, CESR, 1983.

[19] G. Codner et al. Improvements to the CESR Injector and Injection Process. 2001. Presented at IEEE Particle Accelerator Conference (PAC2001), Chicago, Illinois, 18-22 Jun 2001.

[20] M. Sands. The physics of electron storage rings: An introduction. 1970. SLAC-0121.

[21] Y. Kubota et al. The CLEO-II Detector. *Nucl. Instrum. Meth.*, A320:66, 1992.

[22] T. S. Hill. The CLEO II Silicon Vertex Detector. *Nucl. Instrum. Meth.*, A418:32, 1998.

[23] W. R. Leo. *Techniques for Nuclear and Particle Physics Experiments.* Springer-Verlag, second edition, 1994.

[24] K. Hagiwara et al. Review of particle physics. *Phys. Rev.*, D66:010001, 2002.

[25] F. Sauli. Principles of Operation of Multiwire Proportional and Drift Chambers. Yellow Report 77-09, CERN, 1977.

[26] K. Berkelman. A Personal History of CESR and CLEO. CLNS 02-1784, CLEO, 2002.

[27] K.K. Gan, M. Daubenmier, H. Kagan, and R. Kass. Study of Helium-based Drift Chamber Gases. CBX 95-60, CLEO, 1995.

[28] P. Billor. Track Fitting with Multiple Scattering: A New Method. *Nucl. Instrum. Meth.*, A225:352, 1984.

[29] P. Avery. Applied Fitting Theory V Track Fitting Using the Kalman Filter. CBX 92-39, CLEO, 1992.

[30] P. Avery. Applied Fitting Theory VI Formulas for Kinematic Fitting. CBX 98-37, CLEO, 1998.

[31] C. Prescott. Secondary Vertex Finding Performance and the CLEO II Recompress. CBX 97-69, CLEO, 1997.

[32] Geoffrey C. Fox and Stephen Wolfram. Observables for the analysis of event shapes in e+ e- annihilation and other processes. *Phys. Rev. Lett.*, 41:1581, 1978.

[33] R. Michael Barnett et al. Review of particle physics. *Phys. Rev.*, D54:1–720, 1996.

[34] G. Brandenburg et al. Charged track multiplicity in b meson decay. *Phys. Rev.*, D61:072002, 2000.

[35] J. P. Alexander et al. Measurement of the relative branching fraction of upsilon(4s) to charged and neutral b meson pairs. *Phys. Rev. Lett.*, 86:2737–2741, 2001.

[36] C. Prescott. The KNVF Secondary Vertex Finding Package. CSN 97-353, CLEO, 1997.

[37] L.Gibbons, M.Battle, S.Roberts, E.Thorndike, and K.Bloom. Exclusive $B \to \pi/\rho/\omega\ell\nu$ via Neutrino Reconstruction. CBX 95-6, CLEO, 1995.

[38] S. Roberts, L. Gibbons, and E. Thorndike. Trkman the Next Generation: The quest for track quality. CBX 96-103, CLEO, 1996.

[39] R. Kutschke. Proposal for New Track Bank Conventions. CSN 95-340, CLEO, 1995.